Luckung

NASA Contractor Report 166058

CALCULATION OF POTENTIAL FLOW PAST NON-LIFTING

BODIES AT ANGLE OF ATTACK USING AXIAL AND

SURFACE SINGULARITY METHODS

Jin-Yea Shu and John M. Kuhlman

OLD DOMINION UNIVERSITY
Norfolk, Virginia 23508

NF02241

NASA

National Aeronautics and
Space Administration

Langley Research Center
Hampton, Virginia 23665

CALCULATION OF POTENTIAL FLOW PAST NON-LIFTING

BODIES AT ANGLE OF ATTACK USING AXIAL AND

SURFACE SINGULARITY METHODS

SUMMARY

Two different singularity methods have been utilized to
calculate the potential flow past a three dimensional non-lifting
body. Two separate FORTRAN computer programs have been developed to
implement these theoretical models, which will in the future allow
inclusion of the fuselage effect in a pair of existing subcritical
wing design computer programs.

The first method uses higher order axial singularity
distributions to model axisymmetric bodies of revolution in an
either axial or inclined uniform potential flow. Use of inset of
the singularity line away from the body for blunt noses, and cosine-
type element distributions have been applied to obtain the optimal
results. Excellent agreement, to five significant figures, with the
exact solution pressure coefficient value has been found for a
series of ellipsoids at different angles of attack. Solutions
obtained for other axisymmetric bodies compare well with available
experimental data.

The second method utilizes distributions of singularities on
the body surface, in the form of a discrete vortex lattice. This
program is capable of modeling arbitrary three dimensional non-
lifting bodies. Much effort has been devoted to finding the optimal
method of calculating the tangential velocity on the body surface,
extending techniques previously developed by other workers. Again,

the best solution for ellipsoids at angles of attack ranging between 0-30°, has been obtained using cosine spacing of the elements axially.

For a simple axisymmetric body of revolution without any slope discontinuity on the body surface, the first method offers a more accurate solution for less computational cost than the second method.· Therefore, while the surface singularity method has the advantage of greater geometry generality, the axial singularity method is judged more suitable for modeling of fuselage effects in a preliminary aerodynamic design computer program.

CHAPTER 1

INTRODUCTION

Use of computers in aerodynamic theory has seen a trend in recent years toward the flow field analysis of complete aircraft configurations by a single program using a combination of boundary layer analysis and the full potential equation. Programs designed for this purpose do in fact exist, (refer here to references by Streett (1981) or by Mason (1977)), but most of them are extremely large and abound with subtleties often not evident to the user. In an ongoing research effort to include the body effect in a pair of existing wing design computer programs (Kuhlman and Shu, 1981; Kuhlman, 1983), it was decided to first develop separate fuselage programs as a preliminary step. Based on this spirit, the present work investigates the flow field around certain fuselage-shaped bodies using two theoretical formulations and their resulting computer programs. Either of these codes might possibly then be used in the above mentioned subcritical wing design programs to include the effects of a fuselage on the design.

The problem under consideration in this study is that of the uniform, incompressible, inviscid, potential flow past a non-lifting body. Bodies of interest may be either axisymmetric or arbitrary, although results to be presented herein have been limited to axisymmetric bodies. The governing differential equation in terms of the velocity potential ϕ is the well known Laplace's equation.

The surface of the body can, in general, be described by a function $F(x_1, x_2, x_3) = 0$. The variables x_1, x_2, and x_3 are determined by the coordinate system used in the calculation. The mathematical statement of this problem is to find a solution to:

$$\nabla^2 \Phi = 0 \tag{1.1}$$

subject to the boundary conditions

$$\text{grad } \Phi \cdot \text{grad } F = \vec{V} \cdot \text{grad } F = 0 \tag{1.2}$$

on the body, $F(x_1, x_2, x_3) = 0$

and

$$\text{grad } \Phi = U_\infty \vec{i} \quad \text{at infinity} \tag{1.3}$$

If the problem is rewritten in terms of the perturbation field ϕ, due to the body, equations (1.1 to 1.3) become:

$$\nabla^2 \phi = 0 \tag{1.4}$$

$$(\text{grad } \phi + U_\infty \vec{i}) \cdot \text{grad } F = 0$$
$$\text{on } F(x_1, x_2, x_3) = 0 \tag{1.5}$$

$$\text{grad } \phi \rightarrow 0 \quad \text{at infinity} \tag{1.6}$$

Despite the fact that Laplace's equation is one of the simplest

4

and best known of all partial differential equations, the number of known useful exact solutions is quite small. The only exact solution of the uniform potential flow about a closed three-dimensional body is that for the general ellipsoid and its specializations. This is due to the difficulty in satisfying the nonhomogeneous boundary conditions and the requirement for the body surface to be a coordinate surface of one of the special orthogonal coordinate systems for which Laplace's equation can be separated into ordinary differential equations. As a result, use of numerical approximate solutions is usually considered in practical applications. Many different numerical schemes have been formulated. Some are exact in problem formulation and numerical methods then are used to obtain the approximate solution. Under such schemes, errors in the calculated solution can in principle be made as small as desired, by sufficiently refining the numerical calculations. In contrast, some schemes introduce analytical approximations into the problem formulation itself, and thus place limits on the accuracy that can be obtained regardless of the numerical procedures used. One typical example is the so called slender body theory where the body boundary condition is greatly simplified for high fineness ratio bodies.

The present study is based on the first classification which is exact in formulation and numerical in solution. There are two main classes of numerical approaches; axial and surface singularity methods, which may be used in solving the potential flow past non-lifting bodies. From a practical point of view, these two methods each have their own characteristic properties and advantages.

Choice of method for a particular application is largely dependent upon the configuration of interest and how accurate the solution must be. In general, the axial singularity method has less flexibility than the surface singularity method, in that it can not handle certain axisymmetric bodies with discontinuous slopes, nor can it handle the entire class of non-axisymmetric bodies. However, for simple and axisymmetric body shapes, the axial singularity method is easier and more economical to use than the surface singularity method. In contrast, the surface singularity method is in principle more accurate and has fewer geometrical restrictions when compared to the axial singularity method. It is, then, much more sophisticated and powerful, but requires a substantially greater number of numerical calculations and more computer storage. Other solution methods applicable to solving Laplace's equation include finite difference methods (David and Geppson, 1973), but these methods have not been utilized in the present study. This is because the singularity methods based upon Green's theorem significantly reduce the cost of obtaining a numerical solution for ϕ to a certain accuracy, largely as a result of reduction of the problem to finding a suitable singularity distribution on the body surface, rather than requiring that a solution for ϕ be determined in the entire region exterior to the body. The development of the present singularity methods have been summarized in Chapters 2 and 3 of this thesis, for the axial and surface singularity methods; respectively. Also given in these chapters are brief literature surveys.

In light of these considerations, a FORTRAN computer program

6

based on the axial singularity method has been implemented in the present work for the simple, axisymmetric fuselage. Much effort has been devoted to obtain the most accurate numerical solution for both axisymmetric flow and inclined flow. Higher order axial singularity distributions have been formulated for both axial flow and cross flow. Pressure distribution results for ellipsoidal bodies as presented in Chapter 2, show excellent agreement with the exact solution everywhere on the body at arbitrary angle of attack providing that separation does not exist on the body. In Chapter 4, additional results from the axial singularity method, for more complicated geometries, have been compared with results from a surface singularity program described in Chapter 3 and with experimental data.

Although the surface panel method is not considered an efficient model to evaluate fuselage effects in the preliminary wing design program, because large computer memory and long computational time are needed to perform the calculation, it does offer a reliable solution which can serve as a bench mark for those solutions obtained from the axial singularity method. Chapter 3 gives a detailed outline of the formulation and accuracy of the surface panel technique utilized in the present study. A second FORTRAN computer program has been implemented as part of the present work to perform numerical calculations, for ellipsoidal bodies in axisymmetric flow or at angle of attack. These results have been presented in Chapter 3, while results for more complex geometries have been presented in Chapter 4.

LIST OF SYMBOLS

a	inset distance or semi-major axis of ellipsoid
A	area of vortex lattice panel
b	semi-minor axis of ellipsoid
C_p	pressure coefficient
d	distance from control point to vortex filament
e	eccentricity of ellipsoid
ℓ	body length or vortex filament length or panel chord length
L	total body length
K_a	axial coefficient of virtual mass in equn. (2.66)
K_c	cross coefficient of virtual mass in equn. (2.66)
M	order of singularity strength polynomial function or Mach number.
$\vec{n}$	unit normal vector
N	total number of axial singularity panels or total number of vortex lattice panels
P_{ij}, q_{ij}, r_{ij}	vortex lattice influence coefficients, see equn. (3.3)
q	source strength
r	radial coordinate or magnitude of position vector
R	nose radius of curvature or shoulder radius of body
s	bounding surface of a region
u	axial velocity component
u_x, u_r, u_θ	axial, radial and circumferential velocity components
U_∞	free-stream velocity

8

V	total tangential velocity or induced velocity due to a vortex filament
V_t	total tangential velocity
w	radial velocity component
W	self-induced velocity due to a closed loop with unit strength of circulation
x,y,z	cartesian coordinates of points
x,r,θ	cylindrical coordinates of points
α	angle of attack
β	inclination angle of control point with x-axis
Γ	strength of circulation
Θ	circumferential velocity component
θ	circumferential coordinate or meridian angle or inclination angle of panel with x-axis
μ	doublet strength or curvelinear coordinate variable
ξ	axial integration variable
π	ratio of circumference to diameter of circle
ρ	radial distance of control point to body axis
τ_v	tangential velocity due to local vortex lattice panel
Φ	velocity potenial
φ	disturbance velocity potential

SUBSCRIPTS

c	index of panel control point or centroid of area
i	index of control point for axial singularity method
j	index of influencing panel
k	summation index

m	index of minimum induced velocity point
x1, r1	index of axial and radial components for axial flow
x2,r2,θ	index of axial, radial and circumferential components for crossflow

ABBREVIATIONS

CS	constant source
CD	constant doublet
LVS	linearly varying source
LVD	linearly varying doublet
CPE	exact value of pressure coefficient
CPN	numerical value of pressure coefficient
SR	slenderness ratio

CHAPTER 2

AXIALLY DISTRIBUTED SINGULARITY METHOD FOR

AXISYMMETRIC BODY OF REVOLUTION

2.1 Literature Survey

The idea of utilizing a distribution of singularities interior to the body surface to represent the potential flow past a body of revolution was first introduced by Von Karman (1930), who considered axisymmetric shapes in axisymmetric flow and represented them by a piecewise constant source distribution along the axis of symmetry. Since the original work of Von Karman, very little information on this method has been generated, until recently when Oberkampf and Watson (1974) discovered that this method produces a system of linear equations which is in general ill-conditioned, and requires very high computational accuracy (25 significant figures) in the construction of the influence coefficient matrix. They concluded that the method does not always produce reliable solutions for the flow around a specified body and is very sensitive not only to the shape of the contour but also to the number of elements used to generate the body. Karamcheti (1966) states that the body should be slender and should not have any discontinuities in the slope of the meridian line. Zedan and Dalton (1978) extended the method by employing piecewise linearly varying source distributions to improve the computational accuracy. The solutions obtained therein are more accurate as compared to the constant strength element methods. One

11

of the most important features of the linearly varying source method is its ability to deal with bodies having an inflection point in the meridian contour. They again concluded that their new method cannot handle body shapes with sudden changes in the slope of the meridian line. More recently, Zedan and Dalton (1980) have used a polynomial function of arbitrary degree to represent the variation of the intensity of the source distribution over each element. The effects of the order of the distribution, the number of elements, the normalization of the body coordinates, the fineness ratio and the geometry of the profile on the performance of the method have been studied in detail. They concluded that with appropriate choice of these parameters, this approach can be as accurate as the surface singularity approach even for simple axisymmetric bodies with inflection points.

In view of the simplicity of the axial source distribution methods as compared to the surface singularity distribution methods, and the tremendous saving in computer memory storage and the amount of numerical calculation necessary, it was considered justifiable to apply this method as an initial step in considering the effect of an axisymmetric fuselage upon the optimal camber surface obtained from an existing aerodynamic wing-design computer program, provided the accuracy can be improved and the limitations can be reduced for the former class of methods.

The present study is an extension of Zedan and Dalton's work. An axial singularity distribution is placed along the centerline of the body of revolution, where this singularity distribution is assumed to have either a piecewise constant or a piecewise linearly

12

varying strength over a series of discrete segments. Expressions for velocity potential and induced velocities have been developed for source (identical to those of Zedan and Dalton, 1980) and doublet (as suggested in Karamcheti, 1966) singularity distributions. In addition to this, the expressions have been extended for piecewise constant, or linearly varying crossflow doublet singularities, which allows simulation of an axisymmetric fuselage at angle of attack.

A FORTRAN computer program has been developed to implement this theoretical model. This program is currently available for use in the optimal wing-design computer programs (Kuhlman and Shu, 1981; Kuhlman, 1983). Future plans are to add the current axisymmetric body model in the wing-design code. In this chapter the development of the theoretical model will be summarized, and the effects of the type of singularity, the order of the distribution, the number of elements, the geometry of the profile, as well as some paneling techniques, on the performance of the method will be shown by using a simple ellipsoidal test case. Results have been obtained for a series of ellipsoidal bodies of revolution of varying slenderness ratio and angle of attack, and these results have been compared with an exact solution summarized in Wang (1970). Results for more complicated axisymmetric bodies will be presented in Chapter 4.

2.2 Formulation and Equations of the Problem

2.2.1 Formulation of the Problem

Consider the steady, acyclic, potential flow past an axisymmetric body of revolution that is at an angle of attack to the direction of the undisturbed stream (see Sketch 2.1).

13
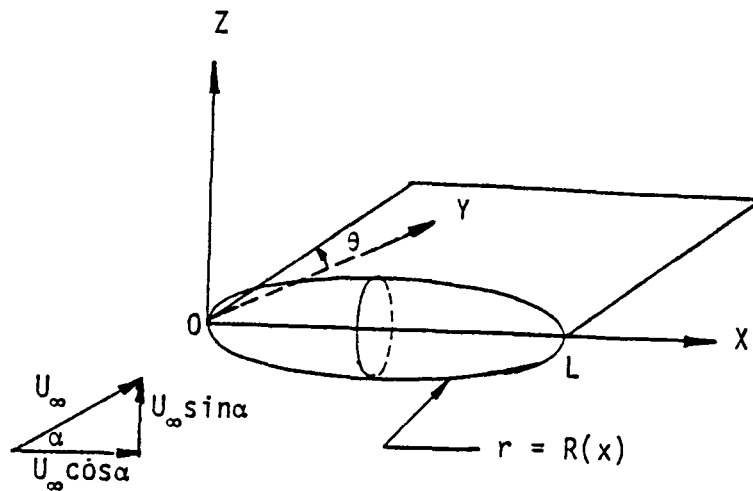
Sketch 2.1   Illustrating flow with angle of
            attack past the body of revolution.

In analyzing the flow past a body of revolution, it is
convenient to use cylindrical coordinates (r,θ,x) as shown in Sketch
2.1. The surface of the body is described by an equation of the
form $r = R(x)$. This may also be expressed as $F(r,x) = r - R(x) = 0$.
Equations (1.4 to 1.6) then take the following form:

$$\frac{\partial^2 \phi}{\partial r^2} + \frac{1}{r} \frac{\partial \phi}{\partial r} + \frac{1}{r^2} \frac{\partial^2 \phi}{\partial \theta^2} + \frac{\partial^2 \phi}{\partial x^2} = 0$$

(2.1)

$$\left(U_\infty \sin\alpha \sin\theta + U_r\right) \frac{\partial F}{\partial r} + \left(U_\infty \cos\alpha + U_x\right) \frac{\partial F}{\partial x} = 0$$

$$\text{on } F(r,x) = 0$$

(2.2)

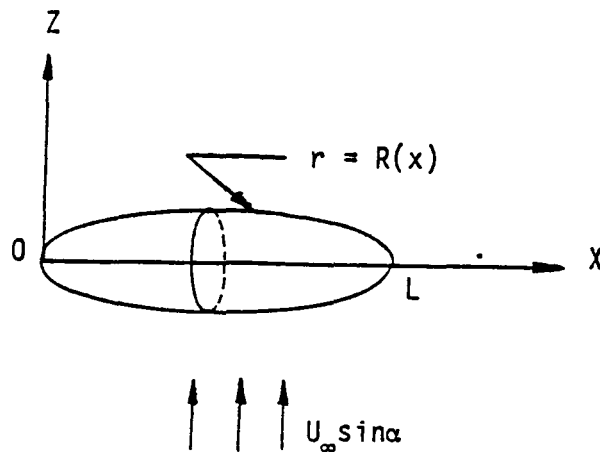$$\nabla\phi \rightarrow 0 \quad \text{at infinity}$$

(2.3)

where $U_r = \frac{\partial \phi}{\partial r}$, $U_\theta = \frac{1}{r} \frac{\partial \phi}{\partial \theta}$, $U_x = \frac{\partial \phi}{\partial x}$

Due to the linearity of the problem (governing equation and boundary

14

conditions), the solution of Equations (2.1 to 2.3) may be expressed as the superposition of the solutions of two separate problems: (1) the problem representing the axial flow at speed $U_\infty \cos\alpha$ past the body of revolution, and (2) the problem representing the cross flow at speed $U_\infty \sin\alpha$ past the same body of revolution (See Sketches 2.2 and 2.3).
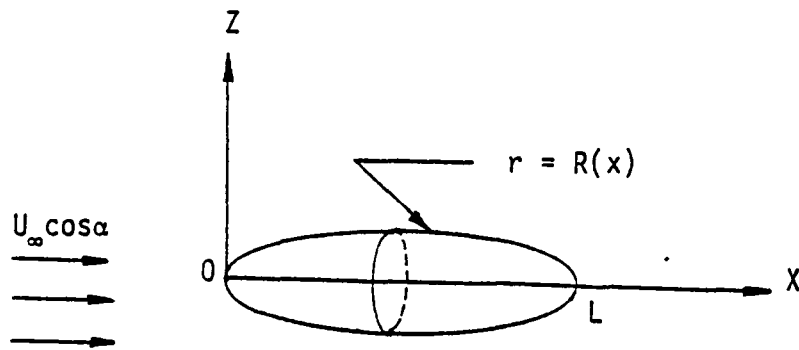
Sketch 2.2   Illustrating axial flow past the body of revolution

Sketch 2.3   Illustrating cross flow past the body of revolution

These two mathematical problems may be stated in the form of:

Axisymmetric Flow Past a Body of Revolution: $\phi_1 = \phi_1(r,x)$

$$\nabla^2 \phi_1 = 0 \qquad\qquad (2.4)$$

$$U_{r1}(R,x) - U_{x1}(R,x) \frac{dR}{dx} = U_\infty \cos\alpha \frac{dR}{dx} \qquad (2.5)$$

$$\nabla\phi_1 \rightarrow 0 \qquad \text{at infinity} \qquad (2.6)$$

Cross Flow Past a Body of Revolution: $\phi_2 = \phi_2(r,\theta,x)$

$$\nabla^2 \phi_2 = 0 \qquad\qquad (2.7)$$

$$U_{r2}(R,x) - U_{x2}(R,x) \frac{dR}{dx} = -U_\infty \sin\alpha \sin\theta \qquad (2.8)$$

$$\nabla\phi_2 \rightarrow 0 \qquad \text{at infinity} \qquad (2.9)$$

Then one is able to use line singularity distribution techniques to solve these two problems and obtain the total solution by superposition of ϕ_1 and ϕ_2. For the axisymmetric flow part, one might use sources or doublets along the body axis. The singularity distribution is divided into finite elements. The strength variation over each element can be described by a polynomial function of arbitrary degree. In this study, we consider four types of representations, which are: constant source, linearly varying source, constant doublet, and linearly varying doublet. For

16

convenience to extend the method to higher order singularity
expressions, the general formulas have been listed for reference.
The cross flow part, as suggested by Karamcheti (1966), has been
represented by a piecewise constant doublet or linearly varying
doublet distribution along the axis of the body, with the axes of
the doublets being normal to the body axis; the doublet axes oppose
the direction of the undisturbed crossflow stream at infinity (see
Sketch 2.4). After solving these two mathematical problems, one can
obtain the pressure coefficient by using Bernoulli's equation

$$C_p = 1 - \frac{V^2}{U_\infty^2} \qquad (2.10)$$
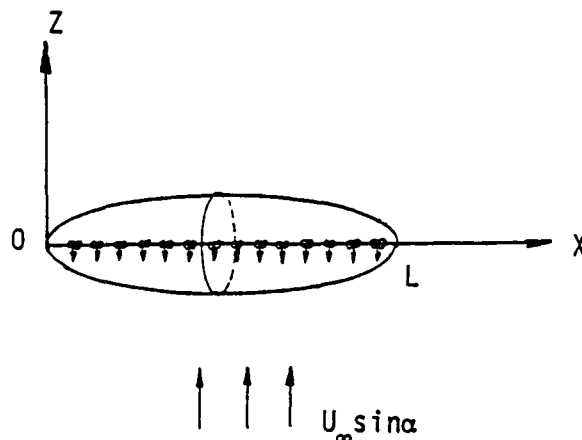
Sketch 2.4 Cross flow past a body of revolution
by combination of a doublet distribution
and a uniform stream

Although one can superpose the ϕ and $\vec{V}$, one cannot do the same for
the pressure coefficient since it is a nonlinear function of $\vec{V}$.
Here V is local total velocity, in the following form:

$$V^2 = (U_\infty \cos\alpha + U_{x1} + U_{x2})^2 + (U_\infty \sin\alpha\sin\theta + U_{r1} + U_{r2})^2$$

$$+ (U_\infty \sin\alpha\cos\theta + U_\theta)^2 \qquad (2.11)$$

and $\quad U_{x1} = \dfrac{\partial\phi_1}{\partial x}$, $\quad U_{x2} = \dfrac{\partial\phi_2}{\partial x}$, $\quad U_{r1} = \dfrac{\partial\phi_1}{\partial r}$

$$U_{r2} = \frac{\partial\phi_2}{\partial r}, \quad U_\theta = \frac{1}{r}\frac{\partial\phi_2}{\partial\theta} \qquad (2.12)$$

2.2.2 Equations for an Element

The following three techniques have been used to evaluate the integrals which will appear in the induced velocity expressions: (1) integration by analytic geometry relationships, (2) integral tables, and (3) the MACSYMA symbolic manipulation language (Bogen et al., 1975). All three methods have been utilized in the present work, with the majority of the integrations having been performed by MACSYMA.

In the following six different element equations, we define the symbolic expressions:

$$H_k = \int_{\ell_1}^{\ell_2} \frac{\xi^{K-1}}{[(x_i-\xi)^2 + r_i^2]^{3/2}} \, d\xi \qquad (2.13)$$

$$P_K = \int_{\ell_1}^{\ell_2} \frac{\xi^{K-1}}{[(x_i-\xi)^2 + r_i^2]^{5/2}} \, d\xi \qquad (2.14)$$

where (ℓ_1, ℓ_2) are the X coordinates of the endpoints of the element. Then the MACSYMA symbolic manipulation language has been utilized to obtain the integral expressions as listed in Appendix A.

18

2.2.2.1 Constant source distribution. Consider first the jth element of an axial singularity distribution having a constant intensity q_j as shown in Sketch 2.5. The velocity potential function and the velocity components at the ith point (x_i, r_i) are given by

$$\phi(x_i, r_i) = -\frac{1}{4\pi} \int_{\ell_1}^{\ell_2} \frac{q_j}{[(x_i-\xi)^2 + r_i^2)^{1/2}} \, d\xi \qquad (2.15)$$

$$u(x_i, r_i) = \frac{1}{4\pi} \int_{\ell_1}^{\ell_2} \frac{q_j(x_i-\xi)}{[(x_i-\xi)^2 + r_i^2]^{3/2}} \, d\xi \qquad (2.16)$$

$$w(x_i, r_i) = \frac{1}{4\pi} \int_{\ell_1}^{\ell_2} \frac{q_j r_i}{[(x_i-\xi)^2 + r_i^2]^{3/2}} \, d\xi \qquad (2.17)$$

Here q_j is constant on element j.

Using tables of integrals (Gradshteyn and Ryzhik, 1980), u and w are evaluated in closed form as

$$u(x_i, r_i) = \frac{q_j}{4\pi} \left[\frac{x_i}{r_i^2} \left(\frac{\ell_2 - x_i}{\sqrt{\ell_2^2 - 2x_i\ell_2 + x_i^2 + r_i^2}} - \frac{\ell_1 - x_i}{\sqrt{\ell_1^2 - 2x_i\ell_1 + x_i^2 + r_i^2}} \right) \right.$$

$$\left. - \frac{1}{r_i^2} \left(\frac{x_i\ell_2 - x_i^2 - r_i^2}{\sqrt{\ell_2^2 - 2x_i\ell_2 + x_i^2 + r_i^2}} - \frac{x_i\ell_1 - x_i^2 - r_i^2}{\sqrt{\ell_1^2 - 2x_i\ell_1 + x_i^2 + r_i^2}} \right) \right]$$

$$(2.18)$$

$$w(x_i, r_i) = \frac{q_j}{4\pi} \frac{1}{r_i} \left(\frac{\ell_2 - x_i}{\sqrt{\ell_2{}^2 - 2x_i\ell_2 + x_i{}^2 + r_i{}^2}} - \frac{\ell_1 - x_i}{\sqrt{\ell_1{}^2 - 2x_i\ell_1 + x_i{}^2 + r_i{}^2}} \right)$$

$$(2.19)$$

In MACSYMA language expressions (Appendix A), the constant source velocity may be expressed as

$$u(x_i, r_i) = \frac{q_j}{4\pi} (x_i H_1 - H_2) \qquad\qquad (2.20)$$

$$w(x_i, r_i) = \frac{q_j}{4\pi} r_i H_1 \qquad\qquad (2.21)$$

2.2.2.2 Linearly varying source distribution. If the jth element (see Sketch 2.5) is assumed to have a linearly varying source distribution, $q_j = a_{j1} + a_{j2}\xi$, the velocity potential function and the velocity components at the ith point (x_i, r_i) are given by
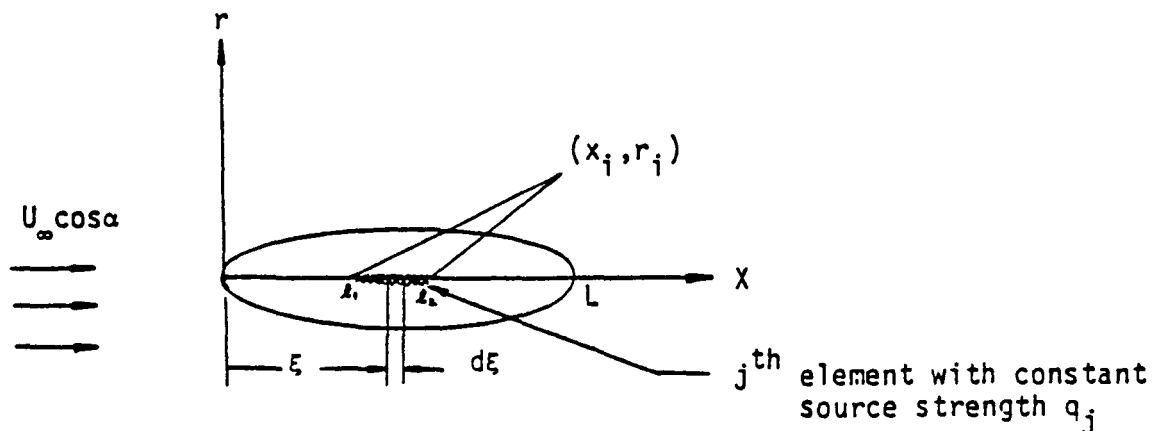
Sketch 2.5   Illustrating axial singularity panelling scheme

20

$$\phi(x_i, r_i) = -\frac{1}{4\pi} \int_{\ell_1}^{\ell_2} \frac{a_{j1} + a_{j2}\,\xi}{\sqrt{(x_i-\xi)^2 + r_i^2}}\, d\xi \qquad (2.22)$$

$$u(x_i, r_i) = \frac{1}{4\pi} \int_{\ell_1}^{\ell_2} \frac{(a_{j1}+a_{j2}\,\xi)(x_i-\xi)}{[(x_i-\xi)^2 + r_i^2]^{3/2}}\, d\xi \qquad (2.23)$$

$$w(x_i, r_i) = \frac{r_i}{4\pi} \int_{\ell_1}^{\ell_2} \frac{a_{j1} + a_{j2}\,\xi}{[(x_i-\xi)^2 + r_i^2]^{3/2}}\, d\xi \qquad (2.24)$$

Equations (2.23 and 2.24) can be rewritten as:

$$u(x_i, r_i) = \frac{1}{4\pi}\left[a_{j1}(x_i H_1 - H_2) + a_{j2}(x_i H_2 - H_3)\right] \qquad (2.25)$$

$$w(x_i, r_i) = \frac{r_i}{4\pi}\left[a_{j1}H_1 + a_{j2}H_2\right] \qquad (2.26)$$

At this point, to extend the scheme to an arbitrary M^{th} order polynomial function, simply let $q_j = \sum_{K=1}^{M+1} a_{jK}\xi^{K-1}$, substitute back into equations (2.16 and 2.17) and evaluate the integrals to obtain the following general expressions:

$$u(x_i, r_i) = \frac{1}{4\pi} \sum_{K=1}^{M+1} a_{jK}(x_i H_K - H_{K+1}) \qquad (2.27)$$

$$w(x_i, r_i) = \frac{r_i}{4\pi} \sum_{K=1}^{M+1} a_{jK}H_K \qquad (2.28)$$

where a_{jK} are constants.

21

2.2.2.3 Constant doublet distribution. Next, the source singularity is replaced by a doublet singularity with axes directed into the undisturbed stream (see Sketch 2.6). That is, the doublet strength is written as $\vec{\mu}_j = -\mu_j \vec{i}$. The velocity potential function and the velocity components at the ith point (x_i, r_i) due to the jth element are given by:

$$\phi(x_i, r_i) = \frac{1}{4\pi} \int_{\ell_1}^{\ell_2} \frac{\mu_j(x_i - \xi)}{[(x_i - \xi)^2 + r_i^2]^{3/2}} \, d\xi \qquad (2.29)$$
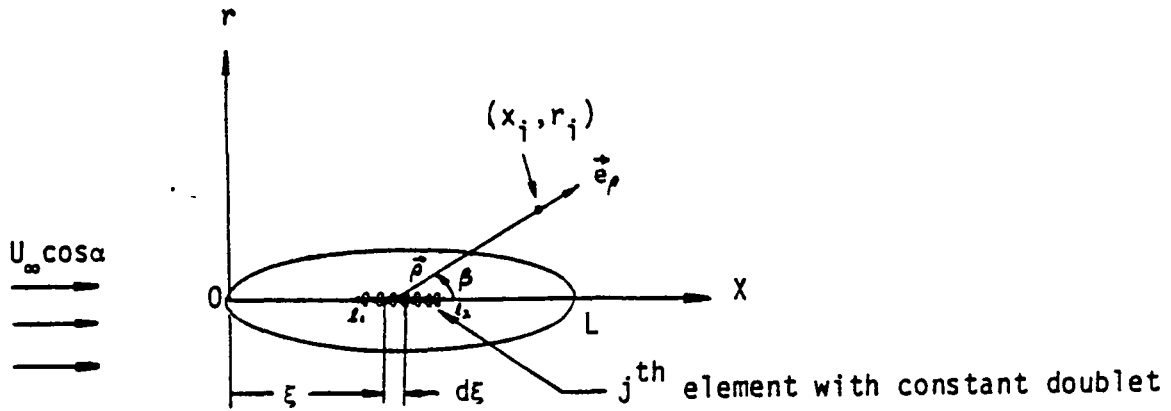
$$u(x_i, r_i) = \frac{1}{4\pi} \int_{\ell_1}^{\ell_2} \frac{\mu_j}{[(x_i - \xi)^2 + r_i^2]^{3/2}} \, d\xi - \frac{3}{4\pi} \int_{\ell_1}^{\ell_2} \frac{\mu_j(x_i - \xi)^2}{[(x_i - \xi)^2 + r_i^2]^{5/2}} \, d\xi$$

$$(2.30)$$

$$w(x_i, r_i) = -\frac{3r_i}{4\pi} \int_{\ell_1}^{\ell_2} \frac{\mu_j(x_i - \xi)}{[(x_i - \xi)^2 + r_i^2]^{5/2}} \, d\xi \qquad (2.31)$$

Equations (2.30 and 2.31) may be evaluated for a piecewise constant doublet distribution in the following forms:

$$u(x_i, r_i) = \frac{\mu_j}{4\pi} H_1 - \frac{3\mu_j}{4\pi} (x_i^2 P_1 - 2x_i P_2 + P_3) \qquad (2.32)$$

$$w(x_i, r_i) = \frac{3r_i \mu_j}{4\pi} (x_i P_1 - P_2) \qquad (2.33)$$

Sketch 2.6   Illustrating axial doublet singularity
panelling scheme

2.2.2.4 Linearly varying doublet distribution.

If the doublet strength is linearly varying over the jth element, $-\mu_j \vec{i} = -(a_{j1} + a_{j2}\xi)\vec{i}$, the velocity potential function and the velocity components at the ith point (x_i, r_i) due to this panel are given by:

$$\phi(x_i, r_i) = \frac{1}{4\pi} \int_{\ell_1}^{\ell_2} \frac{(a_{j1}+a_{j2}\xi)(x_i-\xi)}{[(x_i-\xi)^2 + r_i^2]^{3/2}} \, d\xi \qquad (2.34)$$

$$u(x_i, r_i) = \frac{1}{4\pi} \int_{\ell_1}^{\ell_2} \frac{a_{j1} + a_{j2}\xi}{[(x_i-\xi)^2 + r_i^2]^{3/2}} \, d\xi - \frac{3}{4\pi} \int_{\ell_1}^{\ell_2} \frac{(a_{j1}+a_{j2}\xi)(x_i-\xi)^2}{[(x_i-\xi)^2 + r_i^2]^{5/2}} \, d\xi$$

$$(2.35)$$

$$w(x_i, r_i) = - \frac{3r_i}{4\pi} \int_{\ell_1}^{\ell_2} \frac{(a_{j1}+a_{j2}\xi)(x_i-\xi)}{[(x_i-\xi)^2 + r_i^2]^{5/2}} \, d\xi \qquad (2.36)$$

By evaluating the above expressions, again using MACSYMA, one
23

obtains:

$$u(x_i, r_i) = \frac{1}{4\pi} [a_{j1}(H_1 - 3x_i^2 P_1 + 6x_i P_2 - 3P_3)$$

$$+ a_{j2}(H_2 - 3x_i^2 P_2 + 6x_i P_3 - 3P_4)] \qquad (2.37)$$

$$w(x_i, r_i) = \frac{3r_i}{4\pi} [a_{j1}(P_2 - x_i P_1) + a_{j2}(P_3 - x_i P_2)] \qquad (2.38)$$

If use of higher order doublet distribution is necessary, use $-\mu_{j\bar{1}} = -\sum_{K=1}^{M+1} a_{jK} \xi^{K-1}\bar{1}$ to replace μ_j in equations (2.30 and 2.31), and then the general expressions for (ϕ, u, w) are:

$$\phi(x_i, r_i) = -\frac{1}{4\pi} \sum_{K=1}^{M+1} a_{jK}(H_{K+1} - x_i H_K) \qquad (2.39)$$

$$u(x_i, r_i) = \frac{1}{4\pi} \sum_{K=1}^{M+1} a_{jK}(H_K - 3x_i^2 P_K + 6x_i P_{K+1} - 3P_{K+2}) \qquad (2.40)$$

$$w(x_i, r_i) = \frac{3r_i}{4\pi} \sum_{K=1}^{M+1} a_{jK}(P_{K+1} - x_i P_K) \qquad (2.41)$$

2.2.2.5 Constant cross flow doublet distribution. Use of a piecewise constant doublet distribution along the body axis to simulate cross flow has been illustrated in Sketch 2.7.

The jth element (from $x = \ell_1$ to ℓ_2) is a constant strength doublet distribution with doublet axes pointed toward the on-coming flow. The velocity potential function ϕ at a field point "i" due to this element can be expressed as:
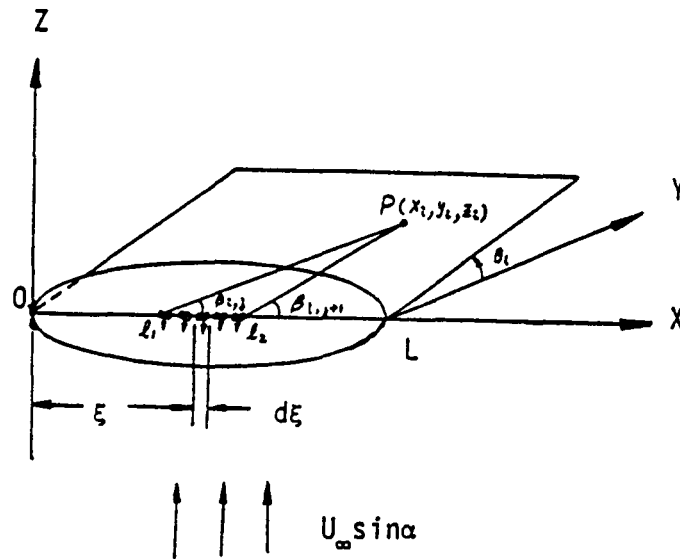
Sketch 2.7 Illustrating axial doublet singularity
'panelling scheme for cross flow

$$\phi_{ij}(x_i, r_i, \theta_i) = \frac{\sin\theta_i}{4\pi} \int_{\ell_1}^{\ell_2} \frac{\mu_j r_i}{[(x_i - \xi)^2 + r_i^2]^{3/2}} \, d\xi \qquad (2.42)$$

The reason that θ_i is involved in the velocity potential
function expression is due to the three dimensional behavior of the
cross flow. This θ_i dependence will be kept in order to make the
expressions derived complete. However, later on, it will be shown
that the doublet strength distribution gotten from solving the
linear equations resulting from the boundary conditions is
independent of the θ location of control points. In this sense, we
can eliminate tne θ_i dependence simply by locating control points on
the top meridian line ($\theta_i = 90^0$). However, if it is desired to cal-
culate the pressure coefficients at points not located on the top or
bottom meridian lines, the θ effect must be included.

By differentiating ϕ_{ij}, three velocity expressions result:

25

$$u(x_i, r_i, \theta_i) = -\frac{3\sin\theta_i}{4\pi} \int_{\ell_1}^{\ell_2} \frac{\mu_j r_i (x_i - \xi) \cdot}{[(x_i - \xi)^2 + r_i^2]^{5/2}} \, d\xi \qquad (2.43)$$

$$w(x_i, r_i, \theta_i) = \frac{\sin\theta_i}{4\pi} \int_{\ell_1}^{\ell_2} \frac{\mu_j}{[(x_i - \xi)^2 + r_i^2]^{3/2}} \, d\xi$$

$$-\frac{3\sin\theta_i}{4\pi} \int_{\ell_1}^{\ell_2} \frac{\mu_j r_i^2}{[(x_i - \xi)^2 + r_i^2]^{5/2}} \, d\xi \qquad (2.44)$$

$$\Theta(x_i, r_i, \theta_i) = \frac{\cos\theta_i}{4\pi} \int_{\ell_1}^{\ell_2} \frac{\mu_j}{[(x_i - \xi)^2 + r_i^2]^{3/2}} \, d\xi \qquad (2.45)$$

If the procedure described in section 1.2.2 is followed, the expressions for velocities will be obtained as follows:

$$u(x_i, r_i, \theta_i) = -\frac{\mu_j \sin\theta_i}{4\pi r_i^2} (\sin^3\beta_{i,j+1} - \sin^3\beta_{i,j}) \qquad (2.46)$$

$$w(x_i, r_i, \theta_i) = \frac{\mu_j \sin\theta_i}{4\pi r_i^2} [2(\cos\beta_{i,j+1} - \cos\beta_{i,j}) - (\cos^3\beta_{i,j+1} - \cos^3\beta_{i,j})]$$

$$(2.47)$$

$$\Theta(x_i, r_i, \theta_i) = -\frac{\mu_j \cos\theta_i}{4\pi r_i^2} (\cos\beta_{i,j+1} - \cos\beta_{i,j}) \qquad (2.48)$$

where the $\beta_{i,j+1}$, $\beta_{i,j}$ have been defined in Sketch 2.7.

In the computer program, a subroutine based on these expressions has been implemented. If the MACSYMA language is used to perform the above integrations, the following forms result for

the constant cross flow doublet:

$$u(x_i,r_i,\theta_i) = - \frac{3\mu_j r_i \sin\theta_i}{4\pi} (x_i P_1 - P_2) \tag{2.49}$$

$$w(x_i,r_i,\theta_i) = \frac{\mu_j \sin\theta_i}{4\pi} H_1 - \frac{3\mu_j r_i^2 \sin\theta_i}{4\pi} P_1 \tag{2.50}$$

$$\oplus (x_i,r_i,\theta_i) = \frac{\mu_j \cos\theta_i}{4\pi} H_1 \tag{2.51}$$

2.2.2.6 Linearly varying cross flow doublet distribution. If the doublet strength is linearly varying over the jth element, $-\mu_j \vec{j} = -(a_{j1} + a_{j2}\xi)\vec{j}$, the velocity potential function and the velocity components at the ith point (x_i,r_i,θ_i) due to the jth panel are given by:

$$\phi(x_i,r_i,\theta_i) = \frac{\sin\theta_i}{4\pi} \int_{\ell_1}^{\ell_2} \frac{(a_{j1} + a_{j2}\xi)r_i}{[(x_i-\xi)^2 + r_i^2]^{3/2}} d\xi \tag{2.52}$$

$$u(x_i,r_i,\theta_i) = - \frac{3\sin\theta_i}{4\pi} \int_{\ell_1}^{\ell_2} \frac{(a_{j1}+a_{j2}\xi)(x_i-\xi)r_i}{[(x_i-\xi)^2 + r_i^2]^{5/2}} d\xi \tag{2.53}$$

$$w(x_i,r_i,\theta_i) = \frac{\sin\theta_i}{4\pi} \int_{\ell_1}^{\ell_2} \frac{a_{j1} + a_{j2}\xi}{[(x_i-\xi)^2 + r_i^2]^{3/2}} d\xi$$

$$- \frac{3\sin\theta_i}{4\pi} \int_{\ell_1}^{\ell_2} \frac{(a_{j1}+a_{j2}\xi)r_i^2}{[(x_i-\xi)^2 + r_i^2]^{5/2}} d\xi \tag{2.54}$$

$$\oplus (x_i,r_i,\theta_i) = \frac{\cos\theta_i}{4\pi} \int_{\ell_1}^{\ell_2} \frac{a_{j1} + a_{j2}\xi}{[(x_i-\xi)^2 + r_i^2]^{3/2}} d\xi \tag{2.55}$$

By using the MACSYMA language, one obtains:

$$u(x_i, r_i, \theta_i) = -\frac{3r_i \sin\theta_i}{4\pi} [a_{j1}(x_i P_1 - P_2) + a_{j2}(x_i P_2 - P_3)] \quad (2.56)$$

$$w(x_i, r_i, \theta_i) = \frac{\sin\theta_i}{4\pi} [a_{j1}(H_1 - 3r_i^2 P_1) + a_{j2}(H_2 - 3r_i^2 P_2)] \quad (2.57)$$

$$\oplus(x_i, r_i, \theta_i) = \frac{\cos\theta_i}{4\pi} [a_{j1}H_1 + a_{j2}H_2] \quad (2.58)$$

The same method applied to arbitrary higher order doublet distributions, using $-\mu_j \vec{\jmath} = -\sum_{K=1}^{M+1} a_{jK} \xi^{K-1} \vec{\jmath}$ to replace μ_j in equations (2.43 to 2.45) results in:

$$u(x_i, r_i, \theta_i) = -\frac{3r_i \sin\theta_i}{4\pi} \sum_{K=1}^{M+1} a_{jK}(x_i P_K - P_{K+1}) \quad (2.59)$$

$$w(x_i, r_i, \theta_i) = \frac{\sin\theta_i}{4\pi} \sum_{K=1}^{M+1} a_{jK}(H_K - 3r_i^2 P_K) \quad (2.60)$$

$$\oplus(x_i, r_i, \theta_i) = \frac{\cos\theta_i}{4\pi} \sum_{K=1}^{M+1} a_{jK}H_K \quad (2.61)$$

2.2.3 Equations for Determining the Strength of Singularities

The expressions for induced velocity components at the ith control point due to the jth element distributed along the body axis (from $x = \ell_1$ to ℓ_2) have been derived in section 2.2.2. When the contributions from individual elements are added together, the total induced velocity at the ith control point can be expressed in terms of the unknown strengths of the singularities at each

element. These unknown strengths can be specified as arbitrary order polynomial functions. In the present studies, constant (order M = 0) and linearly varying (order M = 1) cases have been considered. When these expressions are substituted back into equation (2.5) or equation (2.8) to satisfy the no penetration requirement on the body surface, a system of linear algebraic equations for the unknown polynomial coefficients is obtained, which is then solved for the unknown strengths. Once the strength distribution is known, the velocity and pressure coefficient can be calculated at any field point outside the body, as well as on the body surface.

Since the solution procedures are essentially the same in either the axial flow or cross flow calculations, therefore, only the source singularity distribution in axial uniform flow is presented as an example. There is a slight difference in using the linearly varying doublet as the singularity in either the axial or cross flow calculation. This difference will be described subsequently.

The induced velocity components at the ith control point due to N elements distributed along the body axis (see Sketch 2.8) are given as follows:

$$u(x_i,r_i) = \frac{1}{4\pi} \sum_{j=1}^{N} \left[\sum_{K=1}^{M+1} a_{jK}(x_i H_K - H_{K+1}) \right] \tag{2.62}$$

$$w(x_i,r_i) = \frac{r_i}{4\pi} \sum_{j=1}^{N} \left[\sum_{K=1}^{M+1} a_{jK} H_K \right] \tag{2.63}$$

where M is the degree of the polynomial function, and a_{jk} is the unknown coefficient of the singularity distribution element "j".
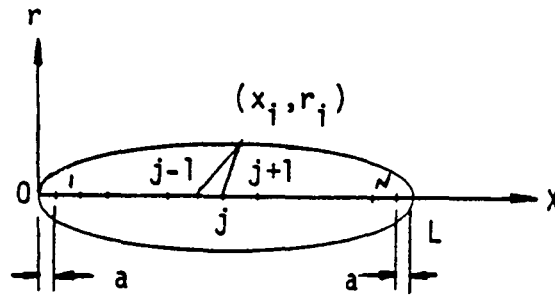
Sketch 2.8   Illustrating axial source singularity
panel distribution for equations (2.62 & 2.63)

If the constant source is chosen as the singularity type(M = 0), there are N unknown coefficients and a N*N linear system results from applying the no penetration boundary condition at the selected N control points on the body surface. Gauss elimination methods have been employed herein to solve for the unknowns. If M = 1, linearly varying source, is chosen as the singularity, there are two unknowns for each element. However, continuity of the singularity distribution at the junction point between two neighboring elements provides another N-1 equations. This continuity requirement is valid so long as the body slope and curvature are continuous. The general form of these N-1 continuity equations is given as:

$$a_{j,1} + a_{j,2}\ell_j = a_{j+1,1} + a_{j+1,2}\ell_j \quad j = 1,2 \ldots N-1 \quad (2.64)$$

where ℓ_j is the x coordinate of the junction point of elements "j" and "j+1".

The last equation required is a closure condition, due to the

30

fact that the net efflux of the source distribution should be zero for a closed body, and is given by

$$\sum_{j=1}^{N} (a_{j,1} L_j + \frac{1}{2} a_{j,2} L_j^2) = 0 \qquad (2.65)$$

where L_j is the length of the jth element. Hence, the 2N unknowns may be determined from the 2N equations developed above. If higher order singularities are used ($M \geq 2$), then corresponding higher order derivatives of the source strength should be continuous, at least for bodies which are sufficiently smooth. For example, for the second order source ($M = 2$), continuity of the slope of the source strength should be enforced at the juncture between two neighboring elements.

As mentioned above, when the linearly varying doublet singularity is used to represent the body, the last closure condition is no longer applicable. The form of this last condition for a general body of revolution is not known. However, in the present studies, a condition of zero strength at the starting and ending points of the singularity distribution has been used to perform the calculations. Imposition of some more fundamental condition on the linear doublet distribution may improve the solution accuracy for this singularity type.

2.3 Analytical Solution for Ellipsoidal Body

The potential flow past an ellipsoidal body was solved exactly by Lamb (1932). Wang (1970) gave an explicit expression for the surface velocity potential function ϕ in terms of two surface coordinates μ and θ (see Sketch 2.9). Here, ($-1 \leq \mu \leq 1$) is constant along the parallels and θ is constant along the

meridians. It should be understood that no restrictions on angle of attack or slenderness ratio was imposed in the solution. By differentiating the velocity potential, Φ, and utilizing the Bernoulli's equation, a closed form of the surface pressure coefficient, C_p, is obtained as:
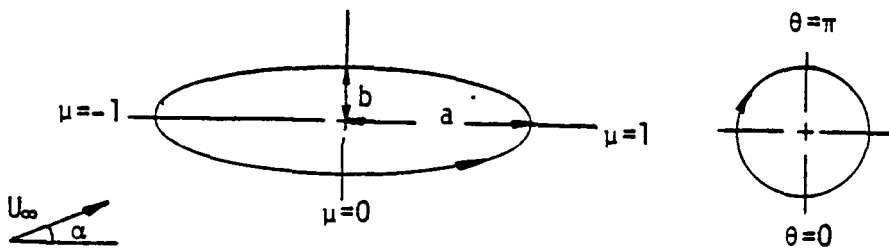
Sketch 2.9 Coordinates scheme for equation (2.66)

$$C_p = 1 - \left\{ \left[\frac{(1 + K_a)(\cos\alpha)(1 - \mu^2)^{1/2} + (\frac{b}{a})(1 + K_c)(\sin\alpha)\mu\cos\theta}{(1 - e^2\mu^2)^{1/2}} \right]^2 \right.$$

$$\left. + \left[(1 + K_c)\sin\alpha \, \sin\theta \right]^2 \right\} \tag{2.66}$$
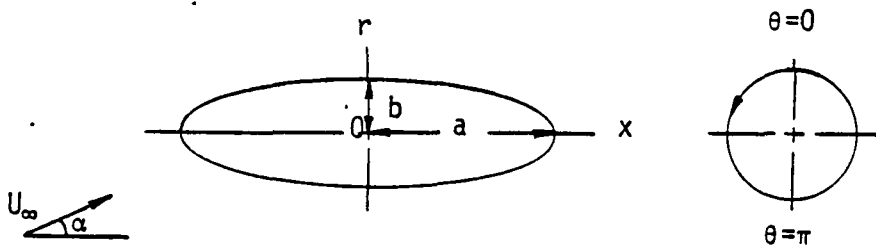
where

$$e = \left[1 - \frac{b^2}{a^2} \right]^{1/2} \text{ , the eccentricity}$$

$$K_a = \frac{\frac{1}{2e} \log \frac{1+e}{1-e} - 1}{\left[\frac{1}{1-e^2} - \frac{1}{2e} \log \frac{1+e}{1-e} \right]} \text{ , the axial coefficient of virtual mass}$$

$$K_c = \frac{1}{1+2K_a} \text{ , the cross coefficient of virtual mass}$$

32

A similar, explicit expression for Cp has been given by Cebeci, Kattab and Stewartson (1980). Another expression for Cp for an ellipsoid at angle of attack has been given in Schlichting and Truckenbrodt (1979), expressed in cylindrical coordinates (see Sketch 2.10). The pressure coefficient, Cp, was expressed in the following form:

Sketch 2.10 Coordinates scheme for equation (2.67)

$$C_p = [1 - A^2 \frac{1 - (\frac{x}{a})^2}{1-[1 - \frac{b^2}{a^2}](\frac{x}{a})^2}] + 2B \frac{b}{a} \frac{\frac{x}{a}\sqrt{1-(\frac{x}{a})^2}\cos\theta}{1-[1- \frac{b^2}{a^2}](\frac{x}{a})^2} \alpha \quad (2.67)$$

where

$$A = \frac{2}{2-\alpha_0} , \qquad B = \frac{8}{4-\alpha_0^2}$$

$$\alpha_0 = \frac{2(\frac{b}{a})^2}{(1 - \frac{b^2}{a^2})^{3/2}} \{\tanh^{-1}[(1 - \frac{b^2}{a^2})^{1/2}] - (1 - \frac{b^2}{a^2})^{1/2}\}$$

It is easy to show that both expressions are identical for flow

33

without angle of attack ($\alpha = 0^0$). However, an appreciable error
results from equation (2.67) for the case of the flow at an angle of
attack (see Table 1 and Figure 1). Numerical experiments show;
at $\alpha = 5^0$, the discrepancy from the exact solution (Lamb) is about
7%; while at $\alpha = 10^0$, more than 30% discrepancy results, which is
totally unacceptable in any kind of flow calculation. Schlichting
and Truckenbrodt indicated that this equation is only good for flow
at small angles of attack, but such a large discrepancy is
unexpected. It was found that the small α equation (2.67) can be
directly derived from the exact equation (2.66) by assuming α is
small, so that $\cos\alpha \sim 1$ and $\sin\alpha \sim \alpha$, and neglecting all terms of
order α^2. Therefore, while equation (2.67) is the correct
expression for Cp for small α, use of equation (2.66) is recommended
instead of (2.67) for all values of α. In the comparisons between
the present numerical model and the analytical solution to be
presented in the following section, only the full expression given
by equation (2.66) has been utilized.

2.4 Accuracy of Method

It has been found that the solution accuracy of the axial
singularity method is largely dependent upon the following four
factors; (1) singularity type, (2) number of discrete elements, (3)
inset panelling technique, and (4) panelling scheme. In this work,
a systematic evaluation has been conducted to determine the error
sensitivities of the solution for an ellipsoidal body to these
factors. The motivation to do these studies is basically due to the
fact that decisions on these variables must be made a priori for any
particular problem, and will usually be influenced by the problem

34

and the information desired from the solution. It is expected that the present study might provide some guidelines for more general bodies.

The test geometry has been chosen to be an ellipsoid of SR=5, because the exact solution previously described already is known, and it is a suitable geometry to show the error sensitivities for all four factors mentioned above. Similar studies of SR=2 and SR=10 ellipsoids have yielded solution of accuracies comparable to those presented herein for SR=5. All comparisons have been made using root mean square error for comparison. This error calculation has been based on pressure coefficients calculated at 40 points equally distributed along a meridian line on the body surface. The root mean square error is defined as

$$\text{Error} = \sqrt{\frac{\sum\limits_{i=1}^{40} (CPE_i - CPN_i)^2}{40}} \qquad (2.68)$$

where CPE_i is the exact pressure coefficient at the ith point and CPN_i is the numerical pressure coefficient at the ith point.

The same fractional locations of the 40 points have been used, independent of the control point locations.

2.4.1 Test 1: Axisymmetric Flow

A set of results for 19 typical cases for the SR=5 ellipsoid at $\alpha = 0^0$ are listed in Table 2. Through comparisons of the error magnitudes, one can easily find the individual contributions to solution accuracy due to one factor by holding the others fixed.

2.4.1.1 Element number. By comparing configurations (1 and 3), it is seen that the solution is improved by utilizing more elements to represent the body. Also, the pair of configurations (2 and 9) reinforce more dramatically the same conclusion. In fact, increasing the number of elements generally improves the solution accuracy for any numerical calculation procedure. In the present studies, 20 elements are considered sufficient to represent the ellipsoid.

2.4.1.2 Singularity type. By comparing configurations (5, 10, 12 and 13), it may be seen that the constant doublet is the least accurate among the four types of singularity, being inadequate to represent the source like nature of flow near the stagnation point. Therefore, it has not been considered in further application. Next, the constant source distribution has the same accuracy as the linearly varying doublet. Finally, the linearly varying source yields the best solution, in the test case, for a fixed number of elements, and is recommended for application to other more complicated geometries.

The singularity strength and Cp distribution along the body axis for these four configurations have been shown in Figures 2 and 3. Note that the source strength predicted by slender body theory has been shown in Figure 2 for comparison. Since the numerical solution error in Figure 3 is almost indistinguishable, Table 3 has been prepared to display the deviations of these four solutions from the exact solution. Note that the error in Cp for the linearly varying source distribution is on the order of 10^{-5} over much of the ellipsoid, with larger errors near the stagnation points.

As a fairer comparison of the relative accuracies of the constant and linear source singularities for approximately equal computational cost, configuration pairs (13, 17) and (14, 18) may be compared. These test pairs have equal matrix sizes and thus should have nearly equal run times and costs. It is seen both for equal sized element (configurations 13, 17) and cosine spacing (configurations 14, 18) use of 40 constant source singularities leads to better accuracy than 20 linear sources. However, comparison of pairs (5, 19) displays an opposite trend for a sparser element distribution. That is, ten equal sized linear sources yield a more accurate solution than 20 constant source singularities. Based on these limited studies it is apparent that use of higher order singularities may or may not result in reduced computational cost.

2.4.1.3 Panelling scheme. The semi-circle cosine type panel distribution has been used previously by many authors in choosing the chordwise and spanwise locations of vortex points as well as control points (see, for example, Lan, 1974). This panelling scheme is based on the assumption that better results might be obtained if finer elements are used in regions of rapid variation of sectional properties. Of course, qualitative properties of the section must be known a priori. It has been proven effective and accurate through numerical experiments in thin wing theory. Therefore, it is believed to be reasonable to apply this technique in the present body calculation. Two comparisons have been made; first, between configurations 5 and 9, and second, configurations 13 and 14 of Table 2. Both comparisons give the positive answer, that a

tremendous improvement in solution accuracy is obtained from using cosine spacing instead of an equal spacing scheme. Hence, use of cosine spacing is strongly recommended, wherever applicable, in other flow calculations.

2.4.1.4 Inset panelling technique. Zedan and Dalton (1980) concluded that use of the submerged panelling technique would lead to a more accurate solution for bodies with either a blunt nose or tail. In the present studies, it has been found that the optimal inset distance for the ellipsoid of SR=5 is about 1% of the body total length (configurations 3 to 7). The root mean square error versus submerged distance is shown in Figure 4.

For ellipsoids of different slenderness ratios, the optimal inset distance must be varied with the magnitude of the local radius of the nose and tail. This ellipsoid nose radius is found to be b/SR, where b is the length of the minor axis of the ellipsoid. Numerical experiments have shown that 6% of the body length is the optimal inset value for a SR=2 ellipsoid, and 0.25% of the body length is optimal for a SR=10 ellipsoid. Table 4 (a), (b) display the relation between the inset value and the associated root mean square error. All test configurations have been run using 20 cosine space linearly varying source elements.

It has been discovered that a nearly constant relationship exists for the optimal inset value for other slenderness ratio ellipsoids, as shown the following brief table, prepared for 20 cosine spaced elements. Here R is the nose radius of curvature.

TABLE 2.1 Optimal inset value for various SR ellipsoid

				optimal inset of singularity line			
SR	a	b	R	% of L	% of a	% of b	(% of b)/R
10	10	1	0.1	0.25	0.5	5.	50.
5	5	1	0.2	1	2.	10.	50.
2	2	1	0.5	6	12.	24.	48.

Notice that the optimal inset value is a constant fraction of the ellipsoid nose radius. Therefore, the optimal inset value for all ellipsoidal bodies should be governed by the following expression:

$$\text{optimal inset value in terms of the body total length (\%)} = \frac{25}{SR^2} \qquad (2.69)$$

Similar results were found using 20 equal sized elements, but the constant was changed slightly so an effect of the length of the element nearest the nose could be seen.

Table 4 (c) shows the root mean square Cp error for axisymmetric flow past a series of ellipsoids using the suggested inset value calculated from equation (2.69). Undoubtedly, this equation offers a very accurate Cp solution, and it's use is recommended in further calculations for blunt nosed ellipsoidal bodies. Figure 5 displays the Cp distributions for axisymmetric flow past SR=2, 5 and 10 ellipsoids using the optimal inset panelling scheme.

2.4.1.5 Optimal solution. By combining all of the above favorable factors together, an optimal representation for axisymmetric flow past a SR=5 ellipsoid may be determined as 20 discrete elements of cosine spaced linearly varying source distribution with a 1% inset panelling scheme. This configuration does give the minimum error in Cp for 20 elements of 0.000063. Figures 6 and 7 display the pressure coefficient and the error distributions. Note that the numerical solution matches the exact solution very well on the whole body surface, with the largest errors occurring near the nose and tail. Also shown, for completeness in Figure 6, is the Cp distribution calculated by slender body theory using the source distribution shown in Figure 2. Slender body theory is in error nominally by 15% over the middle 80% of the body. Similar calculations at SR=10 show approximately 4% error.

2.4.2 Test 2: Inclined Flow at 5° Angle of Attack

A procedure similar to that performed for α = 0^0 above, is now repeated for α = 5^0 to investigate the error sensitivities of panelling and singularity variables in the cross flow calculation. Since the inclined flow can be found as the superposition of a pure axial flow and the corresponding cross flow, one can fix the parameters of the axial flow part of the calculation, and allow only the cross flow calculation singularity and panelling to vary. A choice of 20 discrete elements, for a cosine spaced constant source distribution with 1% inset panelling will allow sufficient accuracy in the axial calculations to see error changes for different crossflow configurations. There are nine such cases listed in Table 5. All results have been calculated along a θ = 33.75^0 meridian

40

line on the body surface. Since the root mean square error in Cp at $\theta = 33.75^0$ is very small, for m -t choices of panelling and inset, detailed plots of singularity strength and Cp distribution have not been presented. It was also found that the root mean square error in Cp values at other θ values were essentially identical to those presented in Table 2, and that the singularity strength distribution solutions were unchanged by different θ meridian line locations of the control points.

2.4.2.1 Singularity type. There are only two choices for singularity type in the cross flow calculation, either constant doublet or linearly varying doublet. Again, it was found that the linearly varying doublet yields better results. Comparing configurations 1 and 5, the root mean square error is reduced from 0.019056 to 0.005749. Comparisons between configurations 2 and 6, as well as 4 and 8, result in the same conclusion.

2.4.2.2 Panelling scheme. By comparing configurations 1 and 3 , it is again found that cosine spacing is better than equal spacing for solution accuracy. Reductions of root mean square error also appear in the test pairs configurations 2 and 4 or 6 and 8.

2.4.2.3 Inset panelling. The inset panelling technique also improves the solution accuracy in the cross flow calculation. This technique is recommended for use for blunt body calculations under the present singularity panel method. Note that if no inset is used for the ellipsoid at angle of attack (not the recommended panelling scheme), use of cosine spacing of the cross flow linearly varying doublet actually degrades the solution accuracy (see configurations

41

5, 7). This is the only exception in consistency to the conclusions made previously for the axial flow analysis. The reason for this different trend is not known.

2.4.2.4 Optimal solution. To find the best panelling arrangement to represent the inclined flow past a SR=5 ellipsoidal body, we use the optimal case for axial flow, combined with the linearly varying doublet with cosine spacing and 1% inset panelling for the cross flow. This is configuration 9 in Table 5 which does yield the minimum error of all cases tested. Based on these results, use of this panelling scheme is strongly recommended for blunt body calculations. Figures (8 through 12) display the singularity strength and Cp distributions of this optimal panelling arrangement at several additional values of α between 5° and 30°. The numerical solutions are in excellent agreement with the exact solution everywhere on the body surface.

CHAPTER 3

VORTEX LATTICE SURFACE SINGULARITY METHOD
FOR ARBITRARY BODY OF REVOLUTION

3.1 Literature Survey

The surface singularity method is one of the most reliable methods available to compute the potential flow past a body of arbitrary geometry. By utilizing this method, which is based on application of Green's theorem, the original three dimensional flow problem is reduced to an integral equation over the given boundary surface of the flow region, comprised of the body surface and/or wake. The Green's theorem expression represents the disturbance velocity potential ϕ at any point P in the flow field as the integrated effect of source and doublet (or equivalently vorticity) singularities on the body surface. The mathematical statement is

$$\phi(P) = -\frac{1}{4\pi} \iint_S (\frac{1}{r} \text{ grad } \phi - \phi \text{ grad } \frac{1}{r}) \cdot \vec{n} \text{ ds} \qquad (3.1)$$

To reduce this expression to one which contains either source only or doublet only, consider a second function, ϕ_1, which is harmonic inside the body, and adding the Green's theorem expression for ϕ_1 evaluated outside the body, one obtains

$$\phi(P) = -\frac{1}{4\pi} \iint_S [\frac{1}{r} \text{ grad } (\phi - \phi_1) - (\phi - \phi_1)\text{grad } \frac{1}{r}] \cdot \vec{n} \text{ ds} \quad (3.2)$$

43

Choice of a unique ϕ_1 solution such that $\phi_1 = \phi$ on s results in a source only method, while fixing ϕ_1 such that $\frac{\partial \phi_1}{\partial n} = \frac{\partial \phi}{\partial n}$ on the boundary yields a doublet singularity method. Also possible are various combinations of source and doublet singularities.

Mathematically, these singularity methods will yield equivalent results independent of which representation may be used. However, numerical differences do occur when different schemes are used. For example, sources are more effective near stagnation points, and doublets are more effective in generating and controlling surface tangential velocities, since flow near a stagnation point is source-like. Intuitively, then, one might expect some benefits to be possible from use of the combined source-vortex or source-doublet methods. This idea has been investigated and proven correct in numerical experiments (Bristow, 1976).

In summarizing related previous work, discussion of two main areas will be given because these two approaches have each had a profound influence on the present study. In fact, the computer program which has been developed herein to implement the surface singularity method is essentially the same as the method due to Asfar et al. (1979) described below, except for some changes in calculation methods and program capability.

The first approach, due for example to Hess and Smith (1962, 1967) utilized a source density distribution over the body surface. Application of the no-penetration boundary condition on the body surface yielded a Fredholm integral equation of the second kind for the source density. The profile curves defining the body were approximated by a large number of small straight or curved line

44

rectangular elements. The source density was then assumed constant over each element. Thus, the contribution of each element to the integral expression for the velocity could be obtained by taking this constant but unknown source density out of the integral and then performing the integration of known geometric quantities over the element. Satisfying the integral equation at a control point on each element led to a system of linear equations for the source densities. Once these densities were evaluated by solving this linear system, straightforward substitution in the appropriate velocity expressions yielded the velocity distribution and hence the pressure distribution.

The second technique (see, for example, Kandil et al., 1974, 1977; Atta, 1978; Asfar et al., 1979) utilized surface distributions of vorticity, in the form of a vortex lattice, and sources, to represent the body. The surface source distribution used by Asfar et al. (1979) was predetermined in such a way that the source on any given element, when acting alone, generated a velocity field which cancelled a prescribed fraction of the normal component of the free-stream velocity at the control point of that element. The vortex lattice was formed by a constant strength quadrilateral vortex element, except at the nose or tail where triangular elements were used. Description of the formation of the vortex lattice have been given by Crigler (1957), Lamar (1971), and Kandil et al. (1974, 1977). Using the element loop circulations (which automatically satisfy the spatial conservation of circulation) as the unknowns, and satisfying the no-penetration boundary condition for all elements on the body surface, a strongly diagonal influence

coefficient matrix of linear equations was generated. Then the unknown strengths of circulation for each element were obtained by solving this linear system. Since the governing equation is elliptic, all aerodynamic parameters were calculated by summing up the individual contributions from source singularities and vortex lattice circulation elements. Atta (1978) has studied various problem formulations in detail, and found the loop circulation formulation to be much more convenient than a branch circulation formulation.

Both methods have been found to yield fairly accurate solutions, by employing a large number of panels, with a resulting high computational cost. According to Asfar et al. (1979), for blunt bodies, the second approach of using a combination of source and vortex singularities was superior to either the vortex lattice only (a special case of the second method, when the source strength is zero) or the source panel method; while for slender bodies, the vortex lattice method appeared to be superior to the source because of the slenderness of the body. This assertion provides another justification for using the vortex lattice method in the present surface singularity theory.

3.2 Formulation of the Problem

The problem formulation for the present method is identical to that given in Chapter 1, except that grad F has been replaced by $\vec{n}$, the outward unit normal vector on the body surface. This formulation is more convenient for complicated bodies for which an analytical expression for F is unknown.

46

3.2.1 Numerical Scheme

The body under consideration has been located in a right handed cartesian coordinate system with the X axis oriented in opposition to the oncoming flow (see Sketch 3.1). The undisturbed free-stream is, in general, oriented at an angle of attack, α, with respect to the X axis, in the XZ plane. The body has been described by a number of discrete points on it's surface. In the present work, where the surface of the body was described by an analytic function, these body points have been generated by the program itself. For more complicated geometry, the program user must define these body points manually.

The surface points have been organized in "rows" and "columns" as indicated in Sketch 3.1. The lattice consists of short straight lines connecting the body points, thereby forming quadrilateral elements, with the exception of the nose and tail, where these lines converge so that the elements are triangular. A system of elements which are chosen to be quadrilaterals of aspect ratio of nearly unity has been found to yield the best results. The velocity fields generated from the above scheme satisfy equations (1.4 and 1.6) regardless of the circulation strengths. It only remains, therefore, to choose their strengths so that equation (1.5) will be satisfied. Equation (1.5) can also be manipulated into a set of algebraic equations, by substituting the following expressions into the equation:

$$\nabla \phi_i = \sum_{j=1}^{N} (P_{ij}\Gamma_j \vec{i} + q_{ij}\Gamma_j \vec{j} + r_{ij}\Gamma_j \vec{k}) \qquad (3.3)$$

47

$$\vec{n}_i = A_i \vec{i} + B_i \vec{j} + C_i \vec{k} \qquad (3.4)$$

$$\vec{U}_\infty = -U_\infty \cos\alpha \vec{i} - U_\infty \sin\alpha \vec{k} \qquad (3.5)$$

where the subscript i denotes the associated quantity evaluated at the control point "i", Γ_j is the unknown strength of circulation of element "j"; P_{ij}, q_{ij}, r_{ij} are the influence coefficients, which give the velocities in the X, Y and Z directions at the ith control point due to a unit loop circulation around the jth element, and A_i, B_i, C_i are the direction cosines of the surface unit normal at the control point "i". Expressions for the influence coefficients will be given subsequently.

Substitution of equations (3.3 to 3.5) into equation (1.5), yields a set of equations for the unknown loop circulations as:
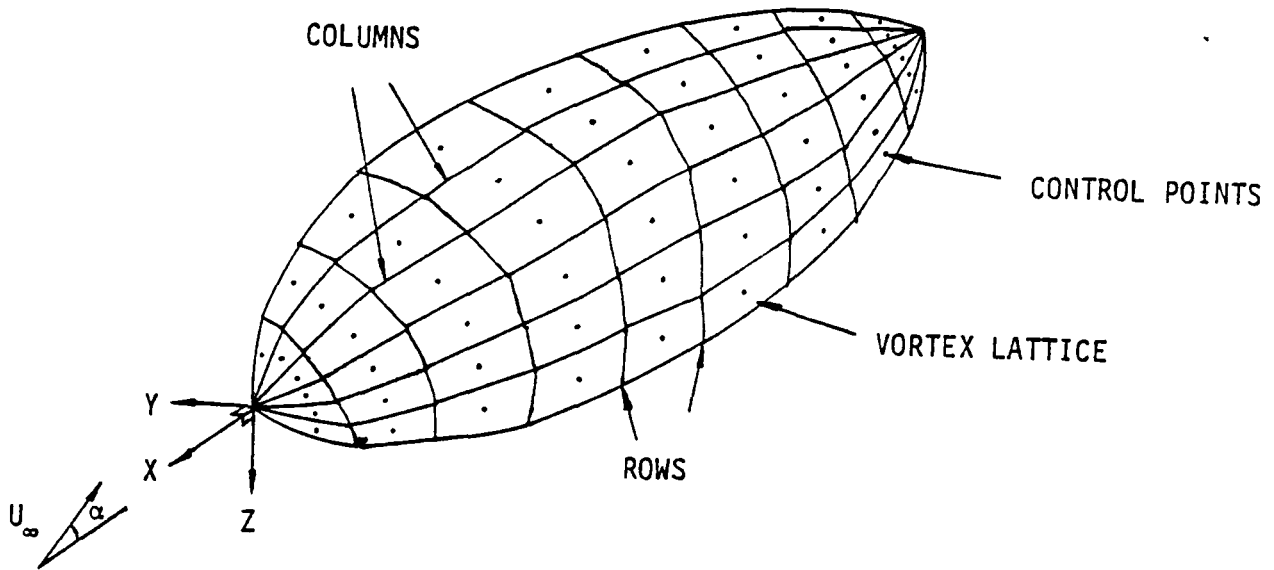
Sketch 3.1 Coordinate scheme for the problem

$$A_i \sum_{j=1}^{N} P_{ij}\Gamma_j + B_i \sum_{j=1}^{N} q_{ij}\Gamma_j + C_i \sum_{j=1}^{N} r_{ij}\Gamma_j$$

$$= U_\infty \cos\alpha \; A_i + U_\infty \sin\alpha \; C_i \qquad \text{for } i = 1, 2, \dots N \qquad (3.6)$$

48

The sequence of numerical techniques which are involved in solving this linear system include decisions as to how to efficiently store the large influence coefficient matrix, selection of a linear equation solver, and reduction of the size of the linear system due to symmetric properties, as has been well documented by Kandil (1974) and Asfar et al. (1979). The following two sections are devoted to development of the explicit expressions for the constant coefficients which appear in equation (3.6).
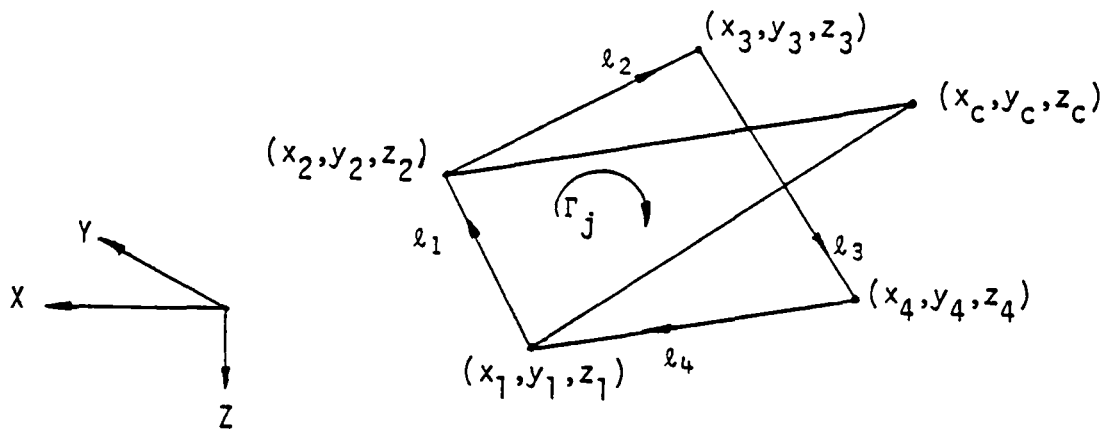
(a) A closed loop vortex element
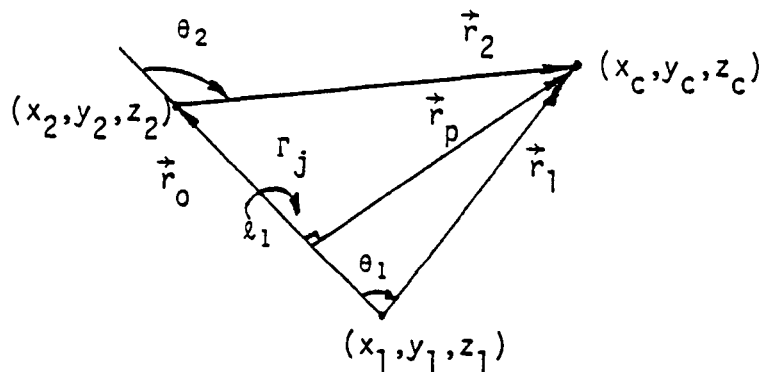
(b) A finite length vortex filament

Sketch 3.2 Nomenclature for calculating the induced velocity

3.2.2 Calculation of Influence Coefficients $p_{ij}-q_{ij}-r_{ij}-$

The total induced velocity at the ith control point due to a discrete vortex element "j", with the constant strength of circulation along the sides (see Sketch 3.3.a), can be expressed in the following symbolic form:

$$\vec{V}_{induced} = p_{ij}\Gamma_j\vec{i} + q_{ij}\Gamma_j\vec{j} + r_{ij}\Gamma_j\vec{k}$$

$$= \sum_{\ell=1}^{4} (u_{i\ell}\Gamma_j\vec{i} + v_{i\ell}\Gamma_j\vec{j} + w_{i\ell}\Gamma_j\vec{k}) \qquad (3.7)$$

The induced velocity due to a single finite vortex segment (see Sketch 3.2.b) is calculated by using the Biot-Savart law (see Karamcheti, 1966).

$$\vec{V}_{\ell 1} = \frac{\Gamma_j}{4\pi r_p} \int_{\theta_1}^{\theta_2} \sin\theta \, d\theta \, \vec{e}_v = \frac{\Gamma_j}{4\pi r_p} (\cos\theta_1 - \cos\theta_2)\vec{e}_v \quad (3.8)$$

$$\text{where} \quad r_p = \frac{|\vec{r}_1 \times \vec{r}_2|}{r_0} \, , \quad \cos\theta_1 = \frac{\vec{r}_0 \cdot \vec{r}_1}{r_0 r_1} \, , \quad \cos\theta_2 = \frac{\vec{r}_0 \cdot \vec{r}_2}{r_0 r_2} \quad (3.9)$$

and $\vec{e}_v$, the direction of the induced velocity, is given by the unit vector

$$\vec{e}_v = \frac{\vec{r}_1 \times \vec{r}_2}{|\vec{r}_1 \times \vec{r}_2|} \qquad (3.10)$$

substituting equations (3.9 and 3.10) into equation (3.8), a vector expression for this induced velocity can be obtained as follows:

$$\vec{V}_{\ell 1} = \frac{\Gamma_j}{4\pi} \frac{\vec{r}_1 \times \vec{r}_2}{|\vec{r}_1 \times \vec{r}_2|^2} [\vec{r}_0 \cdot (\frac{\vec{r}_1}{r_1} - \frac{\vec{r}_2}{r_2})] \qquad (3.11)$$

50

where $\quad \vec{r}_0 = (x_2 - x_1)\vec{i} + (y_2 - y_1)\vec{j} + (z_2 - z_1)\vec{k}$

$$\vec{r}_1 = (x_c - x_1)\vec{i} + (y_c - y_1)\vec{j} + (z_c - z_1)\vec{k}$$

$$\vec{r}_2 = (x_c - x_2)\vec{i} + (y_c - y_2)\vec{j} + (z_c - z_2)\vec{k} \qquad (3.12)$$

$\vec{V}_{\ell 2}$, $\vec{V}_{\ell 3}$, $\vec{V}_{\ell 4}$ are calculated in the same way. By summing the contribution of each segment together, P_{ij}, q_{ij}, and r_{ij} are given by:

$$P_{ij} = \frac{1}{4\pi} \sum_{\ell=1}^{4} \frac{(y_c - y_\ell)(z_c - z_{\ell+1}) - (y_c - y_{\ell+1})(z_c - z_\ell)}{W_{\ell 1}} (W_{\ell 2} - W_{\ell 3})$$

$$q_{ij} = \frac{1}{4\pi} \sum_{\ell=1}^{4} \frac{(x_c - x_{\ell+1})(z_c - z_\ell) - (x_c - x_\ell)(z_c - z_{\ell+1})}{W_{\ell 1}} (W_{\ell 2} - W_{\ell 3})$$

$$r_{ij} = \frac{1}{4\pi} \sum_{\ell=1}^{4} \frac{(x_c - x_\ell)(y_c - y_{\ell+1}) - (x_c - x_{\ell+1})(y_c - y_\ell)}{W_{\ell 1}} (W_{\ell 2} - W_{\ell 3})$$

$$\qquad (3.13)$$

where

$$W_{\ell 1} = [(y_c - y_\ell)(z_c - z_{\ell+1}) - (y_c - y_{\ell+1})(z_c - z_\ell)]^2$$

$$+ [(x_c - x_\ell)(z_c - z_{\ell+1}) - (x_c - x_{\ell+1})(z_c - z_\ell)]^2$$

$$+ [(x_c - x_\ell)(y_c - y_{\ell+1}) - (x_c - x_{\ell+1})(y_c - y_\ell)]^2 \qquad (3.14)$$

$$W_{\ell 2} = \frac{(x_{\ell+1} - x_\ell)(x_c - x_\ell) + (y_{\ell+1} - y_\ell)(y_c - y_\ell) + (z_{\ell+1} - z_\ell)(z_c - z_\ell)}{\sqrt{(x_c - x_\ell)^2 + (y_c - y_\ell)^2 + (z_c - z_\ell)^2}}$$

$$W_{\ell 3} = \frac{(x_{\ell+1} - x_\ell)(x_c - x_{\ell+1}) + (y_{\ell+1} - y_\ell)(y_c - y_{\ell+1}) + (z_{\ell+1} - z_\ell)(z_c - z_{\ell+1})}{\sqrt{(x_c - x_{\ell+1})^2 + (y_c - y_{\ell+1})^2 + (z_c - z_{\ell+1})^2}}$$

51

These expressions have been implemented in a FORTRAN computer program to compute the velocities due to a closed loop discrete vortex element. Note that the index of $\ell+1$ is set equal to 1 when ℓ is 4.

3.2.3 Unit Normal Vector Calculation and Control Point Selection

The unit normal vector and the control point coordinates can be obtained through algebraic combination of the four given element corner points (see Sketch 3.3), as is now described.
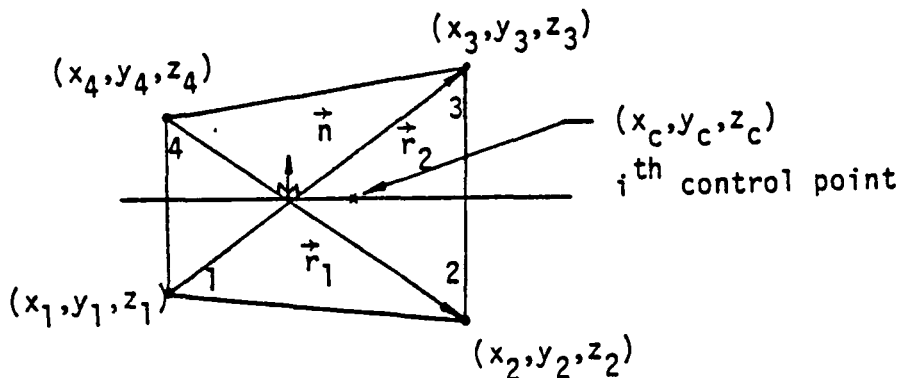
Sketch 3.3 Nomenclature for calculating the unit normal vector

In order to simplify the geometry calculation, it will be assumed that the element is planar; that is, the four points defining a panel element all lie in the same plane. This assumption has been satisfied by the axisymmetric bodies studied in the present work.

3.2.3.1 Unit normal vector calculation. From equation (3.4), the unit normal vector is defined as $\vec{n}_i = A_i \ \vec{i} + B_i \ \vec{j} + C_i \ \vec{k}$, where A_i, B_i, and C_i are constant coefficients which are determined by the element geometry. $\vec{n}_i$ can be represented by $\dfrac{\vec{r}_1 \times \vec{r}_2}{|\vec{r}_1 \times \vec{r}_2|}$, where

52

$$\vec{r}_1 = (x_2 - x_4)\, \vec{i} + (y_2 - y_4)\, \vec{j} + (z_2 - z_4)\, \vec{k}$$

$$\vec{r}_2 = (x_3 - x_1)\, \vec{i} + (y_3 - y_1)\, \vec{j} + (z_3 - z_1)\, \vec{k} \qquad (3.15)$$

Therefore,

$$\vec{r}_1 \times \vec{r}_2 = [(y_2 - y_4)(z_3 - z_1) - (y_3 - y_1)(z_2 - z_4)]\, \vec{i}$$

$$+ [(x_3 - x_1)(z_2 - z_4) - (x_2 - x_4)(z_3 - z_1)]\, \vec{j}$$

$$+ [(x_2 - x_4)(y_3 - y_1) - (x_3 - x_1)(y_2 - y_4)]\, \vec{k}$$

$$= A' \, \vec{i} + B' \, \vec{j} + C' \, \vec{k} \qquad (3.16)$$

By definition, then

$$A_i = \frac{A'}{\sqrt{(A')^2 + (B')^2 + (C')^2}}$$

$$B_i = \frac{B'}{\sqrt{(A')^2 + (B')^2 + (C')^2}}$$

$$C_i = \frac{C'}{\sqrt{(A')^2 + (B')^2 + (C')^2}} \qquad (3.17)$$

where

$$A' = (y_2 - y_4)(z_3 - z_1) - (y_3 - y_1)(z_2 - z_4)$$

$$B' = (x_3 - x_1)(z_2 - z_4) - (x_2 - x_4)(z_3 - z_1)$$

$$C' = (x_2 - x_4)(y_3 - y_1) - (x_3 - x_1)(y_2 - y_4) \qquad (3.18)$$

53

The choice of location of the element control point, where the no-penetration boundary condition is satisfied, is crucial due to the singular nature of the discrete vortex filaments. Following Hess and Smith (1962), Asfar et al. (1979) concluded that the best results were obtained when the control points were located so that the normal component of self-induced velocity due to the closed loop vortex filament at it's own control point is a minimum (known as the "null point" according to Hess and Smith). These minimum self-induced velocity points were located through a tedious search technique. The search scheme is costly and is restricted to problems of fixed geometry. For panels with edge separation (for example in the wing problem), this has to be repeated for the same panel at each iteration. Hence it is not a practical scheme for the wing-body combination problem. Therefore, in the present study, this scheme has not been used. Instead, the centroid of the panel area has been chosen as the control point location, since for the axisymmetric bodies studied, all panels are planar. The advantage of this choice of location is the ease of calculation of the centroid, provided there is not too much difference for the control point location between these two modes. Numerical experiments have proven that this difference is small for both rectangular and triangular elements. The details of calculating the centroid and the panel area for a typical quadrilateral element is given in Appendix B. Also shown in Appendix B are the results of the numerical experiments comparing self-induced velocities for various control point locations.

54

3.2.4 Pressure Coefficient Calculation

Once the linear system given by equation (3.6) has been solved for the unknown circulations, the pressure coefficient at each point on the surface of the body is calculated by using Bernoulli's equation,

$$c_p = 1 - \frac{V_t^2}{U_\infty^2} \qquad (3.19)$$

Here, V_t is the total tangential velocity of the flow at the control point, and is evaluated, as described in Kandil et al. (1977), as the sum of 3 parts; first, the part due to the influence of all the vortex loop elements in the lattice at the control point, second, the contribution of the free stream velocity, and third, the velocity jump across the vortex sheet. The third term is obtained by estimating an equivalent continuous vortex sheet from the lumped vortex filaments. This contribution is to account for the self-induced tangential velocity due to the local strength of the vortex sheet as explained by Kandil[*] (1981). If this term is not taken into account, errorous pressure coefficients are found. For panels with continuous vorticity, this term automatically exists in the induced velocity expression (Kandil et al., 1980). Kandil et al. (1977) have given a detailed description for a flat, rectangular element. Note that there is a typographical error in the definition sketch in that paper. Extension of this method to a general, quadrilateral vortex element has been implemented by Atta (1978) for

---

[*]Private discussion with Dr. Kandil (1981).

a control point located at the average of four corner points. These
two techniques for calculating the tangential velocity have been
summarized in Appendix C. In the present studies, a modified method
has been developed to calculate the tangential velocity due to the
local quadrilateral vortex element. The idea is based on the
equation due to Kandil et al.(1977) then extended to a quadrilateral
element. The reason for developing the new expression instead of
using the formula due to Atta (1978) is the lesser generality of the
latter expression. It is easy to find that the formula due to Atta
(1978) will give the same magnitude of tangential velocity for any
point on the element, which is not consistent with the mathematical
model. The modified method has the ability to account for the
deviation of the tangential velocity between different points. For
some special cases, as shown in the next section, the modified
method gives solutions which are identical to those obtained using
the expression due to Atta (1978). The comparison of these two
schemes for either axisymmetric flow or inclined flow will also be
shown in the next section.

For a typical planar quadrilateral vortex element with two
parallel sides, having the other two sides of equal length, as shown
in Sketch 3.2, the tangential velocity of a point located on the
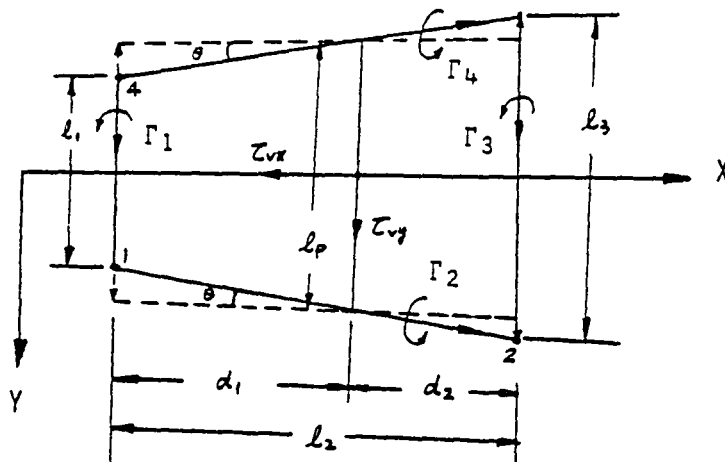center line is given as follows:

$$\tau_{vx} = \frac{1}{4\pi} \frac{1}{2\ell_2^2} [\Gamma'_1 \frac{\ell_1}{\ell_p} d_2 + \Gamma'_3 \frac{\ell_3}{\ell_p} d_1]$$

$$\tau_{vy} = \frac{1}{4\pi} \frac{1}{2\ell_p^2} [\Gamma_4 \cos\theta \frac{\ell_p}{2} + \Gamma_2 \cos\theta \frac{\ell_p}{2}] \qquad (3.20)$$

56

where $\quad \Gamma'_1 = \Gamma_1 + \Gamma_2 \sin\theta \dfrac{d_1}{\ell_2} \dfrac{d_1 \tan\theta}{\ell_1} - \Gamma_4 \sin\theta \dfrac{d_1}{\ell_2} \dfrac{d_1 \tan\theta}{\ell_1}$

$$\Gamma'_3 = \Gamma_3 + \Gamma_2 \sin\theta \dfrac{d_2}{\ell_2} \dfrac{d_2 \tan\theta}{\ell_3} - \Gamma_4 \sin\theta \dfrac{d_2}{\ell_2} \dfrac{d_2 \tan\theta}{\ell_3}$$

Sketch 3.2   Nomenclature of calculating the induced
             tangential velocity

These expressions have been developed from those of Kandil et al.
(1977) (summarized in Appendix C), and are similar to those of
Kandil et al. (1982). Modifications have been made to account for
the nonparallel orientations of Γ_2 and Γ_4, as well as to account for
the unequal lengths of filaments Γ_1 and Γ_3. The ratios ℓ_1/ℓ_p and
ℓ_3/ℓ_p in the τ_{vx} expression are to account for these unequal fila-
ment lengths. The filaments Γ_2 and Γ_4 have been resolved into com-
ponents along the x and y axes, and their x components used in
computing τ_{vy}. The signed y components of Γ_2 and Γ_4 have been used
to replace Γ_1 and Γ_3 by Γ'_1 and Γ'_3 as given above. Note that
these Γ_2, Γ_4 y components have been lumped with Γ_1 and Γ_3 using
linear interpolation, to allow movement of the control point away
from the panel center.

57

In case the field point is not located on the body surface, but is very close to the vortex segment, there is no tangential velocity component in the total velocity expression. However, the induced velocity due to the vortex segment must be modified by a viscous core relation in the form of an exponential multiplier, which causes the induced velocity to approach zero as the vortex is approached. The reason for this is simply because the law of Biot and Savart which is based on an inviscid flow, is singular. However, no artificial viscosity coefficient has been added in the present technique. An accurate accounting of the viscous effects must be obtained from boundary layer solutions, which is beyond the scope of the present study. Instead the velocity and pressure coefficients only at points on the body surface or at far field points have been obtained in the present work.

3.3 Accuracy of Method

Since the surface panel method has been developed for solving the potential flow past an arbitrary body, therefore, the technique of using the vortex ring element as an option to solve for the problem of axial flow past an axisymmetric body of revolution has not been considered here. Note that a very accurate C_p distribution could be obtained using this technique by employing a large number of ring elements. The test configurations investigated in the present study still remain in the axisymmetric body category. However, the flexibility for modelling a realistic fuselage (symmetric with the y=0 plane) has been considered in the computer program. Because of the assumed symmetric property, only one half

58

of the control points on the body surface are stored, but the influence coefficients of the induced velocity at these points are evaluated in the usual way. For each one of these control points, the influence coefficient due to the image of the stored element is evaluated by simply reflecting the coordinates of the corners of this element. The contributions are then added to those of the stored element. This reduces the number of unknowns by one half.

In studying the performance of the method for the test cases discussed below, a serious problem of the need for a large number of elements to adequately represent the given body has been found to exist. This situation is undesirable in terms of cost. However, the reliability of the present scheme may be recognized by studying the solutions presented below.

In this chapter, as in Chapter 2, the test geometry which has been considered and compared with the corresponding exact solution is a SR=5 ellipsoid. The tangential velocity jump has been calculated by the three different methods listed above: Kandil et al. (1977), Atta (1978), and the modified method, equation (3.20), and results have been displayed and discussed in sequence.

3.3.1 Axisymmetric Flow

For calculation of the axisymmetric flow past an ellipsoid of SR=5, a panelling scheme using cosine axial distribution of panels has been applied, to improve the solution accuracy. This is consistent with the criteria mentioned in section 3.2.1, where it was indicated that the best results would be obtained if the vortex panel elements were chosen to be of aspect ratio of nearly unity. Of course, the cosine spacing axial distribution is not the only way

to represent the body. The optimal panelling technique is expected to vary as the body geometry is varied. Figure 13 shows that the C_p distribution for the SR=5, ellipsoid along a meridian line obtained by using 8*30 panels (8 panels in the θ direction by 30 panels axially), with a cosine spacing axial distribution, is much more accurate than that obtained using the same number of panels but with equal spacing in the axial direction.

In order to discover the differences among the three tangential velocity calculation methods, Table 6 has been prepared. The test runs have all been based on the same panelling scheme as above of 8*30 panels, with a cosine axial distribution, and the control points have been located at the average of the four corner coordinates of each panel. In fact, location of the control points at the average of the four corner points is not recommended in general calculations. Another comparison, based on the recommended control point location of the centroid of area of each panel, will be given below. Note that the pressure distribution obtained by using the method of Atta (1978) is exactly the same as that which is obtained by using the modified method (equation 3.20), provided that the control points are selected to be the average of the four corner coordinates of the panels. Atta's application of Kandil's method and the present modified method both work better than Kandil's original formulation does, for the non-rectangular elements utilized in this test case. Especially at the nose and tail region, where the element is less rectangular, the solution accuracy has been improved by accounting for the length effect and orientation of the vortex segments. The same conclusion is reached

60

in the second comparison, as shown in Table 7, where the control points were selected to be the centroid of area of each panel. Another way to improve the solution accuracy, by moving the control points of all triangular elements from the centroid of area to the 3/4 chord length away from the apex of the element, was attempted, listed as "Scheme 2" in Table 7. No significant improvement was achieved through this effort. Numerically, Atta's method appears to be slightly superior to the modified method. However, the observed differences between these two methods are judged to be negligible. Therefore, the modified method (equation 3.20) is recommended in future applications, since it correctly accounts for variation in control point location. It is also noted that the solutions obtained from the vortex lattice surface panel method are less accurate than those obtained from the axial singularity method. The reason is because the present calculation doesn't involve enough panels to adequately represent the body, and due to the poor accuracy obtainable with the discrete vortex singularities used to represent the continuous surface vortex sheets.

3.3.2 Inclined Flow at 20° Angle of Attack

Procedures identical to those used in the axisymmetric flow analysis above were repeated for the flow at a 20° angle of attack for the SR=5 ellipsoidal body. Table 8 shows the C_p distribution along two meridian lines, one located 7.5° away from top meridian line, with the other located 82.5° away from top meridian line, using 12*20 panels, cosine spacing axial panel distribution, and with the control points located at the average of the four corner coordinates of each panel. Numerical solutions obtained from both

61

Atta's and the modified method match the exact solution fairly well along the $\theta = 82.5^0$ meridian line, but are less accurate near the nose along the $\theta = 7.5^0$ meridian line. This may be explained in that the assumption of a linearly distributed vortex sheet strength used in the tangential velocity calculation is no longer adequate at the leeward side of the body near the nose when a large angle of attack is imposed.

Tables 9 and 10 display the C_p solutions obtained by moving the control points to the centroid of area of the panels and keeping the rest of the conditions the same as for Table 8. Through comparison of these results, it is found that taking the centroid of the panel area as the control point location yields a more accurate C_p solution. This reinforces Asfar et al.'s assertion about choosing the minimum induced velocity point as the control point location to obtain the best solution.

Figure 14 displays the C_p distribution along four meridian lines in the first quadrant, compared with the exact solution, for the SR=5, $\alpha = 20^0$ ellipsoidal body, using 12*20 panels, cosine spacing axial distribution, and the modified tangential velocity calculation method. Figure 15 displays the C_p distribution along six circumferential lines at different x/L locations and compares it with the exact solution for the same body using the same method. In general, the calculated solution matches the exact solution well, except at the leeward side of the body near the nose. Note that the θ coordinate used in the surface singularity program is shifted 180°_compared to that used in Chapter 2 for the axial singularity method.

62

CHAPTER 4

RESULTS AND COMPARISONS FOR GENERAL
AXISYMMETRIC CONFIGURATIONS

4.1 Introduction

To further investigate the accuracy and the capability of the
two computer programs described in Chapters 2 and 3, six additional
configurations have been investigated in a series of numerical
experiments. The main area of concern for the axial singularity pro-
gram has been to investigate the feasability of obtaining
approximate C_p distributions for a series of axisymmetric bodies
having discontinuous surface curvature, such as a cylindrical body
with an ellipsoidal nose and tail. Previously, Zedan and Dalton
(1980) have claimed that the axial singularity method cannot
accurately model bodies with either discontinuous surface slope or
surface curvature. It has been found in the present work that the
axial singularity method appears to have the capability of modelling
the second type of configuration having discontinuous changes in
surface curvature, provided a careful numerical scheme is applied,
as described below. Solutions for these types of configurations
using the axial singularity method have been obtained and compared
in this chapter with those obtained from the surface source program
of Hess and Smith (1967) and available experimental data. A brief
discussion about the panelling techniques has also been given
separately for each test case. The vortex lattice surface

singularity program described in Chapter 3 has been run for each configuration, and compared with all other theoretical and experimental results. An explanation has been given in the discussion of the last configuration (30° cone-cylinder), to clear up the faulty conclusion which appeared in Asfar et al. (1979), where it was claimed that the surface vortex lattice method was superior to the surface source method. Generally, the comparisons shown in this chapter demonstrate that good C_p distributions can be obtained from either the axial singularity or the vortex lattice surface methods. Despite the fact that the surface velocity is extremely sensitive to the details of the surface geometry, the above two methods obviously have the capability to account for a wide range of surface geometry accurately. This means that the solution accuracy is largely dependent upon the input surface geometry and panelling, but not the methods themselves. This chapter is intended to serve as an indication of the capabilities of the two methods, and is therefore not intended to be all-inclusive. In particular, no results have been obtained for general three-dimensional bodies. This is largely due to a lack of effort to develop or utilize a general three dimensional geometry input routine such as GEMPAK (see Stack, 1982).

4.2 Test Configurations

4.2.1 Modified Ellipsoid with Zero Curvature at the Maximum Thickness

This body is similar to a configuration which was described by

Hess and Smith (1967) as a two-dimensional body of SR=5, whose profile curve was given by

$$y = \pm \, 0.2\sqrt{1 - x^{3/2}} \qquad\qquad (4.1)$$

Despite the strong similarity in the shapes of the same slenderness ratio 5 ellipsoidal body of revolution and this configuration, their surface pressure distributions are, of course, quite different. That for the ellipsoidal body is very flat and entirely concave down, while that for the modified ellipsoidal body obtained from equation (4.1) by replacing y by r, has a sharp peak at the shoulder and a wide region where it is concave up.

The reason that this configuration has been chosen as a test case in the present study is that the geometry contains an infinite radius of curvature at the shoulder, and as a result, it can be viewed as a transitional model from the ellipsoid to a cylindrical body witn an ellipsoidal nose and tail.

Figure 16 (a) shows the source strength distribution along the body axis obtained by using the constant and linearly varying axial singularity schemes described in Chapter 2. Both cases used 20 cosine type discrete panels to represent the given body. The difference in the strength distribution for the linear source singularity method between the ellipsoid and this modified ellipsoid configuration is that the former one (Figure 2) has a continuous strength at the shoulder and the latter one has a jump in strength there. Apparently, the zero curvature at the shoulder is responsible for this jump. One must account for this discontinuity

in source strength when modeling those classes of bodies with discontinuous curvature using the linear source singularity. In building up the influence coefficient matrix, the continuity equation at the shoulder must be replaced by a constraint equation which will allow a strength jump but having zero net strength there. Therefore, the anti-symmetric property in axial singularity strength distribution is still maintained without any change due to the effect of discontinuous curvature at the shoulder. Figure 16 (b) shows the C_p distribution along a meridian line at $\alpha = 0^0$. Both constant and linearly varying source appear to give the same level of solution accuracy. The C_p curve also has a cusped peak at the shoulder which is the characteristic C_p property for this geometry.

In order to confirm the accuracy of the solution obtained from the axial singularity program, the same configuration has been analyzed using the vortex lattice surface singularity program. The panelling scheme undertaken herein was an 8*30 cosine type axial distribution. Figure 17 displays the comparison of C_p distributions between the two different methods. The equivalence of the two solutions shown does provide evidence that the two solutions are each correct. No experimental data for this type of body is known.

4.2.2 Ogival Body of Revolution

The surface of this configuration is composed by rotating a finite circular arc around the body axis. Such geometries have a pointed nose and tail. The body surface is governed by an analytic function where the slope and curvature are continuous. At the region very close to the pointed nose and tail, potential flow theory will not predict an accurate C_p solution. However, it is

66

believed that a satisfactory C_p distribution can be obtained by using the present two programs over most of the body surface.

Figure 18 (a), (b) display the source strength distributions along the body axis obtained using constant and linearly varying axial singularity schemes for SR=4 ogival body of revolution. The panelling technique undertaken for both computer runs is 20 discrete cosine spaced panels, without inset, to represent the given body. The selection of zero inset distance has been made due to the fact that the radius of curvature of a pointed nose is zero. This is consistent with earlier recommendations of Zedan and Dalton (1980). Note that the source strength at the nose and tail is found to be zero, and the strength distribution is strictly anti-symmetric. The appearance of these two properties is helpful in judging the solution quality. Figure 18 (c) displays the C_p distribution along a meridian line. The constant and linearly varying source schemes give nearly identical C_p values for the entire region except at the nose and tail where the pressure has a sudden drop if the former scheme is used. The explanation for this incorrect pressure drop is that the constant strength axial singularity distribution is inadequate to describe flow at the nose region of an ogival body. However, the solution accuracies away from the nose and tail are strongly confirmed in this comparison.

As was done in analyzing the first configuration, Figure 19 has been prepared to show the comparison of C_p solutions between the axial singularity and the vortex lattice surface panel programs. Again, a panelling scheme using 8*30, cosine axial spaced panels has been applied to model the present configuration in the vortex

67

lattice surface program. The discrepancy appearing in this figure is believed to be due to error in the surface vortex lattice method. An equal spacing panelling scheme reduces the numerical error (see Figure 19), but perhaps addition of some source singularities near the stagnation points may be necessary to obtain more accurate results.

4.2.3 Cylindrical Body with Modified Ellipsoidal Nose

This configuration consists of a cylindrical middle section with the radius equal to the semi-minor axis length of the modified ellipsoidal nose and tail. Therefore, the surface slope is continuous everywhere and surface curvature goes smoothly to zero on the middle cylindrical surface. This geometry is a special example of a smooth body of revolution. Slender body theory can well predict the C_p distribution in the middle part of such bodies, but not for the nose and tail. The present study does not impose the slender body assumptions in formulation. As for the first configuration, a strength jump at the junction where the radius of curvature goes to infinity will be allowed when the linearly varying source distribution is used.

Figure 20 (a), (b) show the axial source strength distributions along the body axis obtained using constant and linearly varying source distributions. Both cases use 10 panels for the nose and tail, and one panel for the cylindrical part, where the cross sectional area is constant. In the case of using linear type singularity distributions to model the given body, the two source strength continuity equations at the junctions have been replaced by two extra no-penetration boundary equations. In other words, two

68

extra control points have been located on the body surface.
Numerical experiments show that the C_p distribution in this
configuration is not sensitive to the location of these two extra
control points. However, some adjustment of control point location
is needed for similar bodies having a long cylindrical middle
section. More discussion about this adjustment will be given in
discussion of the fifth configuration.

The C_p distributions from these two test runs are nearly
identical, as shown in Figure 20 (c). Although there is no
experimental data available, this configuration has been modeled
using the vortex lattice surface panel program. Panelling used is
8*30 panels with equal axial spacing. Through the consistency of
the C_p solutions for the above three theoretical cases, one may
conclude that both the axial singularity method and the surface
vortex lattice method are adequate for this configuration.

4.2.4   Cylindrical Body with Ogival Nose

This configuration was obtained by replacing the SR=5 modified
ellipsoidal nose and tail with a SR=4 ogival nose and tail. The
detailed geometry is shown in Figure 21. A similar body with a boat
tail, as shown in the same figure, was utilized in a wind tunnel
experimental test by Fox (1971) to obtain C_p distributions at a Mach
number equal to 0.403. Over the front half of the body, the
pressure distribution will not be strongly influenced by the
different tail shapes. Therefore, the same symmetrical
computational model has been used for both the axial singularity
program and the vortex lattice surface panel program. Good
agreement with the experimental C_p data is observed in Figure 21 for

69

all methods. The solution obtained from the axial singularity program matches the experimental data even better than that from the vortex lattice surface panel program. Of course, the small number of vortex lattice panels used in modelling this configuration is likely responsible for this discrepancy.

4.2.5 Cylindrical Body with Ellipsoidal Nose

This configuration is composed of a SR=2 blunt nose and a long cylindrical body. The available experimental C_p data were obtained by Campbell and Lewis (1955). The panelling technique used in the previous two configurations has been found to be inadequate for the present configuration. The reasons are, first, the nose is too blunt, and second, the length of cylinder section is too long. It has been found that the C_p solution for this configuration is very sensitive to the panelling and control point location, a result which was not seen for the previous two cases. In general, it has been found that the constant source singularity scheme cannot handle geometries similar to the present configuration. Based on accumulated experience, a new panelling scheme has been discovered and found to be adequate to yield a set of reasonable C_p values, for the linear source scheme. Again, the discontinuous strength at the juncture is allowed. Also, three panels are used to represent the cylindrical section. Since a sudden localized sink distribution was expected to be necessary to accurately model the flow around the shoulder over the junction between the nose and cylinder, the additional two panels on the cylinder were chosen to be relatively small. Because the two source strength continuity equations at the junctions do not exist, two extra control points were needed to

70

perform the calculations. Numerical experiments have shown that these two extra control points, combined with the original three control points, corresponding to the three panels in the cylindrical section, should be equally distributed on the cylinder surface to yield the best results. The detailed control point locations on the cylindrical section have been shown along with the resulting C_p solution in Figure 22. It has been found that the size of the two small panels is not critical, between one percent and four percent of the cylinder length, in obtaining the same accuracy of Cp distribution, even though the singularity strength distribution is changed somewhat. Figure 22 shows the Cp distribution along a meridian line when the flow is at zero angle of attack. Comparing the solution obtained from the axial singularity program to experimental data, a good agreement is noted over the front portions of the computational model. The small discrepancies on the cylindrical surface are mainly due to differences in geometry between the wind tunnel model and the computational model. This assertion has been verified by calculating the Cp values for a configuration having a longer cylindrical middle section, with the same size nose and tail. Pressures for such a geometry were closer to the data. Figure 22 also shows the Cp solution obtained from the vortex lattice surface panel program. The panel scheme used herein is 10*32 panels with a cosine type axial distribution. The solution accuracy for the vortex lattice surface panel method is seen to be not as good as that of the axial singularity method.

Results are presented in Figure 23 for the same configuration as in Figure 22, but at an angle of attack of $\alpha = 6.08^0$, along the

top meridian line of the body. Experimental results have been shown as a solid curve because no data values were given by Campbell and Lewis (1955) when $\alpha \neq 0^0$. Panelling, inset and control point location for the source flow are the same as was used in Figure 22 at $\alpha = 0^0$. However, the linear crossflow doublet calculations have been made assuming continuous strengths at the junctions between nose or tail and cylinder. Also, control point location on the cylinder has been chosen to be of the cosine type. Agreement between experiment and the axial singularity method is not as good as was observed for $\alpha = 0^0$; the reasons for the observed discrepancies are not known. Also shown are results at $\theta = 9^0$ for the vortex lattice surface method, using 10*30 panels; these results are less accurate than the axial singularity results.

4.2.6   30° Cone Cylinder

This configuration first was studied by Johnson (1963). He compared pressure distributions computed by the surface source panel method (Douglas Neumann Program) of Hess and Smith (1967) with experimental data which he obtained at zero angle of attack and at plus and minus 20° angle of attack. The cylindrical after-body of the wind tunnel model had a length equal to 2.9 times its radius. The geometrical model utilized in the surface source panel program was semi-infinite. This difference between the geometries of the experiment and theory led to discrepancies between calculated and experimental pressures on the after portions of the cylindrical body, but its effect was found to be negligible over the nose regions. More recently, the same configuration has been studied by Asfar et al. (1979) to test the solution accuracy for their vortex

72

lattice surface panel method. The computational geometry in their
work was exactly the same as the wind tunnel model of Johnson.
Therefore, the pressure distributions obtained in Asfar's work
matched the experimental data much better than those obtained from
the surface source panel program of Hess and Smith over the after
portions of the cylindrical body. Asfar was apparently unaware of
these differences in geometry, and mistakenly concluded that the
surface vortex lattice method was superior to the surface source
method. In order to show that this conclusion is incorrect, two
test runs have been prepared to illustrate the effect of after-body
length of the 30° cone-cylinder geometry. As shown in Figure 24,
the Cp distribution of the first geometry, having a cylindrical
after-body with a length equal to 2.9 times its radius, matches the
experimental data well. When the cylindircal after-body length was
extended to be 8.5 times the cylinder radius, then the Cp
distribution of this second geometry matches the solution obtained
from the surface source panel program. Note that all four pressure
curves agree well along the cone surface. In the after-region, the
predicted pressure values could be strongly influenced by the sharp
corner.

Figures 25 through 27 compare the calculated and the experi-
mental pressure distributions along three different meridian
lines ($\theta = 45^0$, $\theta = 90^0$, $\theta = 135^0$) at 20° angle of attack for this
configuration. At this angle of attack, agreement is good over the
nose portion of the body for all cases, and less satisfactory over
the after-body. The biggest discrepancy occurs at the leeward side
of the after-body, as shown in Figure 25, where the flow is expected

to be separated for this angle of attack.

Figure 28 compares calculated and experimental circumferential pressure distributions at two axial locations on the pointed 30° cone-cylinder at 20° angle of attack. Again, the effect of separation on the leeward side of the cone can be seen, particularly for the after station. Panelling used for this configuration is 10*32 panels, equally distributed along the x axis. Of course, the solution may be improved by adequately refining the panels. It is worthwhile to note that no success was had in attempts to obtain the Cp distribution using the axial singularity program for this geometry.

CHAPTER 5

CONCLUSIONS

Two different types of singularity methods have been considered
in solving for the potential flow due to a uniform stream, either
axisymmetric or at an angle of attack, past a non-lifting body. The
theoretical formulations have been described in separate chapters of
this thesis. Two FORTRAN computer programs have been generated and
tested to implement these theoretical models. Solutions obtained
from these two programs for certain classes of axisymmetric bodies
have been compared with exact solutions or available experimental
data. Numerical experiments have shown that both methods give
accurate Cp distributions for general axisymmetric bodies of
revolution, except that the axial singularity method cannot handle
bodies with discontinuous surface slopes. For axisymmetric bodies
which are sufficiently smooth, the axial singularity method is more
accurate than the surface vortex lattice method. Some important
features about these two methods will be summarized below.

The axial singularity method is considered to be a method which
is quite inexpensive, since little computer memory is required, but
it has more restrictions on body geometry compared to surface
singularity approaches of solving for the potential flow past an
axisymmetric body. In the course of analyzing an aircraft
configuration, the axial singularity method will not be adequate for
modelling a general fuselage. However, at the preliminary design

stage to estimate the interactions between a fuselage of simple geometry and the non-planar wing, this method is far more applicable than any other numerical approach. By employing higher-order singularity distributions, great improvements in the solution accuracy and geometry flexibility have been found. Specifically, a higher-order axial singularity distribution model has been formulated for either axial or cross flow, where constant and linear orders in strength variation have been utilized to yield a numerical solution. It has been found that panel and control point location for the higher-order singularity method can be very important for obtaining a good quality solution. Inadequate choice of panelling for this technique will yield solutions which are incorrect, as was found, for example, using the continuous linearly varying source distribution applied to model the flow past a cylindrical body with either ogival or ellipsoidal noses. Judgement of the adequacy of the solution can be aided by visualizing the variation of source strength distribution along the body axis. For ellipsoidal bodies, a reliable and accurate panelling technique has been described, where the optimal Cp distribution for the axisymmetric flow past a general ellipsoid has been found by using cosine spaced, linearly varying source distributions with the suggested inset distance governed by equation (2.69). The solution accuracy so obtained has a root mean square error in pressure coefficient on the order of 10^{-5}. The same panelling and inset has been found to yield comparable solution accuracies for ellipsoids of slenderness ratios between 2 and 10 at angles of attack up to 30° degrees. Therefore, the inset distance plays a key role in obtaining the optimal Cp

solution for blunt nosed bodies. This optimal inset appears to depend most strongly upon the local radius of curvature of the body nose. A more limited effect of the size of the singularity element nearest the nose may also be noted. This discovery can be viewed as being contradictory to assertions made by Zedan and Dalton (1980), where it was recommended that 1% inset distance be used for all ellipsoidal body calculations. Another important feature in the present study has been the attempt to obtain solutions for axisymmetric bodies with discontinuous surface curvature using the axial singularity method. Despite the fact that some reasonably good Cp distributions have been obtained from such geometries by using a specialized singularity panel size variation consisting of cosine panel distributions on the nose and tail, plus two very small panels at the ends of the cylinder, no general panelling rule applicable to all configurations has been developed at the present time.

Accuracy of the vortex lattice surface panel method implemented in the present study has been investigated using various axisymmetric configurations. The Cp distributions have been compared with exact solutions, experimental data, and results of the surface singularity theory. It has been found that the solution accuracy is largely dependent upon the panel aspect ratio and the control point location. Best results will be obtained by chosing the panels to have aspect ratios near unity and taking the minimum induced velocity point inside the panel to be the control point. The panel centroid has been found to be an acceptable control point location. The local tangential velocity calculation method

devleoped in previous works by Kandil et al. (1977); Atta (1978); and Asfar et al. (1979), has been extended as documented in Chapter 3. This modified tangential velocity calculation method allows both use of non-rectangular panels and movement of the control point location away from the panel center. Comparisons of solutions obtained using these different formulations have been displayed. It is also found that the present modified equation yields the same accuracy Cp distribution as compared to Atta's method, but allows more flexibility in control point location. None of these methods yield satisfactory Cp distributions at the leeward side of an ellipsoidal body nose and tail when the flow is at a moderate angle of attack. Next, in Asfar et al. (1979), it has been asserted that the vortex lattice surface panel method is more accurate than the surface source panel method, since the numerical solutions of the vortex lattice method matched experimental data for 30° cone-cylinder much better than for the source method. In the present work, it has been proven that this conclusion was incorrect, being due to differences in geometries used in the two methods. Error sensitivities of this method to locating the control points off the actual body surface, in the plane of the panel, have not been investigated in the present work.

Since the vortex lattice surface panel method has the ability to model an arbitrary body, but required a great deal of computational effort, a simplified vortex lattice model based on the technique used by Mason et al. (1977), using slender body transformation of the actual body slope to a bounding rectangular box has been investigated as a part of the present research. A

brief description of this study has been given by Shu and Kuhlman (1981). Due to difficulty in obtaining an adequate expression for the local tangential velocity on the rectangular box, this approach has been found to not be fruitful.

Finally, as previously discussed, the main purpose of the present study has been to develop theoretical methods which will allow the inclusion of fuselage effects into a pair of existing subcritical wing design programs (Kuhlman and Shu, 1981; Kuhlman, 1983). Both fuselage programs are now ready to be modified for addition into the above mentioned design computer programs. Future plans are to accomplish this task.

References

1. Asfar, K. R., Mook, D. T., and Nayfeh, A. H., "Application of the Vortex-Lattice Technique for Arbitrary Bodies," _Journal of Aircraft_, Vol. 16, No. 7, July 1979, pp. 421-424.

2. Atta, E. H., "Nonlinear Steady and Unsteady Aerodynamics of Wings and Wing-Body-Combinations," Ph.D. Dissertation, Dept. of Engineering Sciences and Mechanics, V.P.I. & S.U., Blacksburg, VA, May 1978, Avail. Univ. Microfilms as 7822718.

3. Bogen, R., Golden, J., Genesereth, M., and Doohovskoy, A., "MACSYMA Reference Manual, Version 8," The Math Lab Group, Project MAC, Massachusetts Institute of Technology, Nov. 1975.

4. Bristow, D. R., "A New Surface Singularity Method for Multi-element Airfoil Analysis and Design," AIAA Paper No. 76-20, Jan. 1976.

5. Campbell, I. J. and Lewis R. G., "Pressure Distribution: Axially Symmetric Bodies in Oblique Flow," Aeronautical Research Council C. P. No. 213, 1955.

6. Cebeci, T., Kattab, A. H., and Stewartson, K., "On Nose Separation," _Journal of Fluid Mechanics_, Vol. 97, Part 3, 1980, pp. 435-454.

7. Crigler, J. L., "Comparison of Calculated and Experimental Load Distributions on Thin Wings at High Subsonic and Sonic Speeds," NACA TN 3941, 1957.

8. Dalton, C. and Zedan, M. F., "Design of Low Drag Axisymmetric Shapes by the Inverse Method," Published in ASME Book Number G00147, 1979, and presented in ASME/AIAA/SAE Joint Symposium on Aerodynamics of Transportation, Niagara Falls, N. Y., June 18-20, 1979.

9. David, A. L. and Geppson, R. W., "Solving 3-D Potential Flow Problems by Means of an Inverse Formulation and Finite Differences," NTIS CSCL 20/4, N73-26302 (Microfishe), 1973.

10. Faulkner, S., Hess, J. L., and Giesing, J. P., "Comparison of Experimental Pressure Distributions with Those Calculated by the Douglas Aircraft Company," Report No. LB31831, McDonnel-Douglas Co., Dec. 1964.

11. Fox, C. H., "Experimental Surface Pressure Distribution for a Family of Axisymmetric Bodies at Subsonic Speeds," NASA TMX-2439, 1971.

12. Gradshteyn, I. S. and Ryzhik, I. M., _Table of Integrals, Series, and Products,_ Academic Press, 1980, pp. 67-69.

13. Hess, J. L. and Smith, A. M. O., "Calculation of the Nonlifting Potential Flow About Arbitrary Three Dimensional Bodies." Report No. E. S. 40622, McDonnel-Douglas Co., 1962.

14. Hess, J. L. and Smith, A. M. O., "Calculation of Potential Flow About Arbitrary Bodies," _Progress in Aeronautical Sciences,_ Vol. 8, Pergamon Press, 1967.

15. Johnson, W. E., "Experimental Investigation and Correlation with Theory of the Surface Pressure Distribution on Several Sharp and Blunted Cones for Incompressible Flow," M. Sc. Thesis, Dept. of Aero. and Astro., Univ. of Washington, 1963.

16. Kandil, O. A., Mook, D. T., and Nayfeh, A. H., "Nonlinear Prediction of the Aerodynamic Loads on Lifting Surface," AIAA Paper No. 74-503, Palo Alto, CA, June 1974.

17. Kandil, O. A., "Prediction of the Steady Aerodynamic Loads on Lifting Surfaces Having Sharp-Edge Separations," Ph.D. Dissertation, VPI & SU, Dec. 1974.

18. Kandil, O. A., Atta, E. H., and Nayfeh, A. H., "Three Dimensional Steady and Unsteady Asymmetric Flow Past Wings of Arbitrary Planforms," AGARD CP-227, Sept. 1977, pp. 2-1 to 2-19.

19. Kandil. O. A., Chu, L., and Yates, Jr., E. Carson, "A Hybrid Vortex Method for Lifting Surfaces with Free-Vortex Flows," AIAA Paper No. 80-0070, Jan. 1980.

20. Kandil, O. A., Chu, L. C., and Tureaud, T., "Steady and Unsteady Nonlinear Hybrid Vortex Method for Lifting Surfaces at Large Angles of Attack," AIAA Paper No. 82-0351, Orlando, Florida, Jan. 1982.

21. Karamcheti, K., _Principles of Ideal-Fluid Aerodynamics,_ Wiley, 1966, pp. 331-344.

22. Kuhlman, J. M., "Iterative Optimal Subcritical Aerodynamic Design Code Including Profile Drag," AIAA Paper No. 83-0012, presented at AIAA 21st Aerospace Sciences Meeting, Reno, Nevada, Jan. 10-13, 1983.

23. Kuhlman, J. M. and Shu, J. Y., "Computer Program Documentation for a Subcritical Wing Design Code Using Higher Order Far-Field Drag Minimization," NASA CR-3457, Sept. 1981.

24. Lamar, J. E., "Effects of Aeroelasticity on Static Aerodynamics Derivatives," in NASA SP-258, 1971, pp. 375-438.

25. Lamb, H., Hydrodynamics, Sixth Edition, Dover Publications, 1932, pp. 139-156.

26. Lan, C. E., "A Quasi-Vortex-Lattice Method in Thin Wing Theory," Journal of Aircraft, Vol. 11, No. 9, Sept. 1974, pp. 518-527.

27. Mason, W. H., Balhaus, W. F., MacKenzie, C., Frick, J., and Stern, M., "An Automated Procedure for Computing the Three-Dimensional Transonic Flow over Wing-Body Combinations, Including Viscous Effects. Vol. I. Description of Analysis Methods and Applications," Report AFFDL-TR-77-122, Vol. I, Feb. 1977. (Available from DTIC as AD-A055899.)

28. Oberkampf, W. L. and Watson, L. E., "Incompressible Potential Flow Solutions for Arbitrary Bodies of Revolution," AIAA Journal Vol. 12, 1974, pp. 409-411.

29. Schlichting, H., and Truckenbrodt, E., Aerodynamics of the Airplane, McGraw-Hill and Hemisphere, 1979.

30. Shu, J. Y. and Kuhlman, J. M., "A Simplified Vortex Lattice Model for Potential Flow Past a Fuselage," Presented at 59th Annual Meeting of the Virginia Academy of Science, Norfolk, VA, May 12-15, 1981, and abstract published in the Virginia Journal of Science, Vol. 32, No. 3, 1981, pp. 71.

31. Stack, S. H., "Computer-Aided Design System Geared Toward Conceptual Design in a Research Environment," Journal of Aircraft, Vol. 19, No. 2, Feb. 1982, pp. 176-182.

32. Streett, C. L., "Viscous-Inviscid Interaction for Transonic Wing-Body Configurations Including Wake Effects," AIAA Paper 81-1266, Presented at AIAA 14th Fluid and Plasma Dynamics Conference, Palo Alto, CA, June 22-24, 1981.

33. Von Karman, T., "Calculation of Pressure Distribution on Airship Hulls," NACA TM 574, 1930.

34. Wang, K. C., "Three-Dimensional Boundary Layer Near the Plane of Symmetry of a Spheroid at Incidence," Journal of Fluid Mechanics, Vol. 43, Part 1, 1970, pp. 187-209.

35. Zedan, M. F. and Dalton, C., "Potential Flow Around Axisymmetric Bodies: Direct and Inverse Problems," AIAA Journal, Vol. 16, March 1978, pp. 242-250.

36. Zedan, M. F. and Dalton, C., "Higher-Order Axial Singularity Distributions for Potential Flow About Bodies of Revolution," Computer Methods in Applied Mechanics and Engineering, Vol. 21, North-Holland Publishing Co., 1980, pp. 295-314.

APPENDIXES

APPENDIX A

MACSYMA INTEGRAL EXPRESSIONS

Integral expressions, utilized in the axial singularity method of Chapter 2, obtained by using the MACSYMA symbolic manipulation language (Bogen et al., 1975) are given below:

(1)
$$H_1 = \int \frac{d\xi}{[(x_i-\xi)^2 + z_i^2]^{3/2}} = \frac{(x_i-\xi)(z_i^2 + x_i^2-2x_i\xi + \xi^2)^{1/2}}{z_i^4 + (x_i^2-2x_i\xi + \xi^2)z_i^2} \tag{A.1}$$

(2)
$$H_2 = \int \frac{\xi d\xi}{[(x_i-\xi)^2 + z_i^2)^{3/2}} = \frac{z_i^2 + x_i^2-x_i\xi}{z_i^2(z_i^2 + x_i^2 -2x_i\xi + \xi^2)^{1/2}} \tag{A.2}$$

(3)
$$H_3 = \int \frac{\xi 2 d\xi}{[(x_i-\xi)^2 + z_i^2]^{3/2}}$$

$$= \frac{-[z_i^2(z_i^2+x_i^2-2x_i\xi+\xi^2)^{1/2}\sinh^{-1}(\frac{x_i-\xi}{|z_i|}) + (x_i+\xi)z_i^2+x_i^3-x_i^2\xi]}{z_i^2(z_i^2 + x_i^2 - 2x_i\xi+\xi^2)^{1/2}} \tag{A.3}$$

(4)
$$P_1 = \int \frac{d\xi}{[(x_i-\xi)^2 + z_i^2]^{5/2}}$$

$$= \frac{(x_i-\xi+2)z_i^2+2x_i^2-4x_i\xi+2\xi^2}{(z_i^2+x_i^2-2x_i\xi+\xi^2)^{1/2}[\textrm{\j}z_i^6+(3x_i^2-6x_i\xi+3\xi^2)z_i^4]} \tag{A.4}$$

(5)　$P_2 = \int \dfrac{\xi d\xi}{[(x_i-\xi)^2 + z_i^2]^{5/2}}$

$$= \dfrac{z_i^4+(3x_i^2-3x_i\xi)z_i^2+2x_i^4-6x_i^3\xi+6x_i^2\xi^2-2x_i\xi^3}{(z_i^2+x_i^2-2x_i\xi+\xi^2)^{1/2}[3z_i^6+(3x_i^2-6x_i\xi+3\xi^2)z_i^4]} \qquad (A.5)$$

(6)　$P_3 = \int \dfrac{\xi^2 d\xi}{[(x_i-\xi)^2 + z_i^2]^{5/2}}$

$$= \dfrac{-[2x_iz_i^4+(4x_i^3-6x_i^2\xi+3x_i\xi^2-\xi^3)z_i^2+2x_i^5-6x_i^4\xi+6x_i^2\xi^2-2x_i^2\xi^3]}{(z_i^2+x_i^2-2x_i\xi+\xi^2)^{1/2}[3z_i^6+(3x_i^2-6x_i\xi+3\xi^2)z_i^4]}$$
$$(A.6)$$

(7)　$P_4 = \int \dfrac{\xi^3 d\xi}{[(x_i-\xi)^2 + z_i^2]^{5/2}}$

$$= \dfrac{-[2z_i^6 + (6x_i^2-6x_i\xi + 3\xi^2)z_i^4+ (6x_i^4-12x_i^3\xi + 9x_i^2\xi^2-3x_i\xi^3)z_i^2 +}{(z_i^2 + x_i^2-2x_i\xi + \xi^2)^{1/2}[3z_i^6 +}$$

$$\dfrac{2x_i^6 - 6x_i^5\xi + 6x_i^4\xi^2 - 2x_i^3\xi^3]}{(3x_i^2 - 6x_i\xi + 3\xi^2)z_i^4]} \qquad (A.7)$$

APPENDIX B

SELECTION OF CONTROL POINT LOCATION

FOR VORTEX LATTICE METHOD

According to Asfar et al. (1979), the most accurate Cp solutions will be obtained when the control points have been located so that the self-induced velocity due to the closed loop vortex filament at its own control point is a minimum. Searching for the correct location of this point, of course, is very tedious and requires a lot of calculations. In the present study of axisymmetric bodies, all panels have been chosen to be planar quadrilaterals with two parallel sides and having the other two sides of equal length, except at the nose and tail where panels have been chosen to be of equilateral triangular shape. Through a series of numerical experiments, as shown below, it has been found that choosing the control point location to be the centroid of area of each panel can be used to replace the original technique without too much difference in the solution accuracy. The following two sections are designed to show, first, how to compute the coordinates of the centroid of area of a typical panel, and second, the difference in location of control points calculated for these two methods.

B.1 Determine the Coordinates of the Centroid of Area

Consider a typical panel as described above, located in local cartesian coordinates as shown in Sketch B.1.
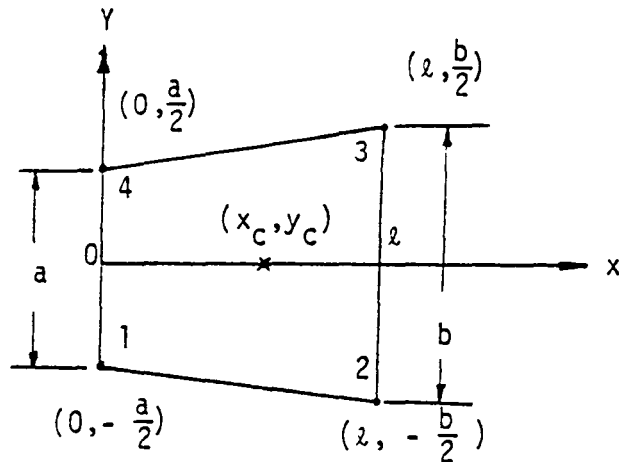
Sketch B.1 Nomenclature of a typical panel in
local cartesian coordinates

The local coordinates of the centroid of area are given as

$$x_c = (1 - \frac{2a+b}{3(a+b)}) \, \ell \qquad (B.1)$$

$$y_c = 0 \qquad (B.2)$$

The global coordinates can be obtained by performing a simple

transformation.

B.2 Difference in Coordinates between the Minimum Self-Induced
Velocity Point and the Centroid of Area

The following brief table, obtained from numerical experiments,

shows that the centroid of area may be used in place of the optimal

control point location, because small differences exist in control

point location and induced velocity magnitude.

Table B.1 Comparisons of the minimum self-induced
velocity point and the centroid of area

| Test No. | Panel Geometry | | | Centroid of Area | | Minimum Induced Velocity | | Differences | |
	a	b	ℓ	x_c	y_c	x_m	y_m	$\dfrac{x_m-x_c \%}{L}$	$\dfrac{W_c-W_m \%}{W_m}$
1	2.	4.	5.	2.78	0	2.87	0	1.8	0.6
2	0.	4.	6.	4.	0	4.3	0	6.0	1.2
3	0.	1.364	2.	1.34	0	1.45	0	5.5	1.2
4	1.364	1.819	2.	1.048	0	1.07	0	1.1	0.2
5	2.082	2.229	2.	1.011	0	1.04	0	1.45	0.16
6	2.229	2.274	2.	1.003	0	1.04	0	1.83	0.3

,

APPENDIX C

CALCULATION OF LOCAL TANGENTIAL VELOCITY

FOR VORTEX LATTICE METHOD

When the field piont is on the body surface, one has to account for the induced tangential velocity due to the local strength of the vortex sheet. The parameters involved in calculating the components of the induced tangential velocity in the x and y directions at a point P for a rectangular vortex element on the X-Y plane are shown in Sketch C.1. With linear interpolation, Kandil et al. (1977) gave the expressions for the components of tangential velocity as follows:
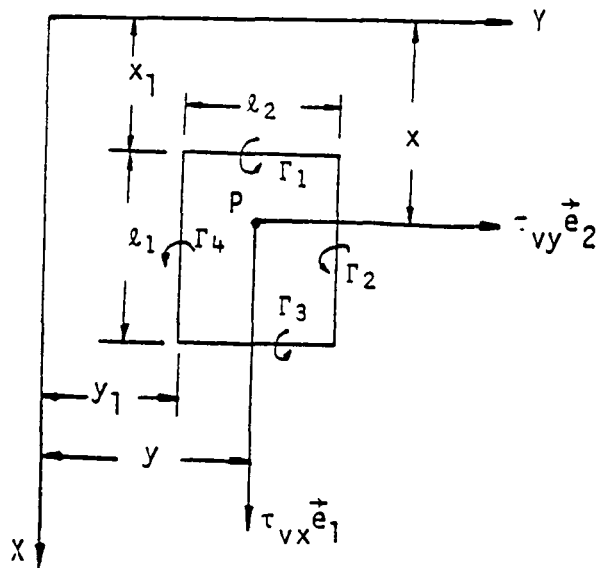
Sketch C.1 Nomenclature of calculating the induced tangential velocity

$$\vec{\tau}_{vx} = \frac{1}{2\ell_1^2} [\Gamma_1(x_1+\ell_1-x) + \Gamma_3(x-x_1)]\vec{e}_1 \qquad\qquad (C.1)$$

$$\vec{\tau}_{vy} = \frac{-1}{2\ell_2^2} [\Gamma_4(y_1+\ell_2-y) + \Gamma_2(y-y_1)]\vec{e}_2 \qquad\qquad (C.2)$$

Extension of these two equations to a general, quadrilateral vortex element has been given by Atta (1978) as follows:

$$\Delta\vec{V} = (\frac{\Gamma_1\vec{\ell}_1 + \Gamma_2\vec{\ell}_2 + \Gamma_3\vec{\ell}_3 + \Gamma_4\vec{\ell}_4}{4\Delta A}) \times \vec{n} \qquad\qquad (C.3)$$

Note that this expression yields a tangential velocity jump which either must be interpreted as being constant on the element, or it must be understood to apply only at control points located at the average of the panel corner points.

90

Table 1 Comparison of the small α solution by Maruhn with the exact solution by Lamb for an ellipsoid of SR=5 along top meridian line.

X/L	C_p at α = 5°			C_p at α = 10°		
	MARUHN	LAMB	DEVIATION	MARUHN	LAMB	DEVIATION
.0375	-.04460	-.04223	-.00236	-.18241	-.17024	-.01217
.0875	-.12783	-.12164	-.00619	-.22203	-.19556	-.02647
.1375	-.14472	-.13736	-.00736	-.21531	-.18466	-.03065
.1875	-.14836	-.14046	-.00790	-.20303	-.17055	-.03248
.2375	-.14747	-.13927	-.00820	-.19002	-.15661	-.03341
.2875	-.14453	-.13615	-.00839	-.17712	-.14322	-.03390
.3375	-.14042	-.13194	-.00847	-.16437	-.13025	-.03412
.3875	-.13549	-.12696	-.00853	-.15163	-.11745	-.03417
.4375	-.12984	-.12130	-.00854	-.13866	-.10457	-.03409
.4875	-.12346	-.11493	-.00853	-.12521	-.09132	-.03389
.5375	-.11622	-.10773	-.00849	-.11095	-.07737	-.03358
.5875	-.10789	-.09948	-.00841	-.09546	-.06232	-.03314
.6375	-.09811	-.08981	-.00830	-.07815	-.04559	-.03256
.6875	-.08630	-.07815	-.00815	-.05815	-.02639	-.03176
.7375	-.07145	-.06353	-.00792	-.03408	-.00340	-.03068
.7875	-.05174	-.04416	-.00758	-.00348	0.02565	-.02217
.8375	-.02341	-.01636	-.00705	0.03859	0.06531	-.02672
.8875	0.02292	0.02900	-.00608	0.10393	0.12643	-.02250
.9375	0.11984	0.12366	-.00382	0.23179	0.24468	-.01289
.9875	0.53989	0.53197	-.00793	0.71349	0.67851	-.03497
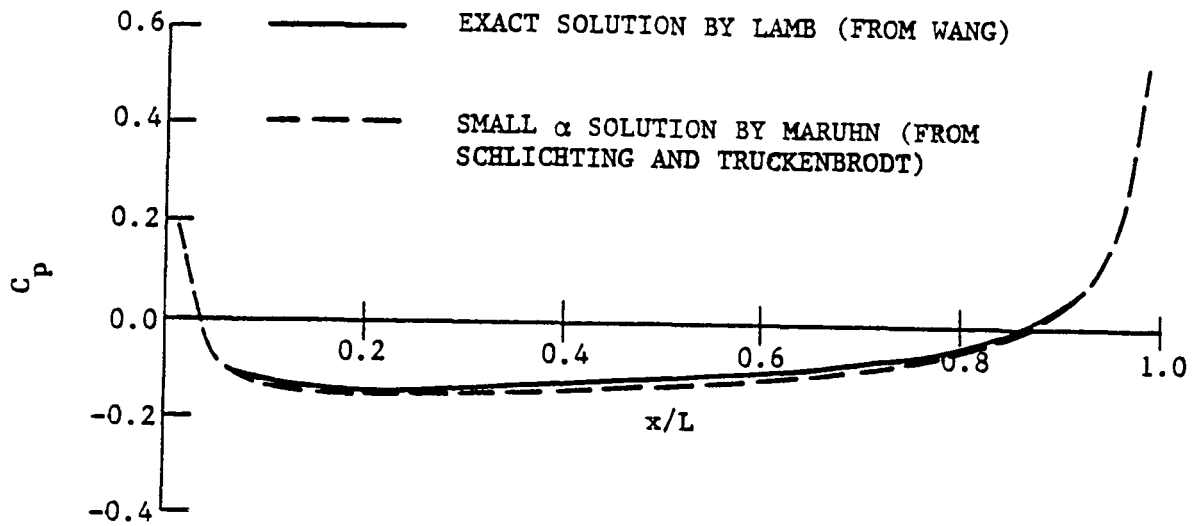
(a) $\alpha = 5°$
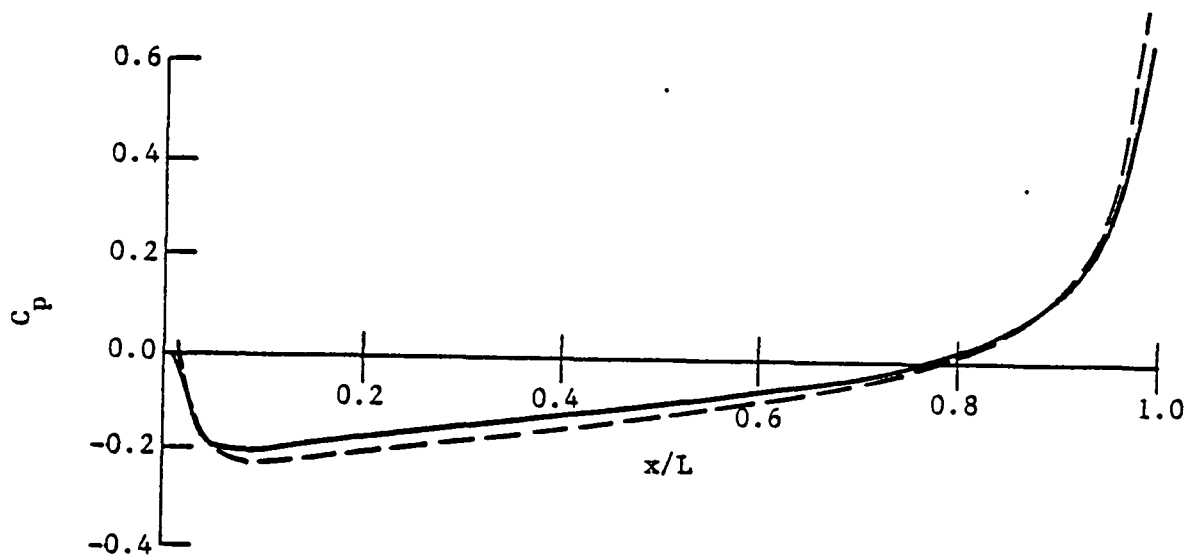
(b) $\alpha = 10°$

Figure 1. Comparisons of pressure distribution along top
meridian line ($\theta = 0°$) at $\alpha = 5°$ and $\alpha = 10°$, for
exact solution and small α solution for ellipsoid
of SR = 5.

Table 2 Solution accuracy for axial singularity method for axisymmetric flow past an ellipsoid of SR=5.

Config. No.	Axial Flow Numerical Arrangement			Inset Panelling a/L*100	Root Mean Square Error
	Singularity Type	Number of Elements	Panelling Scheme		
1	CS	10	Equal	0	0.054962
2	CS	10	Cosine	1	0.001758
3	CS	20	Equal	0	0.052254
4	CS	20	Equal	0.5	0.026120
5	CS	20	Equal	1	0.001695
6	CS	20	Equal	1.5	0.025122
7	CS	20	Equal	2	0.040193
8	CS	20	Cosine	0	0.006483
9	CS	20	Cosine	1	0.000089
10	CD	20	Equal	1	0.347660
11	LVD	20	Equal	0	0.052254
12	LVD	20	Equal	1	0.001688
13	LVS	20	Equal	1	0.000503
14	LVS	20	Cosine	1	0.000063
15	CS	20	Equal	0.75	0.012057
16	CS	20	Equal	1.75	0.014300
17	CS	40	Equal	1	0.000062
18	CS	40	Cosine	1	0.000008
19	LVS	10	Equal	1	0.000595
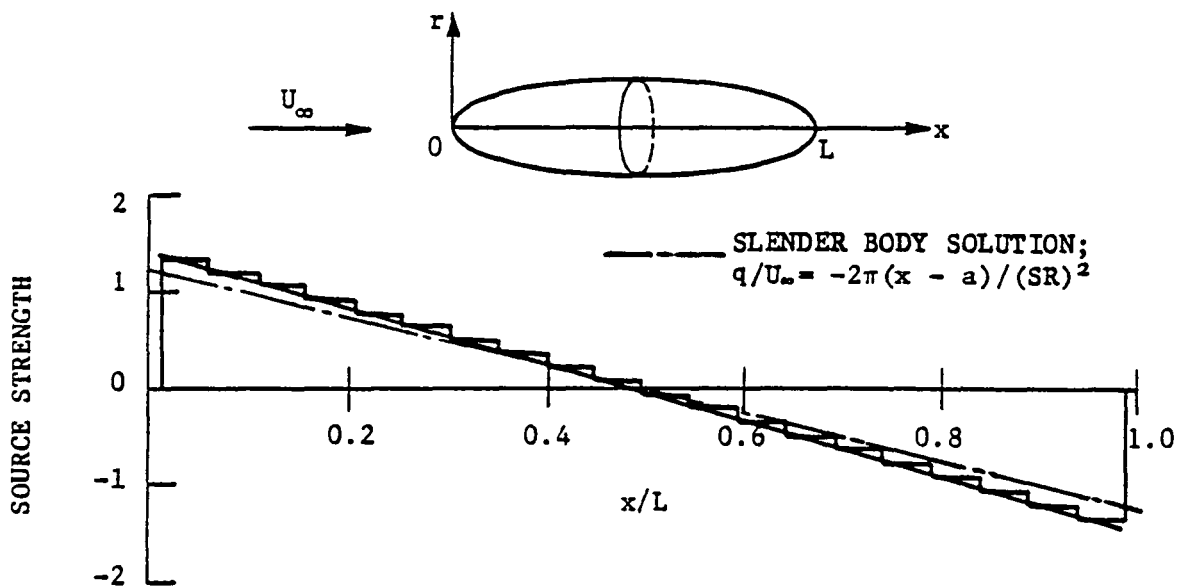
(a) Piecewise constant source and linearly varying source.
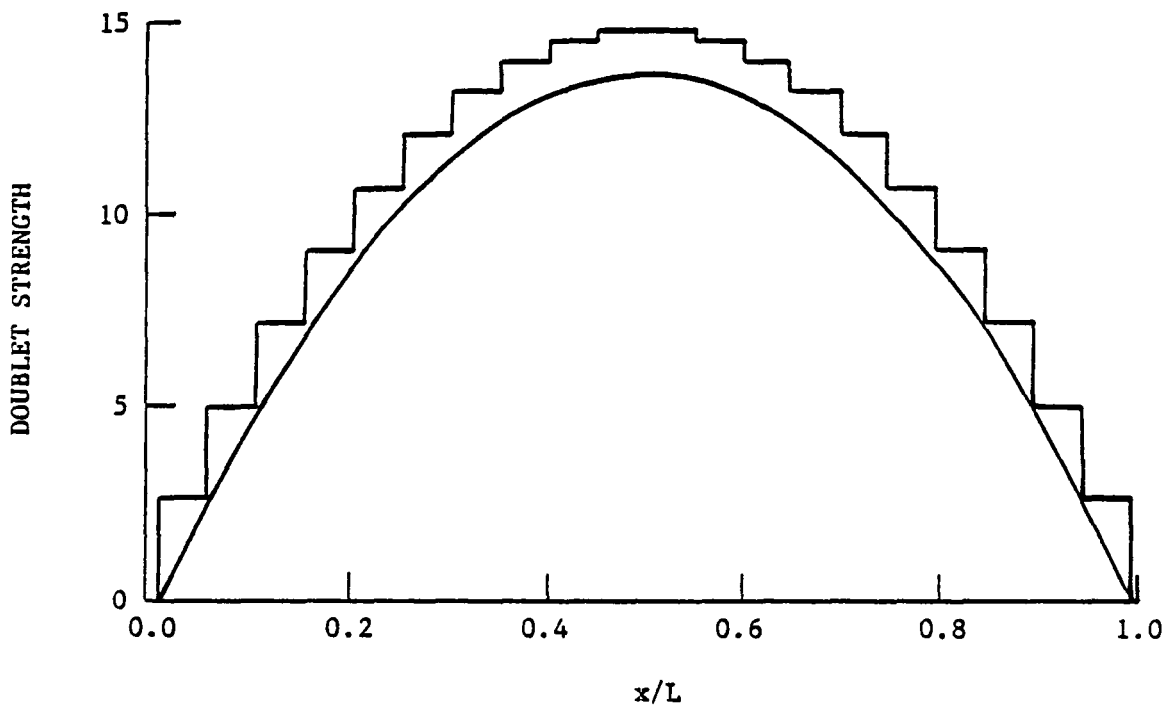
(b) Piecewise constant doublet and linearly varying doublet.

Figure 2.   Axial singularity strength distribution along body
             axis for ellipsoidal body, SR = 5, $\alpha = 0°$, equally
             spaced panels and a/L = 0.01.
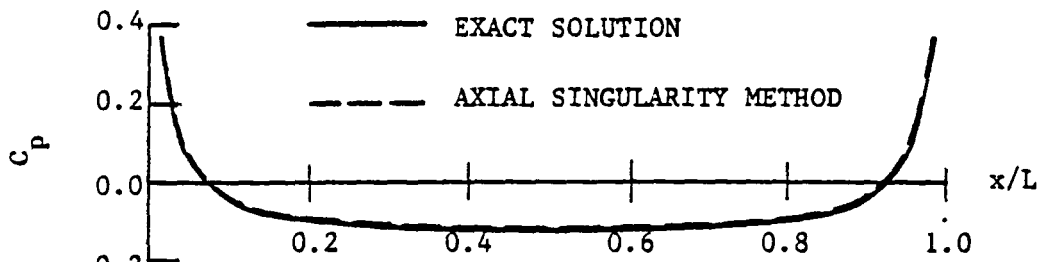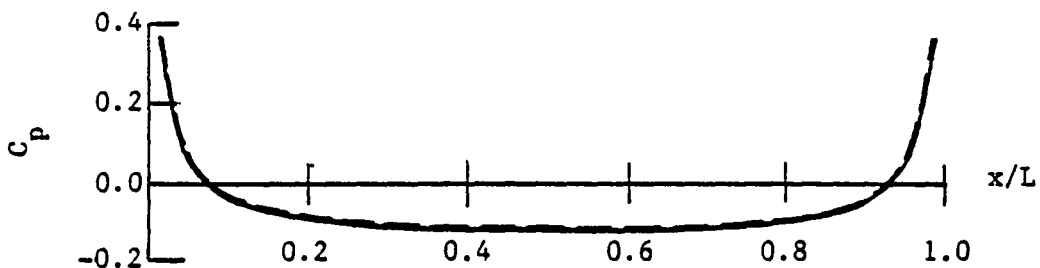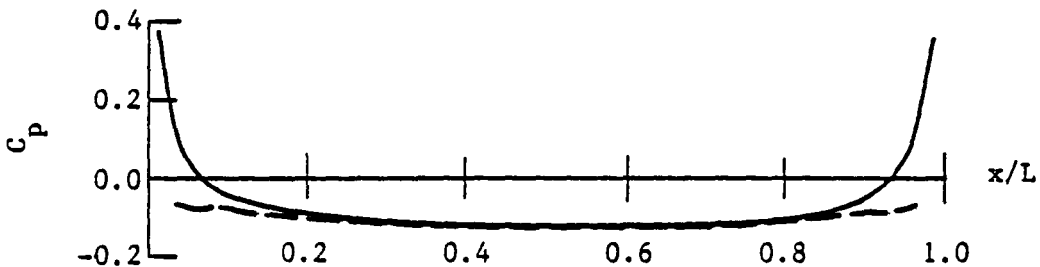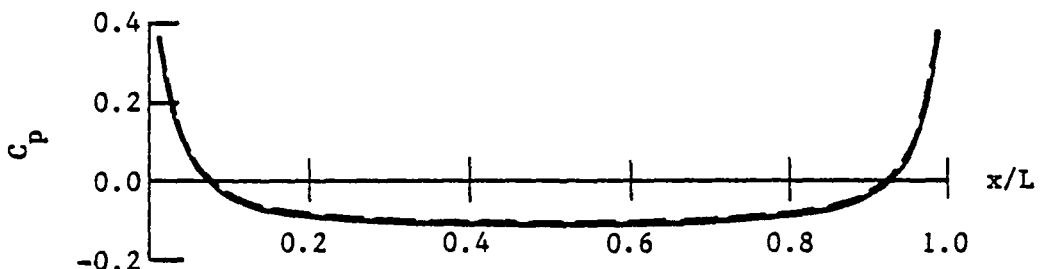
Figure 3. Pressure coefficient distribution from axial singularity method along meridian line for ellipsoidal body, SR = 5, α = 0°, equally spaced panels with a/L = 0.01.

Table 3   Comparison of Cp error for various of axial singularity
types for axisymmetric flow past an ellipsoid of SR=5.

| X/L | DEVIATION FROM EXACT SOLUTION   x 10^{-4} | | | |
	CONSTANT SOURCE	LINEARLY VARYING SOURCE	CONSTANT DOUBLET	LINEARLY VARYING DOUBLET
.0375	26.209	-4.542	-1616.645	26.209
.0875	4.91	-0.910	-449.064	4.909
.1375	2.075	-0.423	-204.528	2.075
.1875	1.165	-0.248	-118.926	1.165
.2375	0.773	-0.168	-79.899	0.774
.2875	0.571	-0.125	-59.278	0.570
.3375	0.455	-0.101	-47.489	0.455
.3875	0.388	-0.086	-40.605	0.388
.4375	0.352	-0.078	-36.834	0.352
.4875	0.377	-0.075	-35.347	0.337
.5375	0.342	-0.076	-35.847	0.342
.5875	0.366	-0.082	-38.436	0.366
.6375	0.416	-0.093	-43.657	0.415
.6875	0.501	-0.111	-52.766	0.501
.7375	0.648	-0.144	-68.473	0.648
.7875	0.913	-0.201	-97.087	0.913
.8375	1.438	-0.317	-155.847	1.438
.8875	2.716	-0.600	-306.678	2.715
.9375	7.094	-1.618	-921.745	7.090
.9875	70.616	21.952	-15422.648	69.703
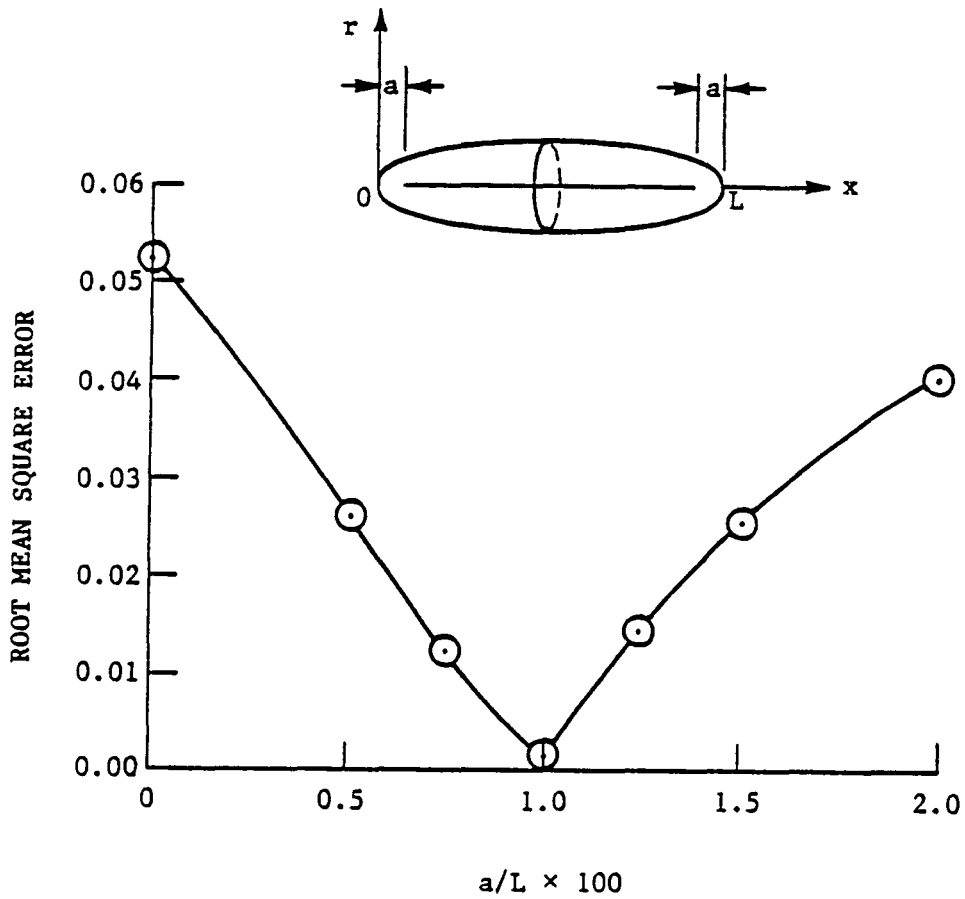
Figure 4. Effect of inset of axial singularity
distribution for an ellipsoid of SR = 5,
for equally spaced constant source
panels.

Table 4 Solution accuracy for axisymmetric flow past
ellipsoids, using 20 cosine spaced linearly
varying axial source panels.

config. No.	inset a/L%	root mean square root
1	2	0.146652
2	3	0.002798
3	4	0.001519
4	5	0.000047
5	6	0.000045
6	7	0.000078

(a) Solution accuracy for various inset
values of SR=2 ellipsoid

config. No.	inset a/L%	root mean square error
1	0	0.000330
2	0.1	0.000597
3	0.2	0.000301
4	0.25	0.000004
5	0.3	0.000381
6	0.4	0.001423
7	0.6	0.004844
8	0.8	0.010803
9	1.0	0.019887

(b) Solution accuracy for various inset
values for SR=10 ellipsoid

config. No.	SR	inset a/L%	root mean square error
1	2	6	0.000045
2	3	2.78	0.000095
3	4	1.56	0.000106
4	5	1	0.000063
5	6	0.7	0.000005
6	7	0.51	0.000022
7	8	0.4	0.000061
8	9	0.3	0.000068
9	10	0.25	0.000004

(c) Solution accuracy for various SR
ellipsoids, using the suggested
inset value calculated by equation
(2.69)
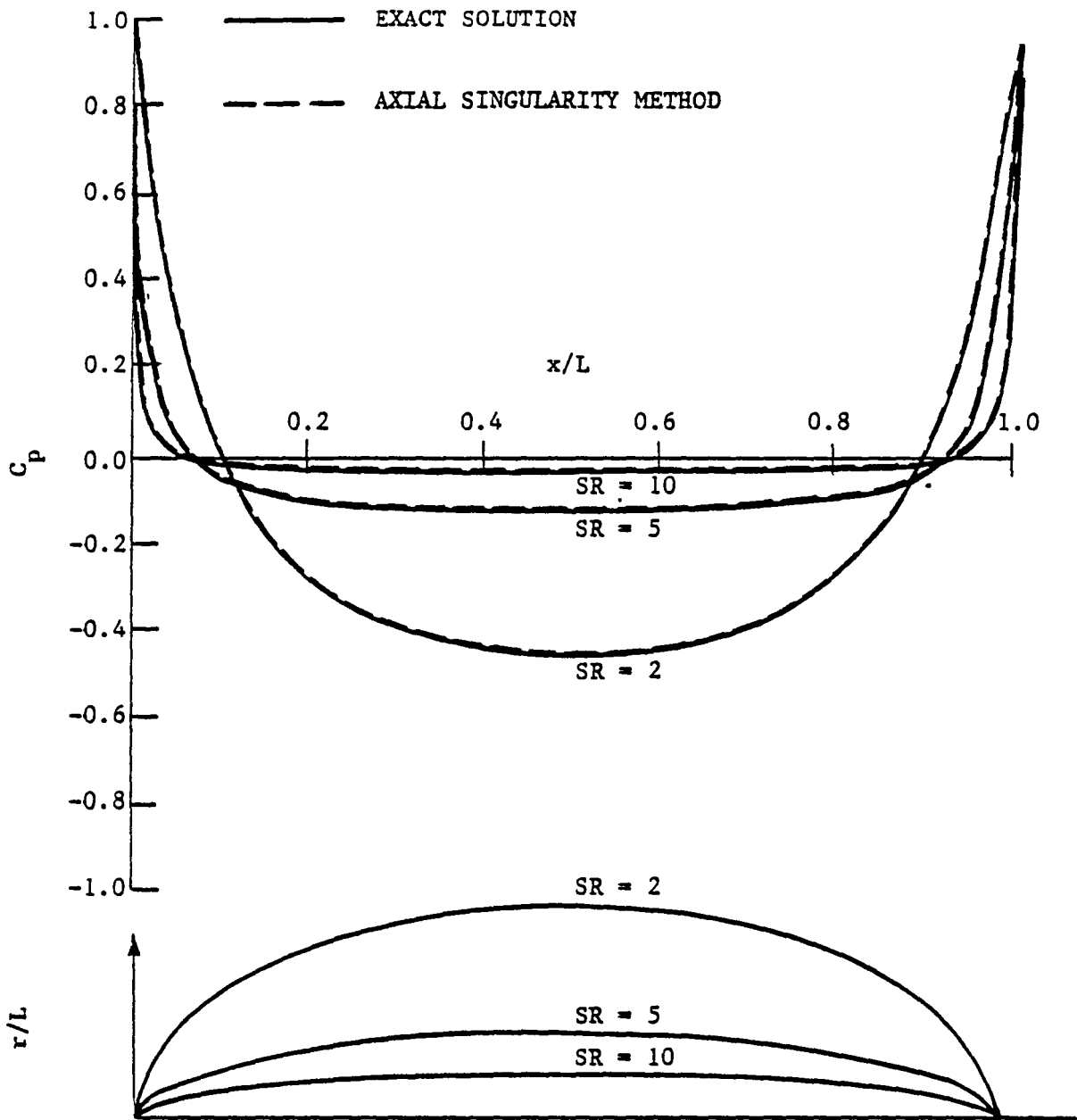
Figure 5. Pressure coefficient distribution for various SR
ellipsoids, using the suggested inset value calculated
by equation (2.69), 20 cosine spaced, linearly varying
axial source panels.
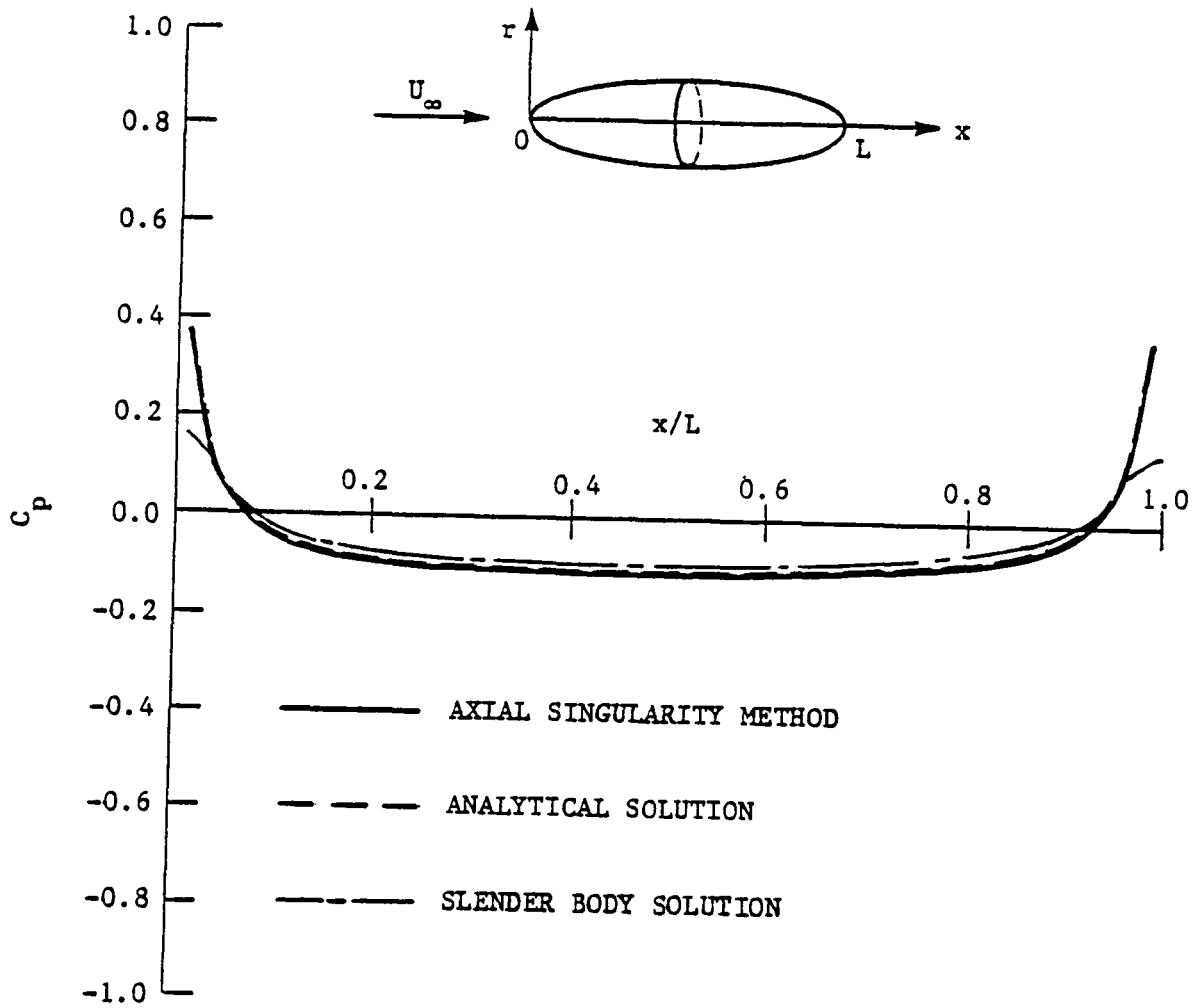
Figure 6. Pressure coefficient distribution along meridian line for ellipsoid of SR = 5, at α = 0°, cosine spaced linearly varying axial source with a/L = 0.01 (optimal panelling).
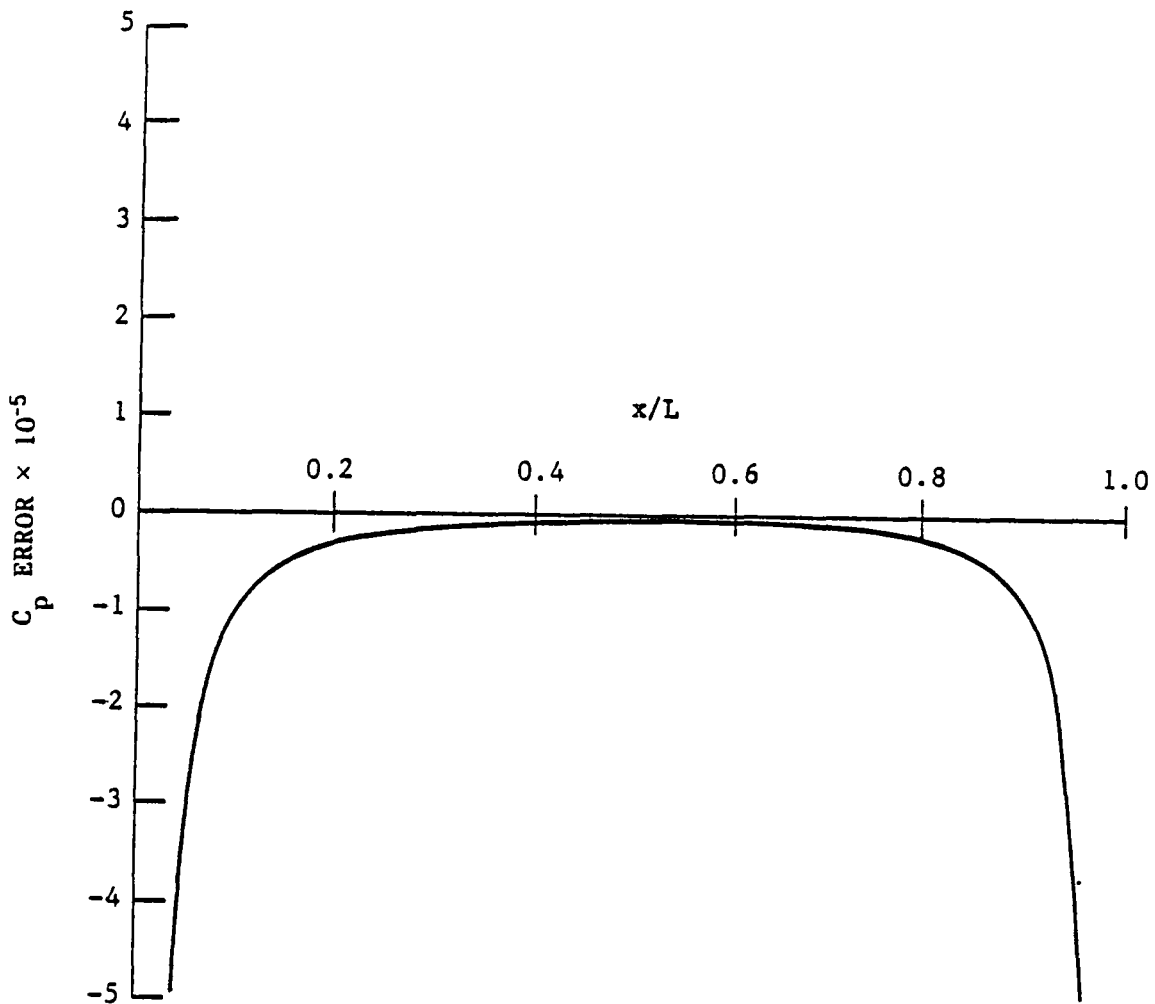
Figure 7. Error distribution along meridian line for an ellipsoid of SR = 5, at α = 0°, cosine spaced linearly varying axial source with a/L = 0.01 (optimal panelling).

Table 5 Solution accuracy for axial singularity method for inclined flow
with 5° angle of attack past an ellipsoid of SR=5; error
calculated along θ = 33.75⁰ meridian line on body surface.

| CONFIG. NO. | CROSS FLOW-NUMERICAL ARRANGEMENT | | | | ROOT MEAN SQUARE ERROR |
	SINGULARITY TYPE	ELEMENT NO.	PANELLING SCHEME	$(a/L)*100$	
1	CD*	20	EQUAL	0	0.019056
2	CD*	20	EQUAL	1	0.010986
3	CD*	20	COSINE	0	0.002012
4	CD*	20	COSINE	1	0.000117
5	LVD*	20	EQUAL	0	0.005749
6	LVD*	20	EQUAL	1	0.000129
7	LVD*	20	COSINE	0	0.011609
8	LVD*	20	COSINE	1	0.000088
9	LVD⁺	20	COSINE	1	0.000062

* - CONFIGURATIONS BASED ON FIXED CONDITIONS IN AXIAL FLOW: 20 DISCRETE
ELEMENTS, COSINE SPACING, CONSTANT SOURCE WITH a/L = 0.01.

+ - AXIAL FLOW CHANGED TO 20 DISCRETE ELEMENTS, COSINE SPACING, LINEARLY
VARYING SOURCE WITH a/L = 0.01, THE OPTIMAL NUMERICAL ARRANGEMENT FOR
INCLINED FLOW.
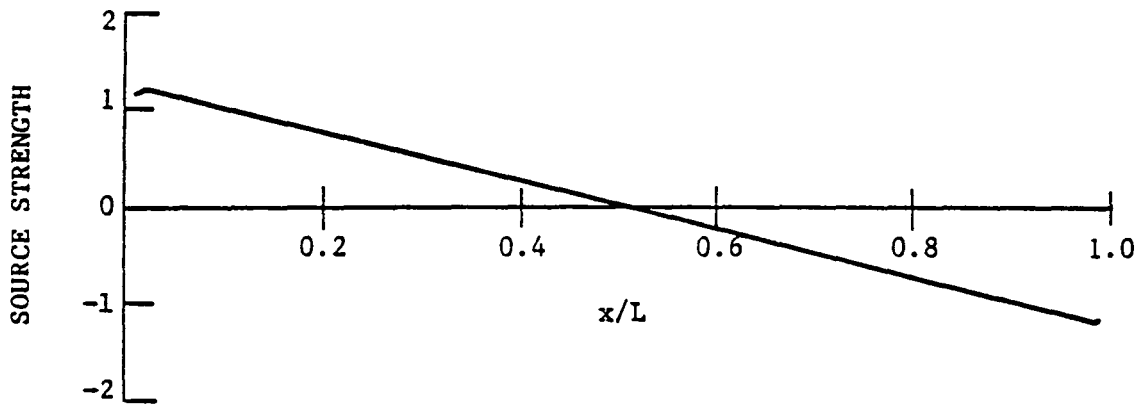
(a) Axial flow: 20 discrete elements, cosine spaced linearly
varying source with a/L = 0.01.
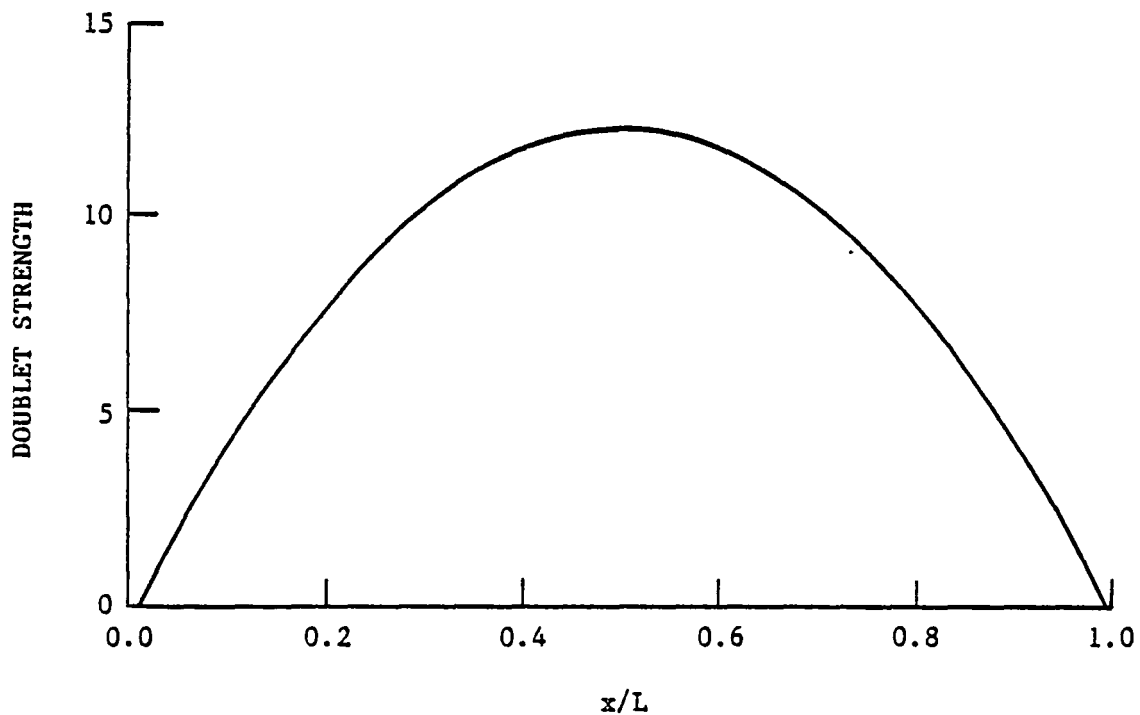
(b) Cross flow: 20 discrete elements, cosine spaced linearly
varying doublet with a/L = 0.01.

Figure 8.   Axial singularity strength distribution along body
axis, for an ellipsoid of SR = 5, at α = 30°, for
optimal panelling.
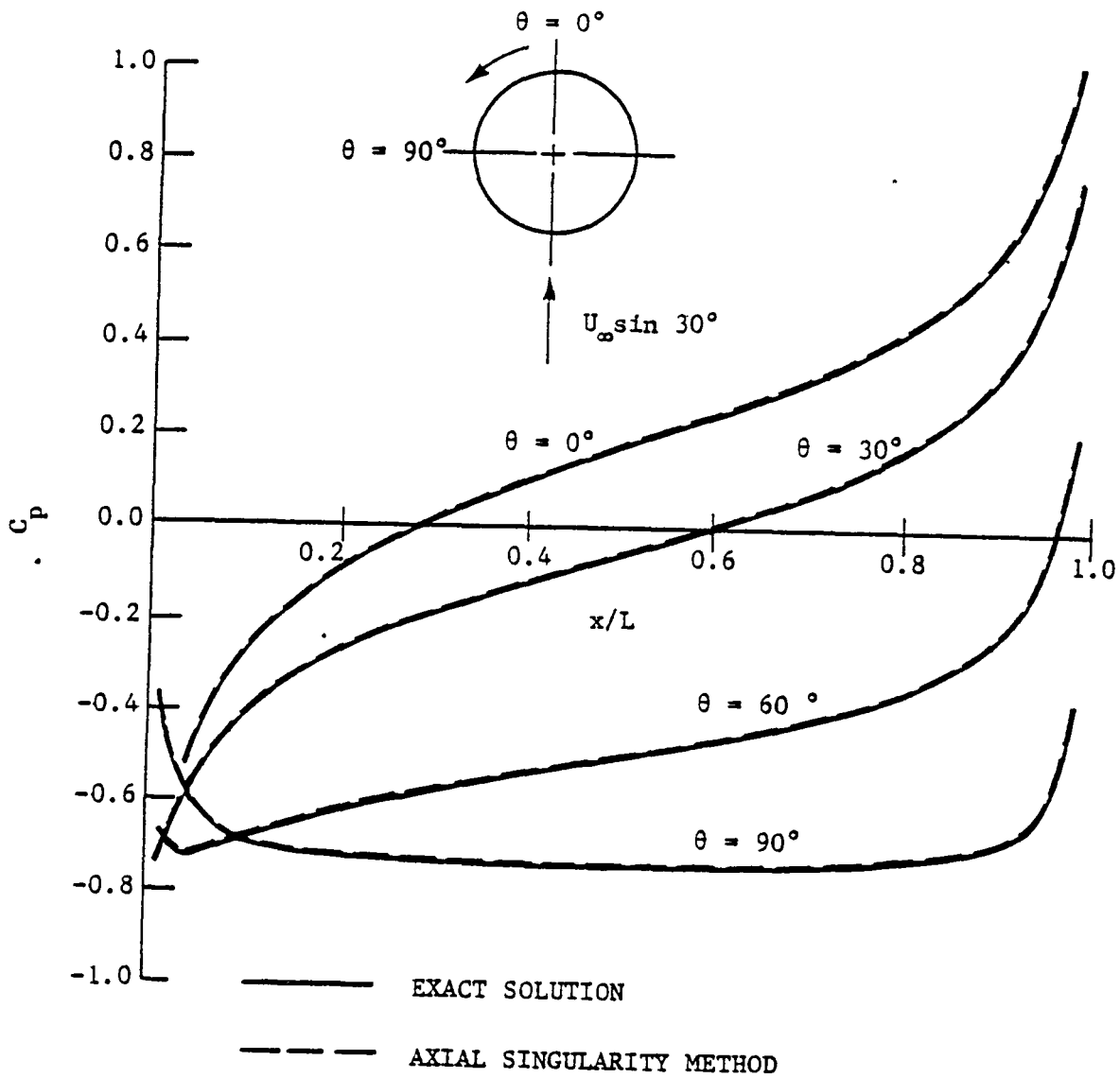
Figure 9.   Pressure coefficient distribution from axial
singularity method for an ellipsoid of SR = 5,
at α = 30°, for optimal panelling, various meridian
lines on body; θ = 0°, θ = 30°, θ = 60° and θ = 90°.
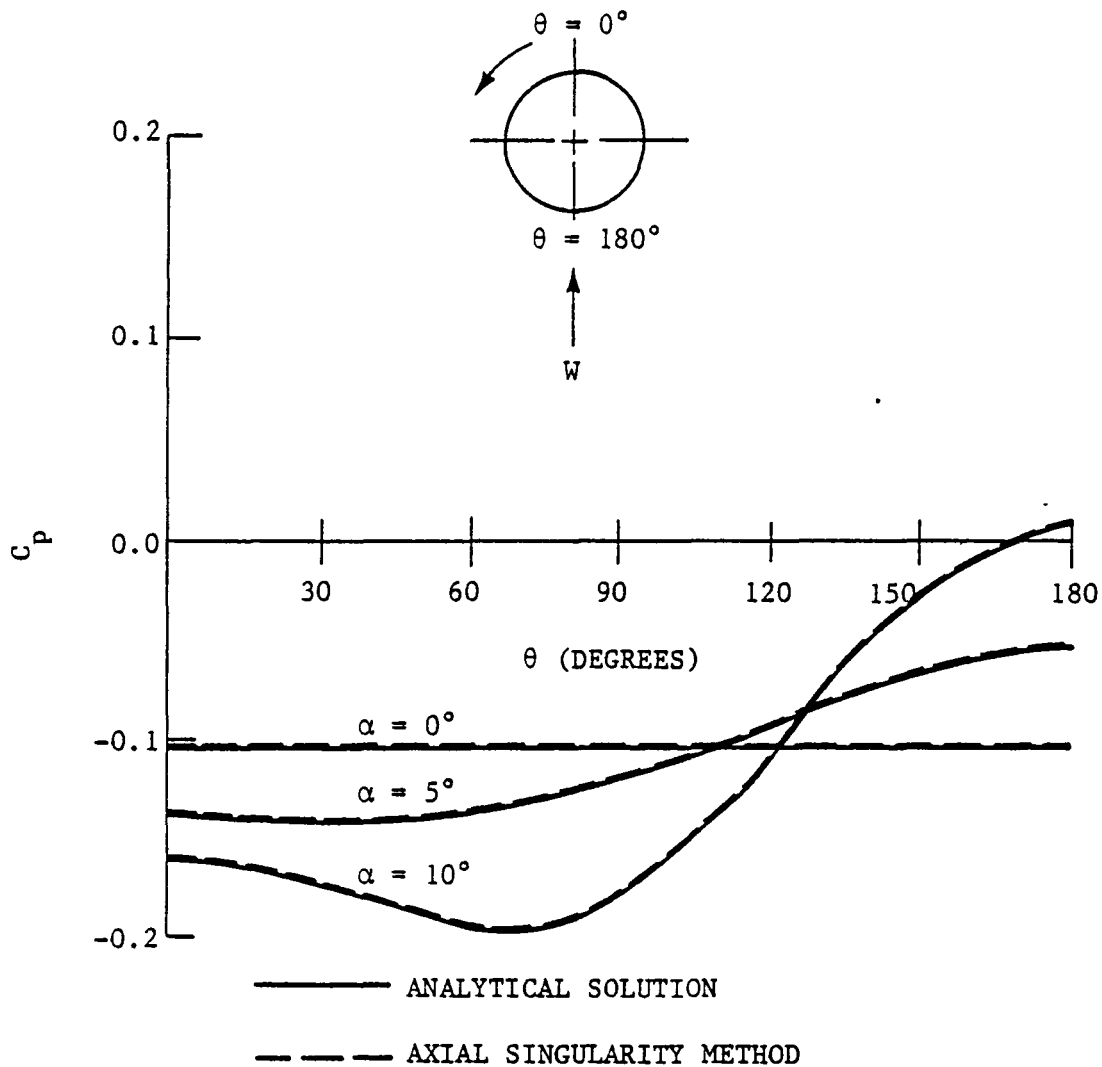
Figure 10. Pressure coefficient distribution from axial
singularity method along circumferential line
at x/L = 0.2375 cross section, for an ellipsoid
of SR = 5, at $\alpha = 0°$, $\alpha = 5°$ and $\alpha = 10°$,
for the optimal panelling.
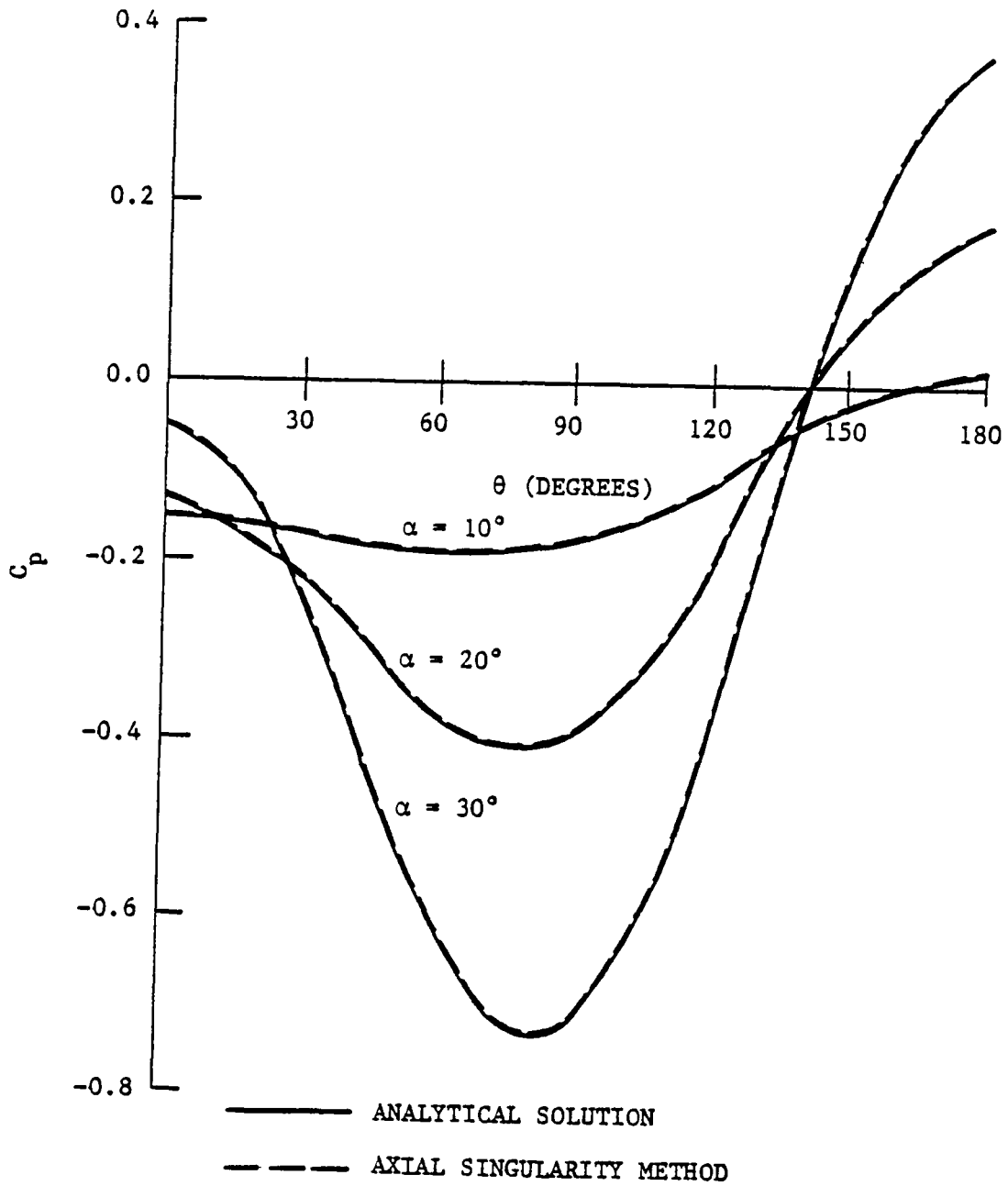
Figure 11. Pressure coefficient distribution from axial singularity method along circumferential line at x/L = 0.2375 cross section, for an ellipsoid of SR = 5, at α = 10°, α = 20° and α = 30° for the optimal panelling.

106

Figure 12. Pressure coefficient distribution from axial
singularity method along top meridian line ($\theta = 0°$)
on body surface, for an ellipsoid of SR = 5, at
$\alpha = 0°$, $\alpha = 10°$, $\alpha = 20°$ and $\alpha = 30°$ for the optimal
panelling.
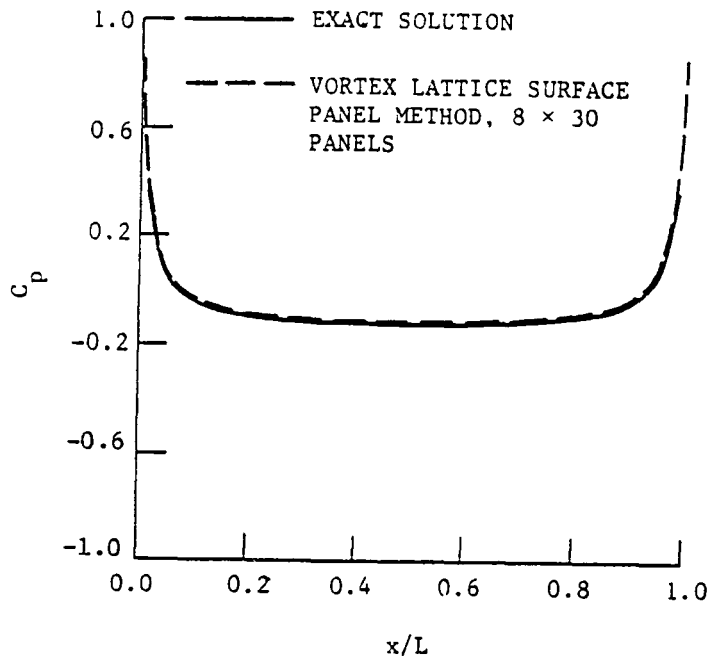
(a) Cosine axial panel distribution.
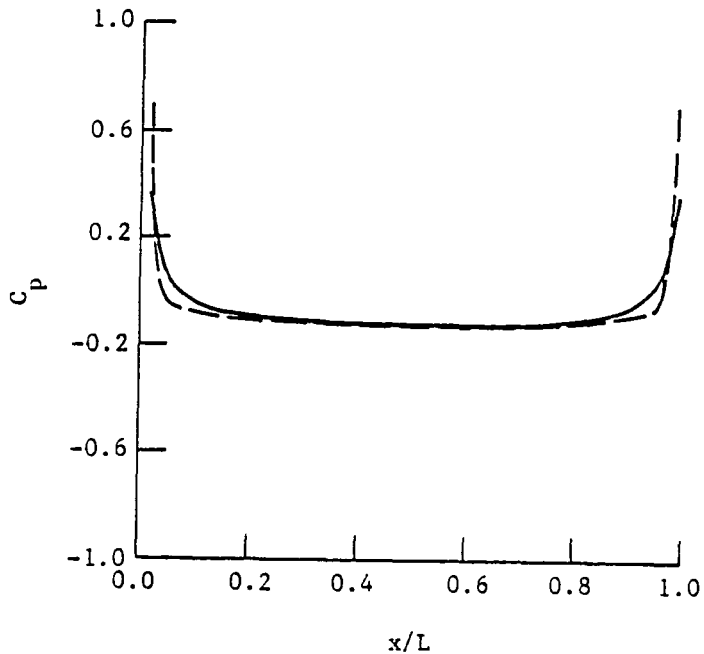
(b) Equal axial panel distribution.

Figure 13. Pressure coefficient distribution from vortex
lattice method along meridian line for ellipsoidal
body, SR = 5, $\alpha = 0^\circ$, using modified tangential
velocity calculation method.

Table 6 Comparison of Cp from vortex lattice method for various of tangential velocity calculation methods for axisymmetric flow past an ellipsoid of SR=5, using 8*30 panels, cosine spacing axially, and control point located at the average of four corner coordinates of each panel.

x/L	Cp EXACT	Cp NUMERICAL		
		KANDIL (1977)	ATTA (1978)	MODIFIDIED (equ. 3.20)
.00137	.864390	.9329	.8387	.8387
.01770	.269314	.2868	.2607	.2607
.05511	.026309	.0276	.0180	.0180
.11196	-.057666	-.0629	-.0670	-.0670
.18577	-.093193	-.1016	-.1035	-.1035
.27332	-.110248	-.1203	-.1211	-.1211
.37077	-.118535	-.1295	-.1297	-.1297
.47387	-.121615	-.1329	-.1329	-.1329
.57811	-.120616	-.1318	-.1319	-.1319
.67894	-.115183	-.1258	-.1262	-.1262
.77195	-.103200	-.1126	-.1138	-.1138
.85307	-.078821	-.0859	-.0887	-.0887
.91876	-.025376	-.0280	-.0342	-.0342
.96616	.113794	.1211	.1057	.1057
.99317	.539069	.5755	.5286	.5286

Table 7 Comparison of Cp from vortex lattice method for various of
tangential velocity calculation methods for axisymmetric flow
past an ellipsoid of SR=5, using 8*30 panels, cosine spacing
axially, and control point located at the centroid of area of
each panel.

x/L	Cp EXACT	Cp NUMERICAL				
		SCHEME 1*			SCHEME 2[+]	
		KANDIL (1977)	ATTA (1978)	MODIFIED (equ 3.20)	ATTA (1978)	MODIFIED (equ. 3.20)
.00183	.825989	.9018	.8446	.8446		
.01814	.262712	.2844	.2680	.2601	.2623	.2704
.05551	.025187	.0320	.0260	.0231	.0234	.0264
.11231	-.057943	-.0560	-.0585	-.0598	-.0597	-.0584
.18606	-.093277	-.0936	-.0947	-.0953	-.0953	-.0947
.27352	-.110274	-.1118	-.1122	-.1125	-.1124	-.1122
.37089	-.118541	-.1207	-.1208	-.1209	-.1208	-.1208
.47389	-.121615	-.1240	-.1240	-.1240	-.1240	-.1240
.57804	-.120619	-.1229	-.1229	-.1230	-.1230	-.1229
.67877	-.115199	-.1171	-.1173	-.1175	-.1174	-.1173
.77170	-.103247	-.1043	-.1050	-.1054	-.1053	-.1050
.85275	-.078971	-.0783	-.0800	-.0809	-.0808	-.0800
.91838	-.025914	-.0220	-.0259	-.0278	-.0276	-.0257
.96572	.111215	.1229	.1133	.1086	.1094	.1141
.99272	.521222	.5696	.5385	.5248	.5397	.5533

* - CONTROL POINT LOCATED AT THE CENTROID OF AREA OF EACH PANEL.

+ - CONTROL POINT LOCATED AT THE CENTROID OF AREA OF EACH PANEL,
EXCEPT TRIANGULAR PANEL AT THE NOSE AND TAIL, WHERE THE CONTROL
POINT LOCATED AT 3/4 CHORD LENGTH AWAY FROM THE APEX.

Table 8 Comparison of Cp from vortex lattice method for various of tangential velocity calculation methods for inclined flow, α=20°, past an ellipsoid of SR=5, using 12*20 panels, cosine spacing axially, and control point located at the average of four corner coordinates of each panel.

x/L	θ = 7.5°			θ = 82.5°		
	EXACT	ATTA (1978)	MODIFIED (equ. 3.20)	EXACT	ATTA (1978)	MODIFIED (equ. 3.20)
.003080	-.100442	-.2543	-.2451	.275594	.3048	.3077
.015320	-.390676	-.4691	-.4609	-.107441	-.1122	-.1101
.039485	-.386188	-.4482	-.4426	-.288417	-.2935	-.2922
.074995	-.316861	-.3756	-.3717	-.359549	-.3643	-.3636
.12097	-.250026	-.3066	-.3038	-.389816	-.3946	-.3941
.176275	-.192597	-.2472	-.2452	-.403316	-.4081	-.4078
.239555	-.142936	-.1956	-.1942	-.408920	-.4137	-.4135
.309250	-.098582	-.1493	-.1483	-.410256	-.4150	-.4148
.383635	-.057401	-.1062	-.1056	-.408901	-.4135	-.4134
.460890	-.017586	-.0643	-.0641	-.405509	-.4099	-.4089
.539110	.022528	-.0221	-.0222	-.400228	-.4043	-.4043
.616365	.064701	.0224	.0291	-.392826	-.3965	-.3966
.690750	.111064	.0714	.0705	-.382655	-.3859	-.3860
.760445	.164558	.1279	.1267	-.368438	-.3711	-.3713
.823725	.229688	.1967	.1950	-.347721	-.3497	-.3499
.879030	.313947	.2854	.2833	-.315568	-.3167	-.3168
.925005	.430552	.4078	.4052	-.261150	-.2612	-.2613
.960515	.602127	.5874	.5843	.158303	-.1571	-.1570
.194685	.846020	.8420	.8393	.056286	.0604	.0611
.996920	.986992	.9907	.9913	.418758	.4687	.4705

Table 9 Comparison of Cp from vortex lattice method along θ = 7.5°
meridian line for various of tangential velocity calculation
methods for inclined flow, α = 20°, past an ellipsoid of
SR=5, using 12*20 panels, cosine spacing axially, and control
point located at the centroid of area of each panel.

x/L	Cp EXACT	SCHEME 1* ATTA (1978)	SCHEME 1* MODIFIED (equ. 3.20)	SCHEME 2+ ATTA (1978)	SCHEME 2+ MODIFIED (equ. 3.20)
.004105	.171617	.0539	.0363		
.016315	-.401517	-.3916	-.4074	-.3412	-.3639
.040435	-.384262	-.4131	-.4166	-.4092	-.4131
.07587	-.315345	-.3506	-.3510	-.3496	-.3500
.12175	-.249073	-.2858	-.2852	-.2854	-.2848
.176945	-.192009	-.2287	-.2277	-.2285	-.2275
.240095	-.142561	-.1785	-.1776	-.1783	-.1774
.30964	-.098351	-.1332	-.1324	-.1331	-.1323
.383875	-.057274	-.0908	-.0903	-.0907	-.0902
.46097	-.017545	-.0496	-.0495	-.0496	-.0494
.53903	-.022487	-.0080	-.0082	-.0079	-.0081
.616125	.064563	.0359	.0352	.0359	.0353
.69036	.110795	.0841	.0829	.0842	.0830
.759905	.164089	.1389	.1379	.1399	.1380
.823055	.228870	.2075	.2046	.2076	.2047
.87825	.312452	.2947	.2905	.2949	.2907
.92413	.427582	.4146	.4086	.4150	.4089
.959565	.595590	.5899	.5810	.5905	.5817
.983685	.831918	.8364	.8252	.8361	.8250
.995895	.992848	.9903	.9932		

* - CONTROL POINT LOCATED AT THE CENTROID OF AREA OF EACH PANEL.
+ - CONTROL POINT LOCATED AT THE CENTROID OF AREA OF EACH PANEL
    EXCEPT TRIANGULAR PANEL AT THE NOSE AND TAIL, WHERE THE
   CONTROL POINT LOCATED AT 3/4 CHORD LENGTH AWAY FROM THE APEX.

Table 10   Comparison of Cp from vortex lattice method along θ = 82.5°
meridian line for various of tangential velocity calculation
methods for inclined flow, α = 20°, past an ellipsoid of
SR=5, using 12*20 panels, cosine spacing axially, and control
point located at the centroid of area of each panel.

x/L	Cp EXACT	SCHEME 1*		SCHEME 2[+]	
		ATTA (1978)	MODIFIED (equ. 3.20)	ATTA (1978)	MODIFIED (equ. 3.20)
.004105	.214953	.1146	.2799		
.016315	-.122094	-.1164	-.1162	-.0979	-.1002
.040435	-.291783	-.2878	-.2896	-.2859	-.2878
.07587	-.360491	-.3545	-.3555	-.3539	-.3550
.12175	-.390117	-.3827	-.3832	-.3824	-.3830
.176945	-.403413	-.3951	-.3954	-.3950	-.3952
.240095	-.408945	-.4001	-.4002	-.4000	-.4000
.30964	-.410255	-.4010	-.4010	-.4009	-.4009
.383875	-.408893	-.3993	-.3992	-.3992	-.3992
.46097	-.405505	-.3956	-.3956	-.3956	-.3956
.53903	-.400234	-.3901	-.3902	-.3901	-.3901
.616125	-.392853	-.3826	-.3827	-.3825	-.3826
.69036	-.382720	-.3724	-.3726	-.3723	-.3725
.759905	-.368574	-.3582	-.3586	-.3581	-.3585
.823055	-.348004	-.3377	-.3385	-.3375	-.3383
.87825	-.316190	-.3063	-.3075	-.3060	-.3072
.92413	-.262683	-.2537	-.2555	-.2532	-.2550
.959565	-.162783	-.1558	-.1582	-.1543	-.1569
.983685	.040291	.0453	.0460	.0571	.0563
.995895	.368258	.2520	.4155		

* - CONTROL POINT LOCATED AT THE CENTROID OF AREA OF EACH PANEL.
+ - CONTROL POINT LOCATED AT THE CENTROID OF AREA OF EACH PANEL
   EXCEPT TRIANGULAR PANEL AT THE NOSE AND TAIL, WHERE THE
   CONTROL POINT LOCATED AT 3/4 CHORD LENGTH AWAY FROM THE APEX.
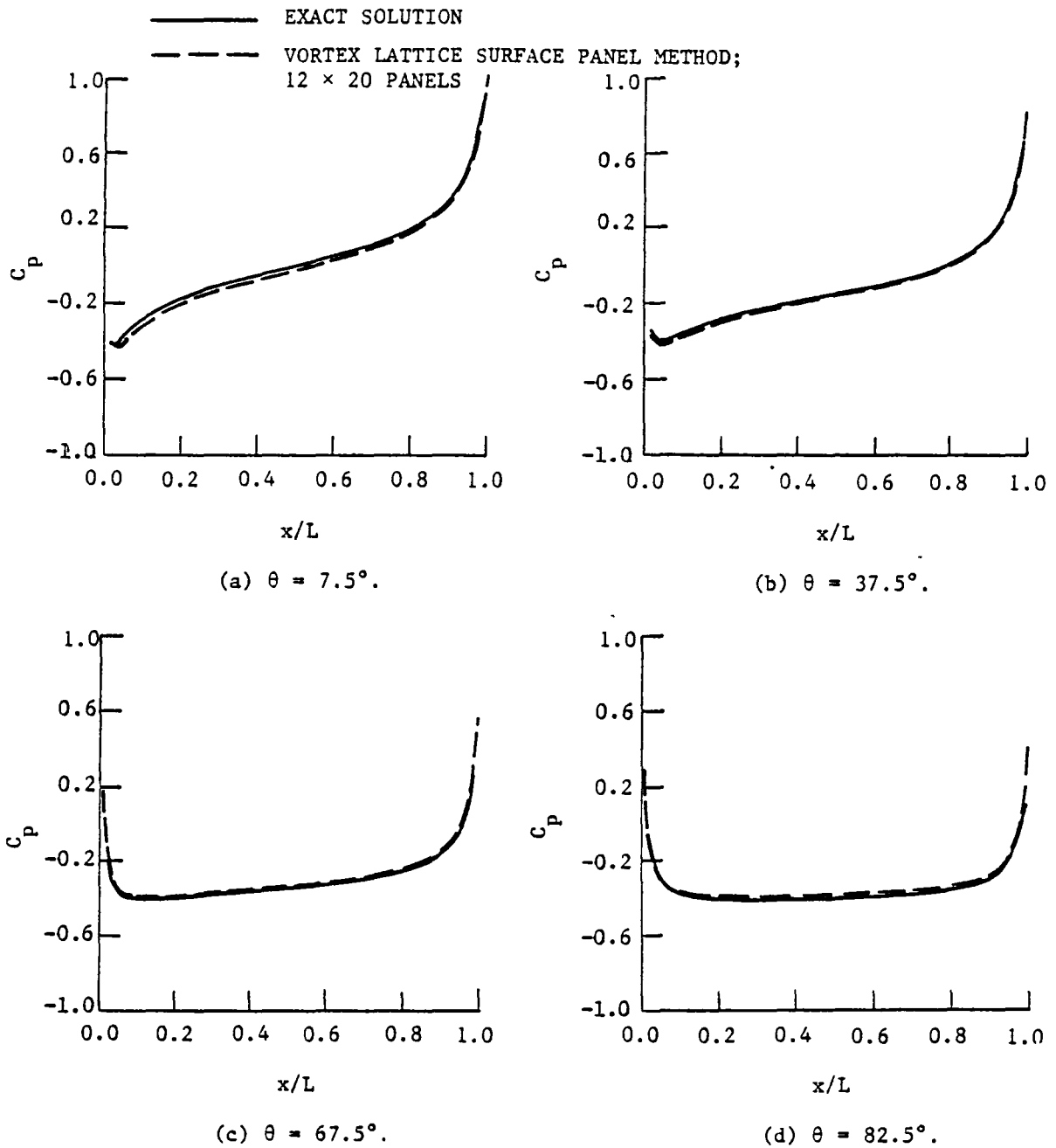
Figure 14. Pressure coefficient distributions from vortex lattice method
along various meridian lines for ellipsoidal body, SR = 5,
α = 20°, using modified tangential velocity calculation
method.

114

EXACT SOLUTION
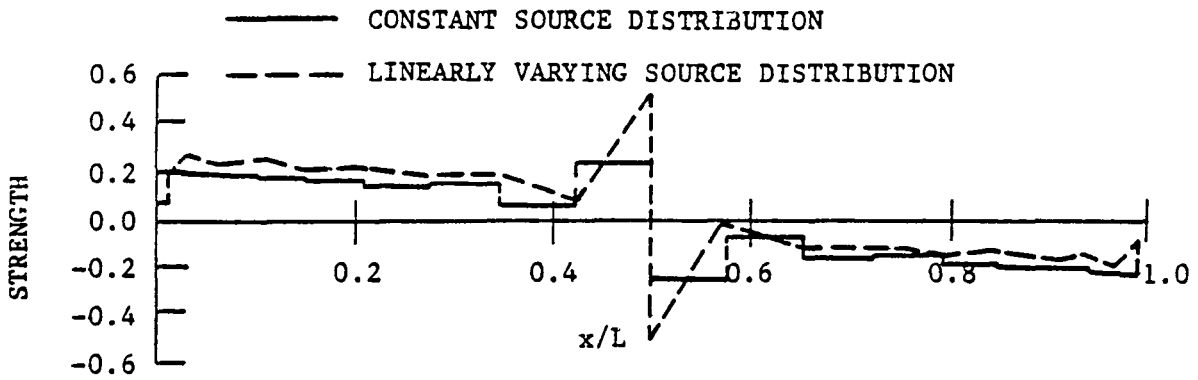
VORTEX LATTICE SURFACE PANEL METHOD; 12 × 20 PANELS

(a) x/L = 0.00962.

(b) x/L = 0.12175.

(c) x/L = 0.38388.

(d) x/L = 0.53903.

(e) x/L = 0.69036.

(f) x/L = 0.92413.
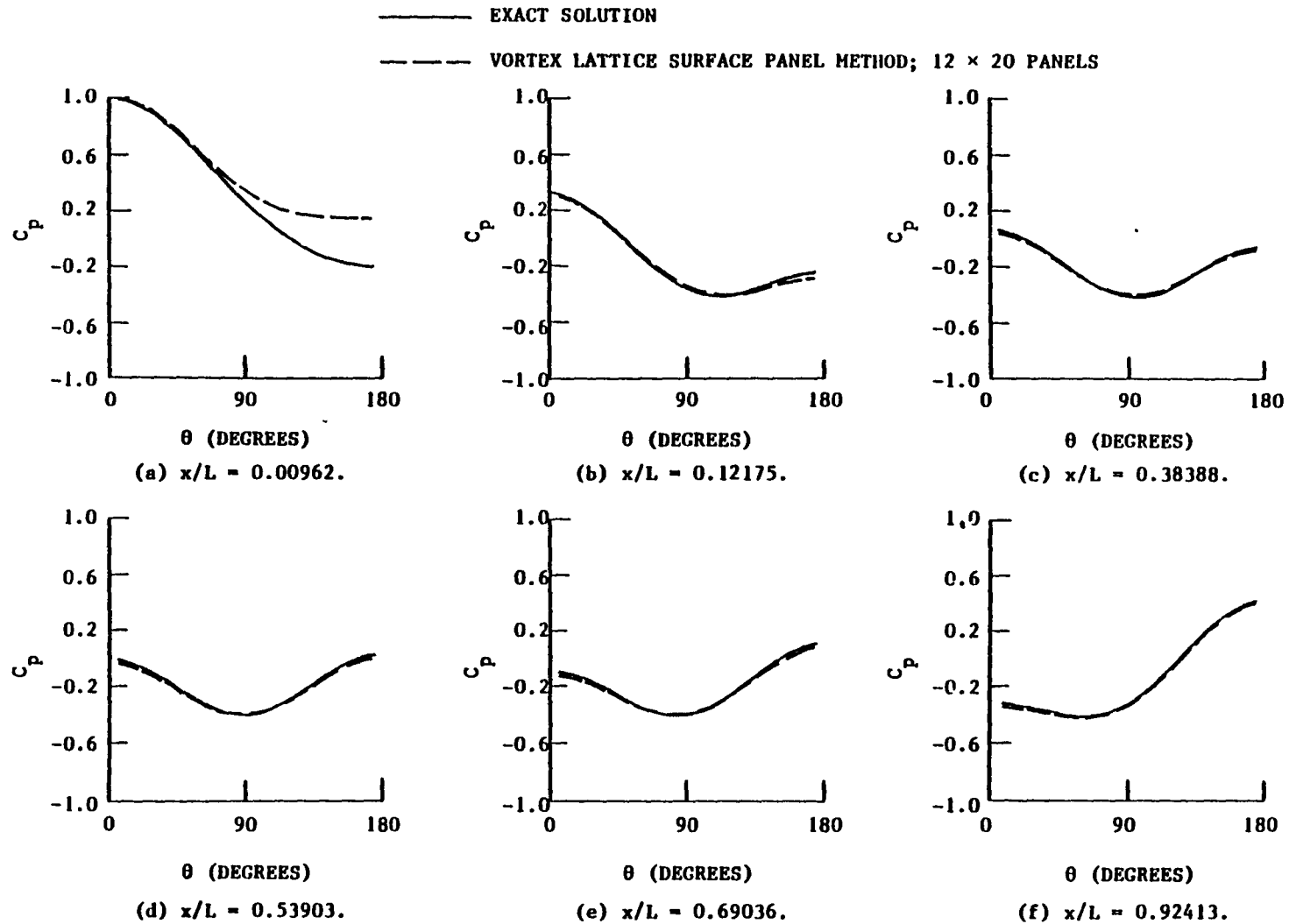
Figure 15.   Pressure coefficient distributions from vortex lattice method along circumferential
lines at various x/L values for ellipsoidal body, SR = 5, α = 20°, using modified
tangential velocity calculation method.

(a) Source strength distribution along body axis.
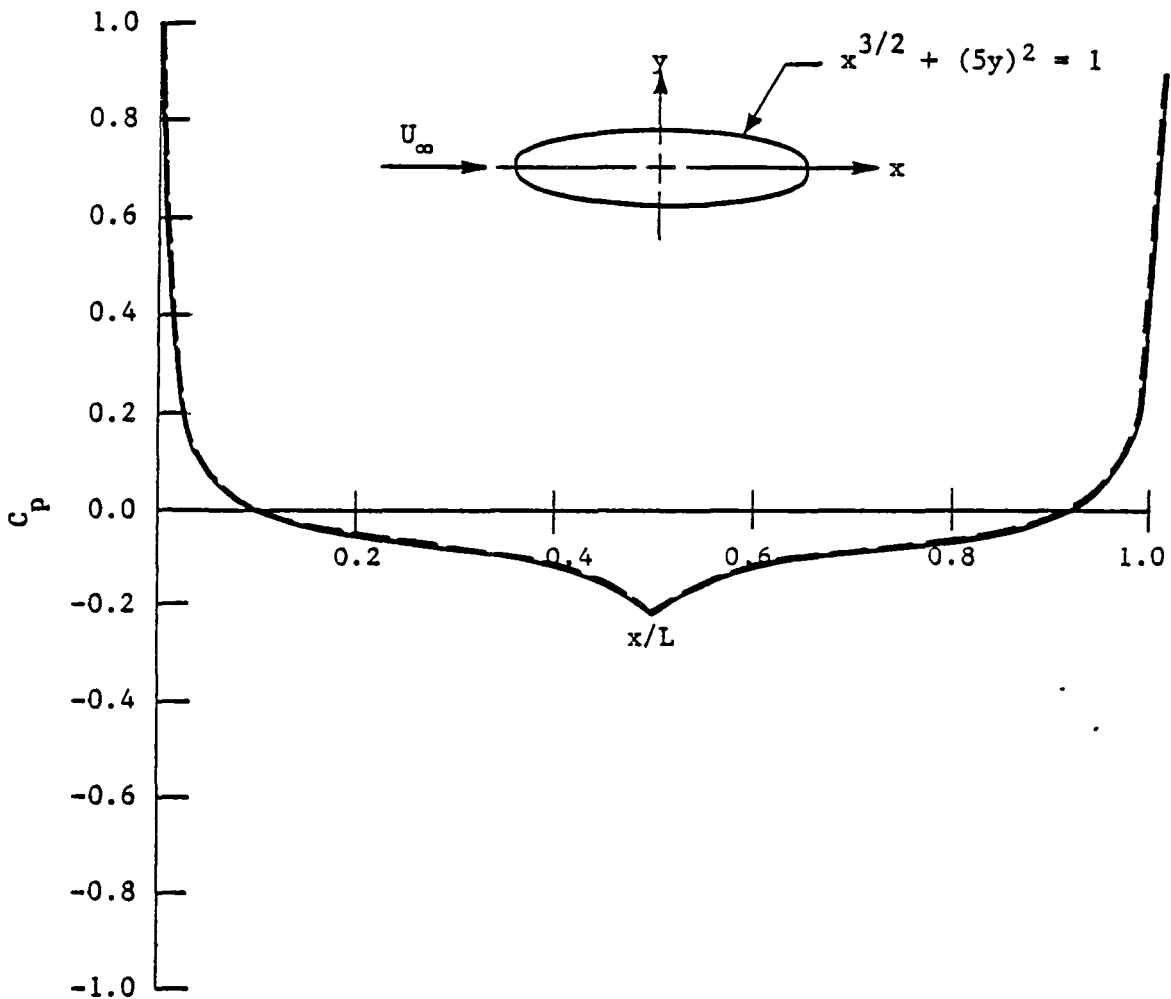
(b) Pressure distribution along meridian line.

Figure 16. Axial singularity strength, and C_p distribution, for a SR = 5, modified ellipsoid given by equation (4.1), using 20 cosine spaced, constant and linearly varying axial sources.
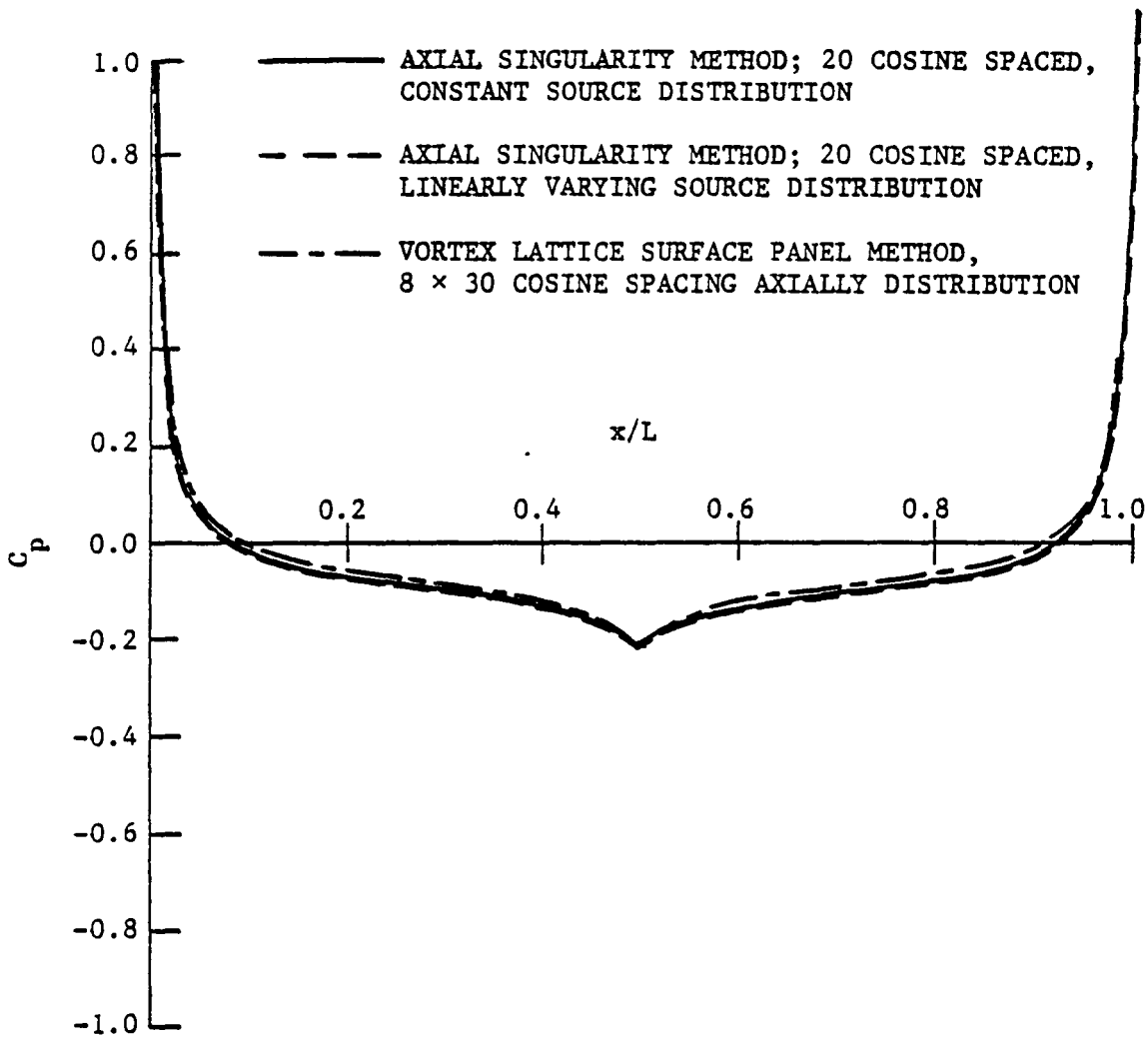
Figure 17. Pressure coefficient distribution for a SR = 5, modified
ellipsoid given by equation (4.1), using axial singularity
method and vortex lattice surface panel method.
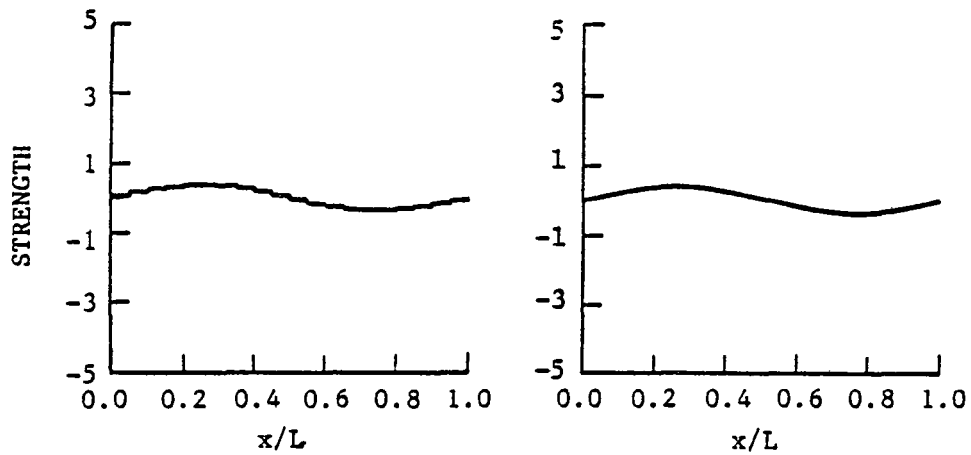
(a) Strength distribution using constant source panels.

(b) Strength distribution using linearly varying source panels.
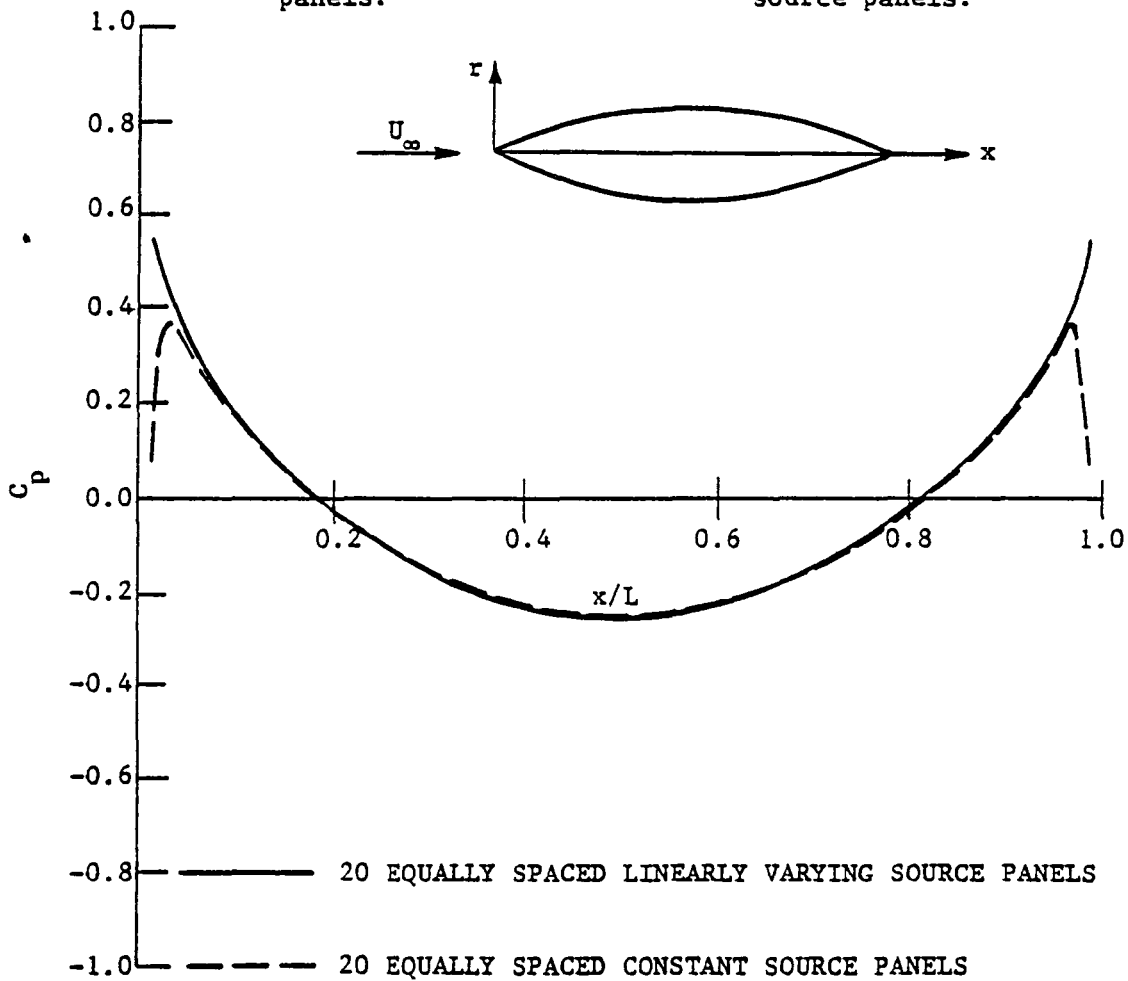
(c) Pressure coefficient distribution along meridian line.

Figure 18. Axial singularity strength, and C_p distribution, for axisymmetric flow past a SR = 4, Ogival body of revolution, using 20 equal spaced, constant and linearly varying axial sources.
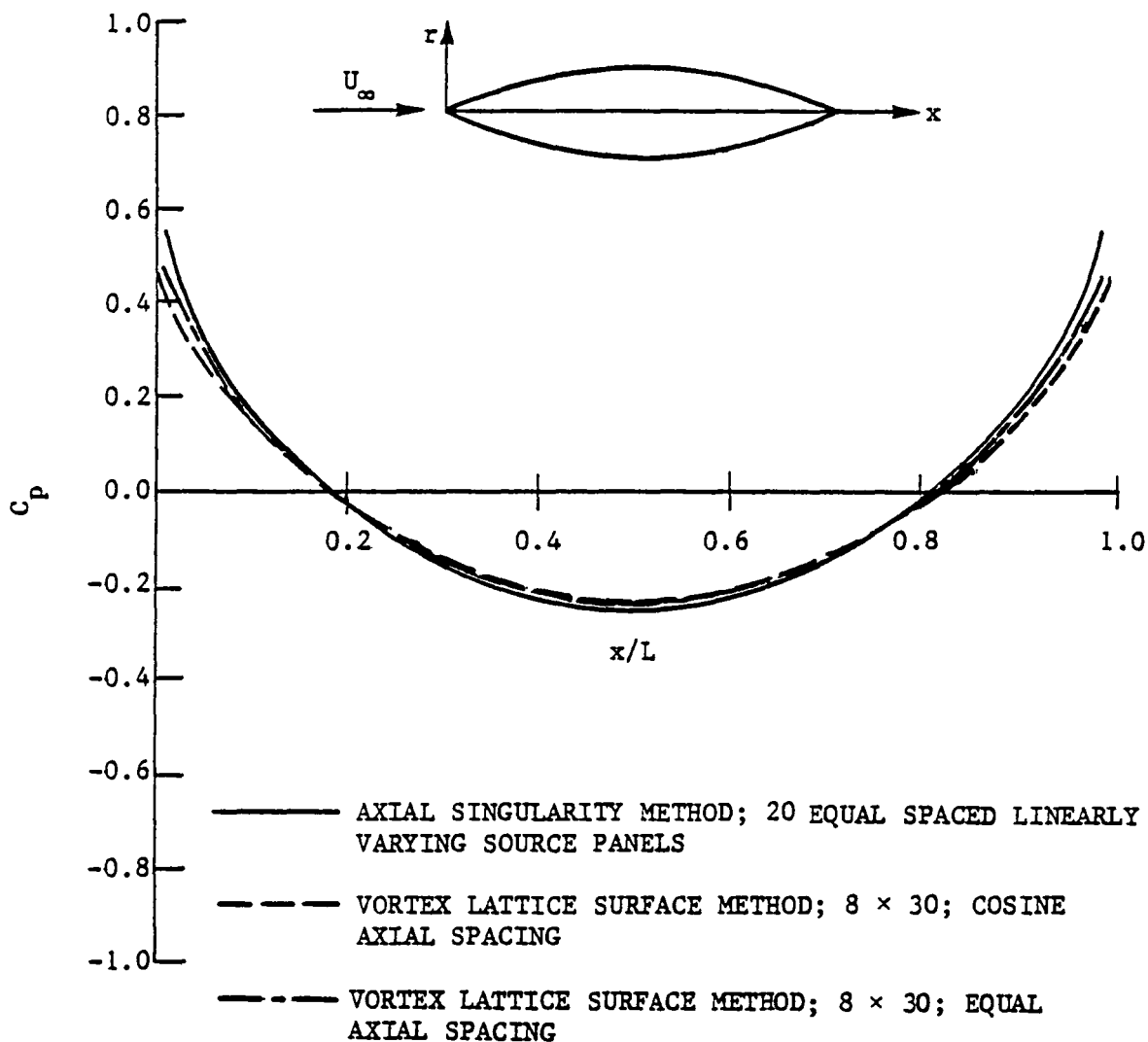
Figure 19. Pressure coefficient distribution for axisymmetric flow past a SR = 4, Ogival body of revolution, using axial singularity method and vortex lattice surface panel method.

(a) Strength distribution using constant source panels.

(b) Strength distribution using linearly varying source panels.

——————— AXIAL SINGULARITY METHOD; LINEARLY VARYING SOURCE; 10-1-10 PANEL DISTRIBUTION; a/L = 0.002

— — — AXIAL SINGULARITY METHOD; CONSTANT SOURCE; 10-1-10 PANEL DISTRIBUTION; a/L = 0.002

— —— VORTEX LATTICE SURFACE PANEL METHOD; 8 × 30 PANELS; EQUAL SPACING AXIALLY

MODIFIED ELLIPSOID CONTOUR

0.0667
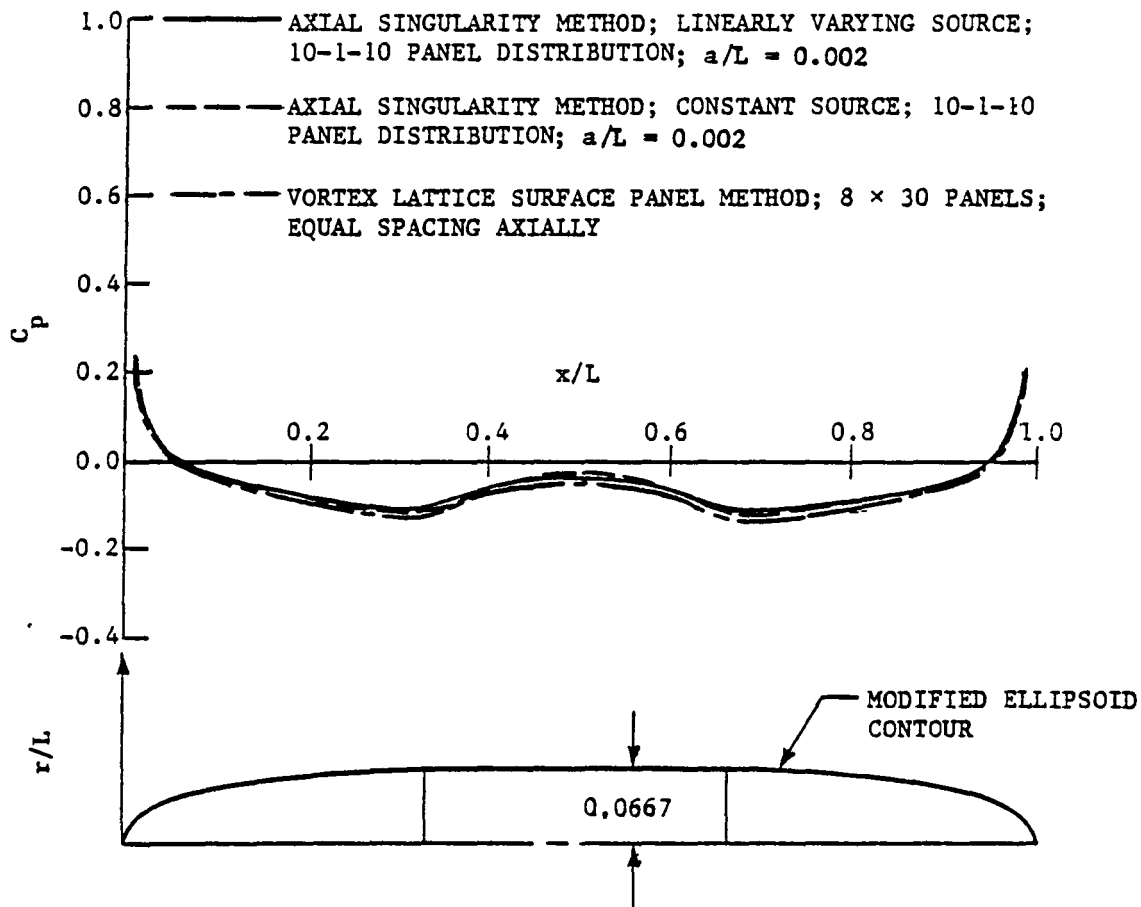
(c) Pressure coefficient distribution along meridian line.

Figure 20.   Pressure coefficient distribution along meridian line for axisymmetric flow past a cylindrical body with modified ellipsoidal nose and tail, using axial singularity method, and vortex lattice surface panel method.

120
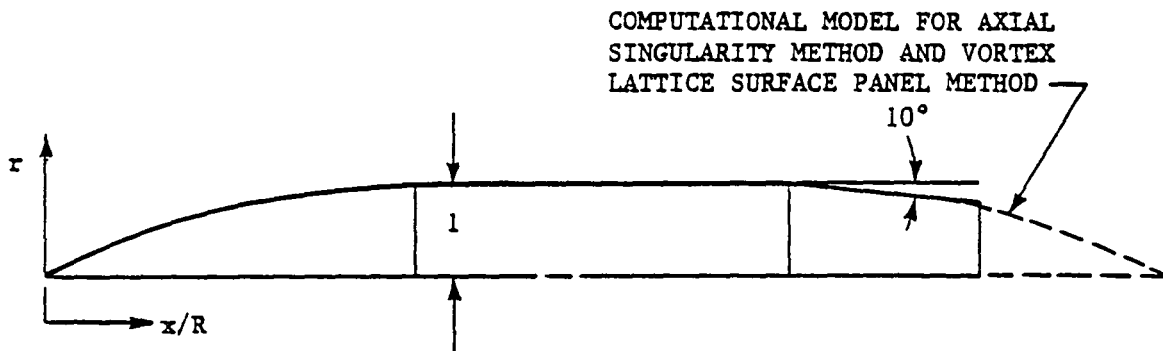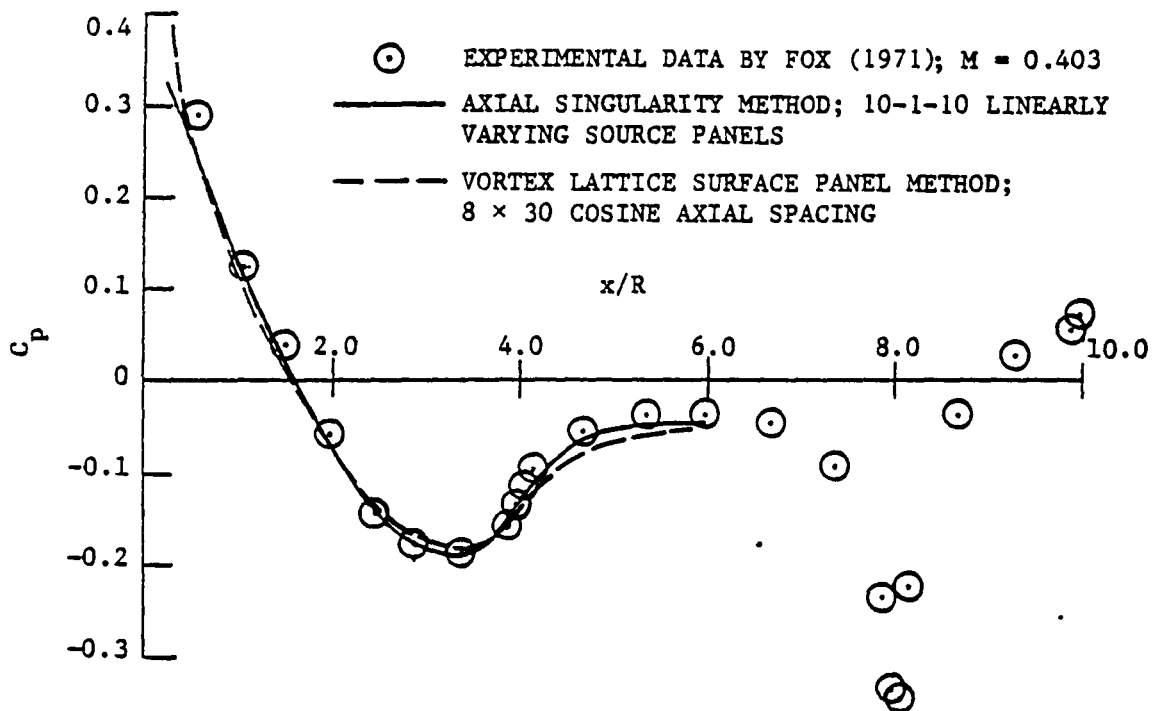
Figure 21. Pressure coefficient distribution along meridian line for axisymmetric flow past a cylindrical body with Ogival nose, using axial singularity method, and vortex lattice surface panel method.
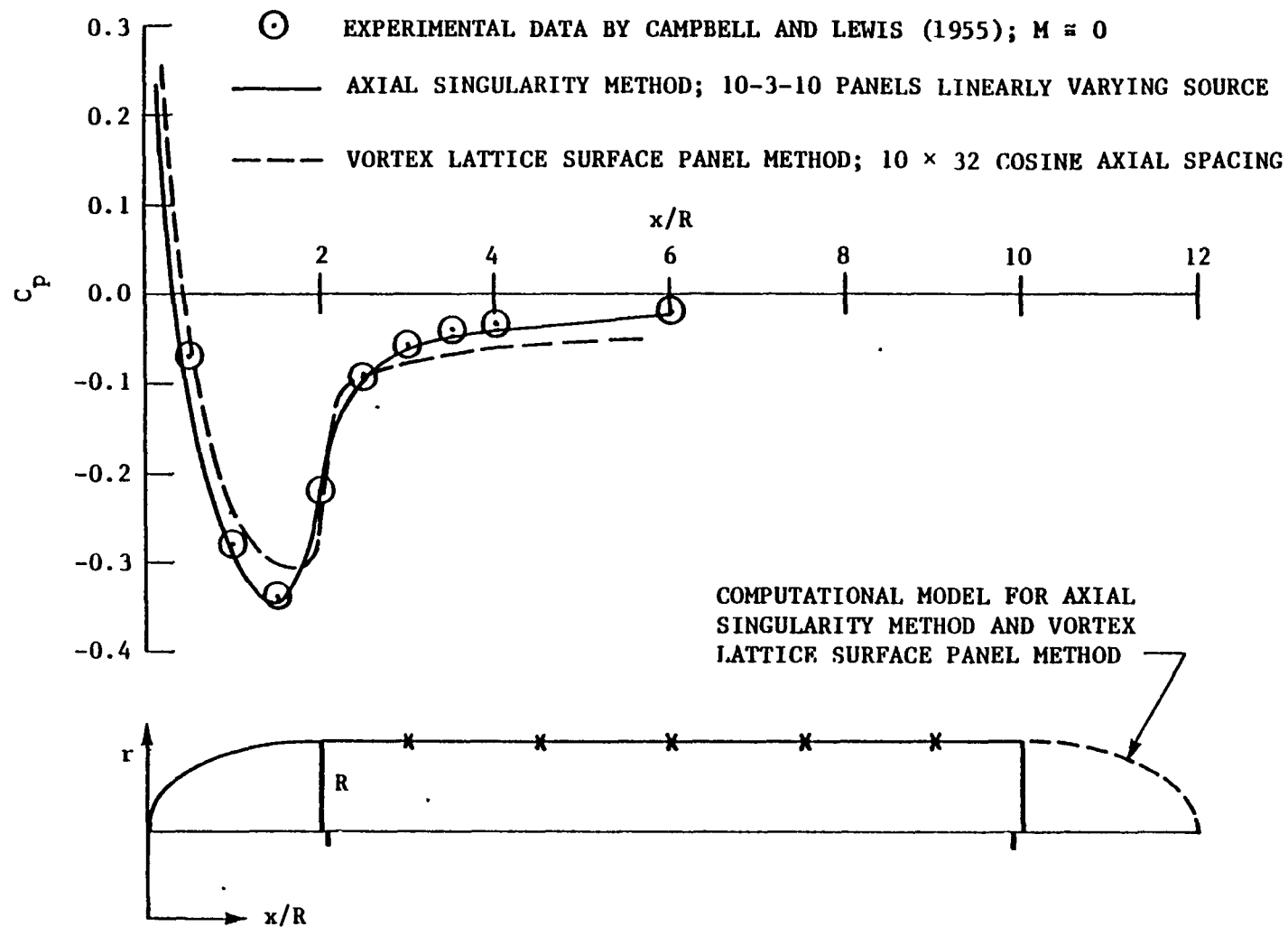
Figure 22. Pressure coefficient distribution along meridian line for axisymmetric flow past a cylindrical body with SR = 2 ellipsoidal nose, using axial singularity method, and vortex lattice surface panel method.
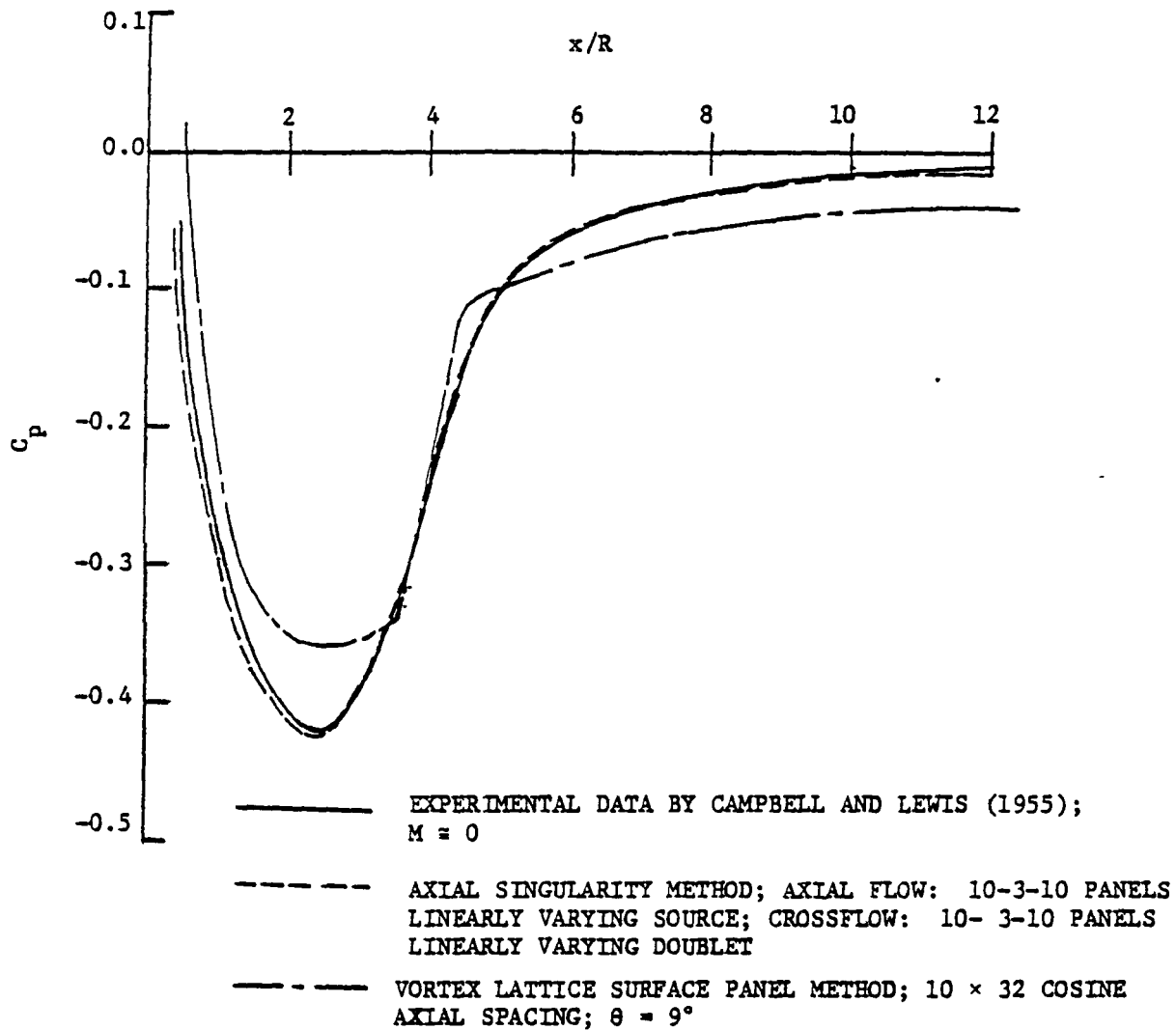
Figure 23. Pressure coefficient distribution along top meridian line for inclined flow α = 6.08° past a cylindrical body with SR = 2 ellipsoidal nose, using axial singularity method, and vortex lattice surface panel method.
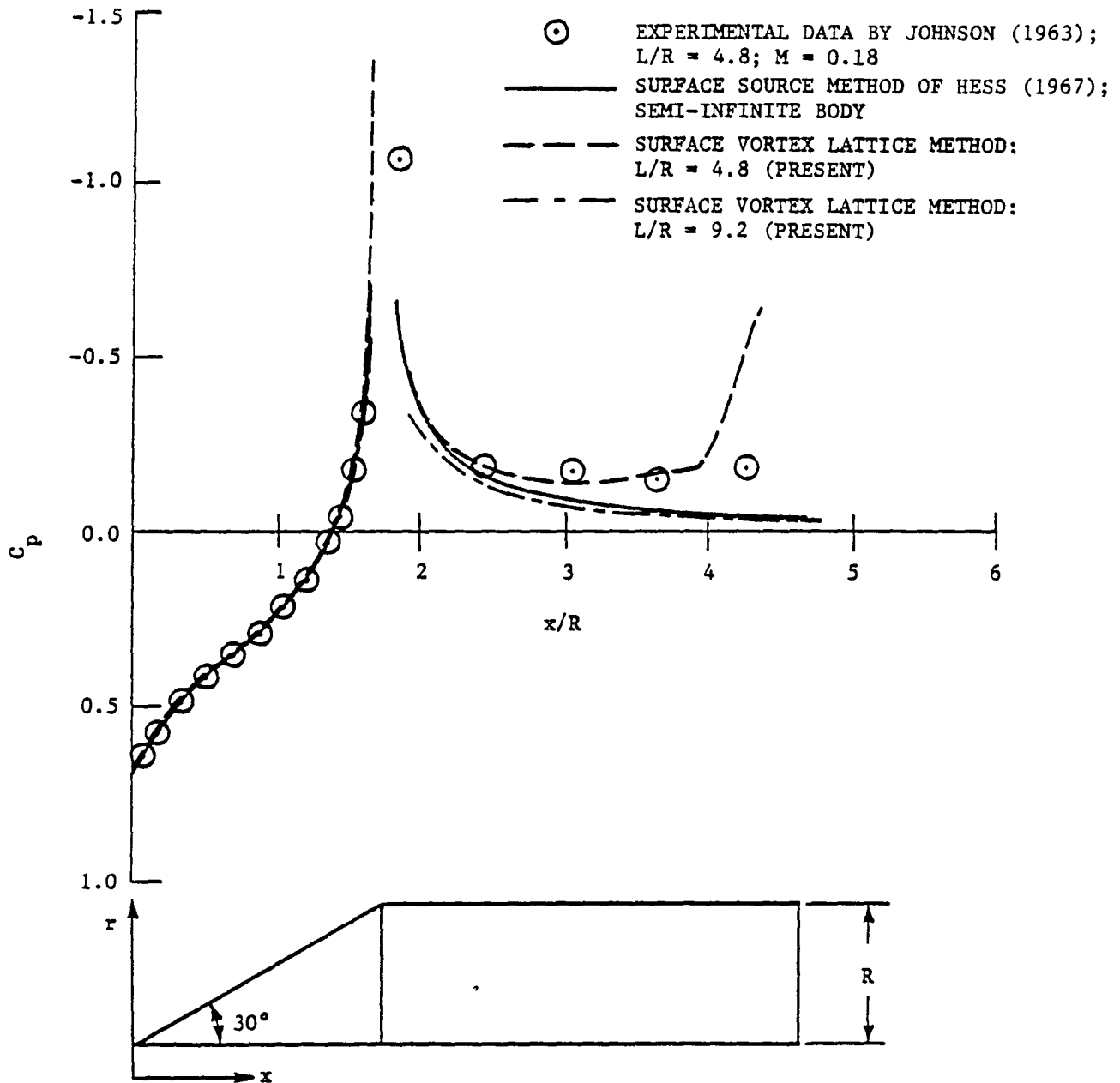
Figure 24. Pressure coefficient distribution along meridian line
for axisymmetric flow past a 30° cone-cylinder for
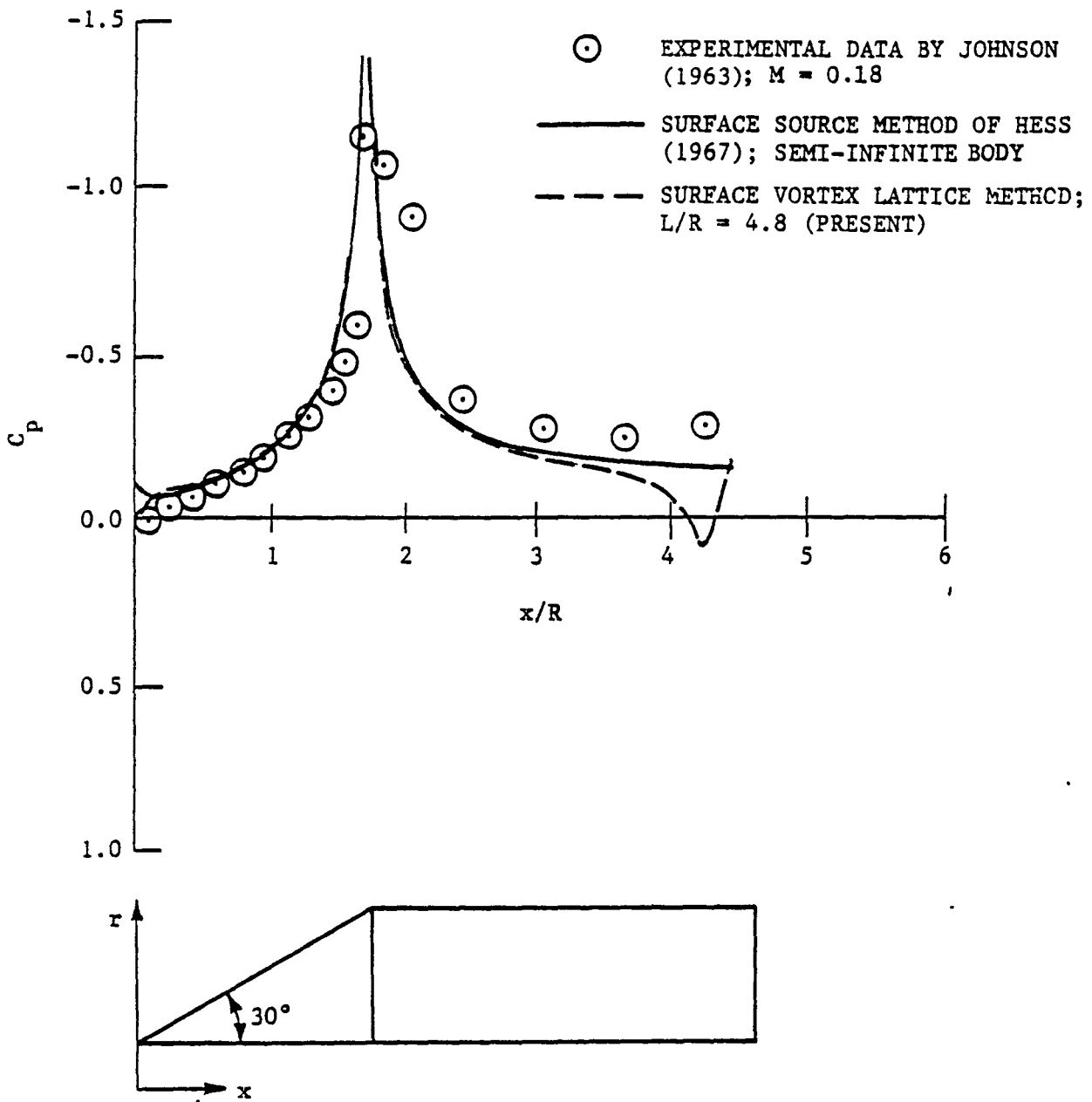vortex lattice surface panel method.

Figure 25. Pressure coefficient distribution along θ = 45° meridian line for flow at α = 20° past a 30° cone-cylinder for vortex lattice surface panel method.
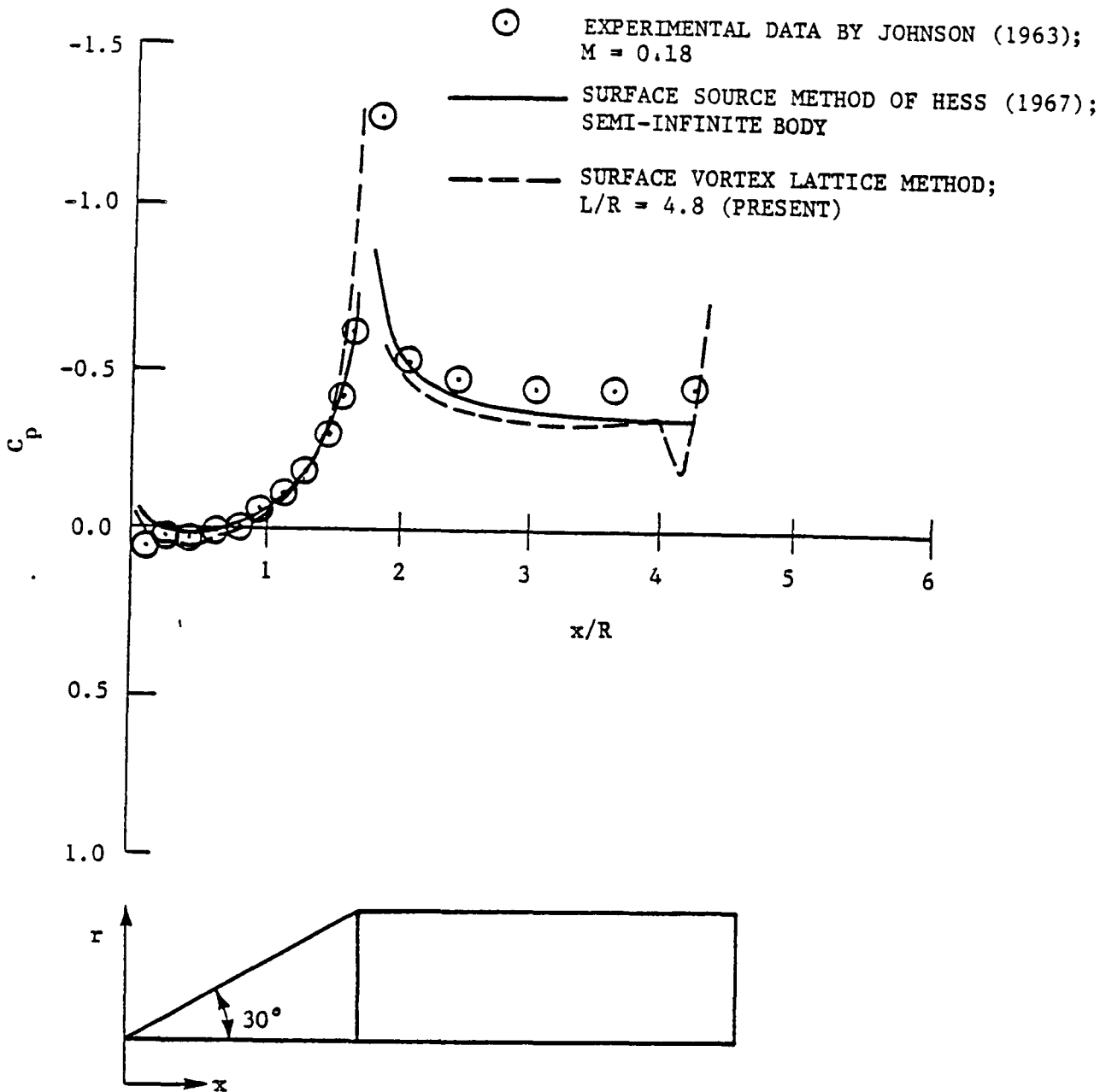
125

Figure 26. Pressure coefficient distribution along θ = 90°
meridian line for flow at α = 20° past a 30°
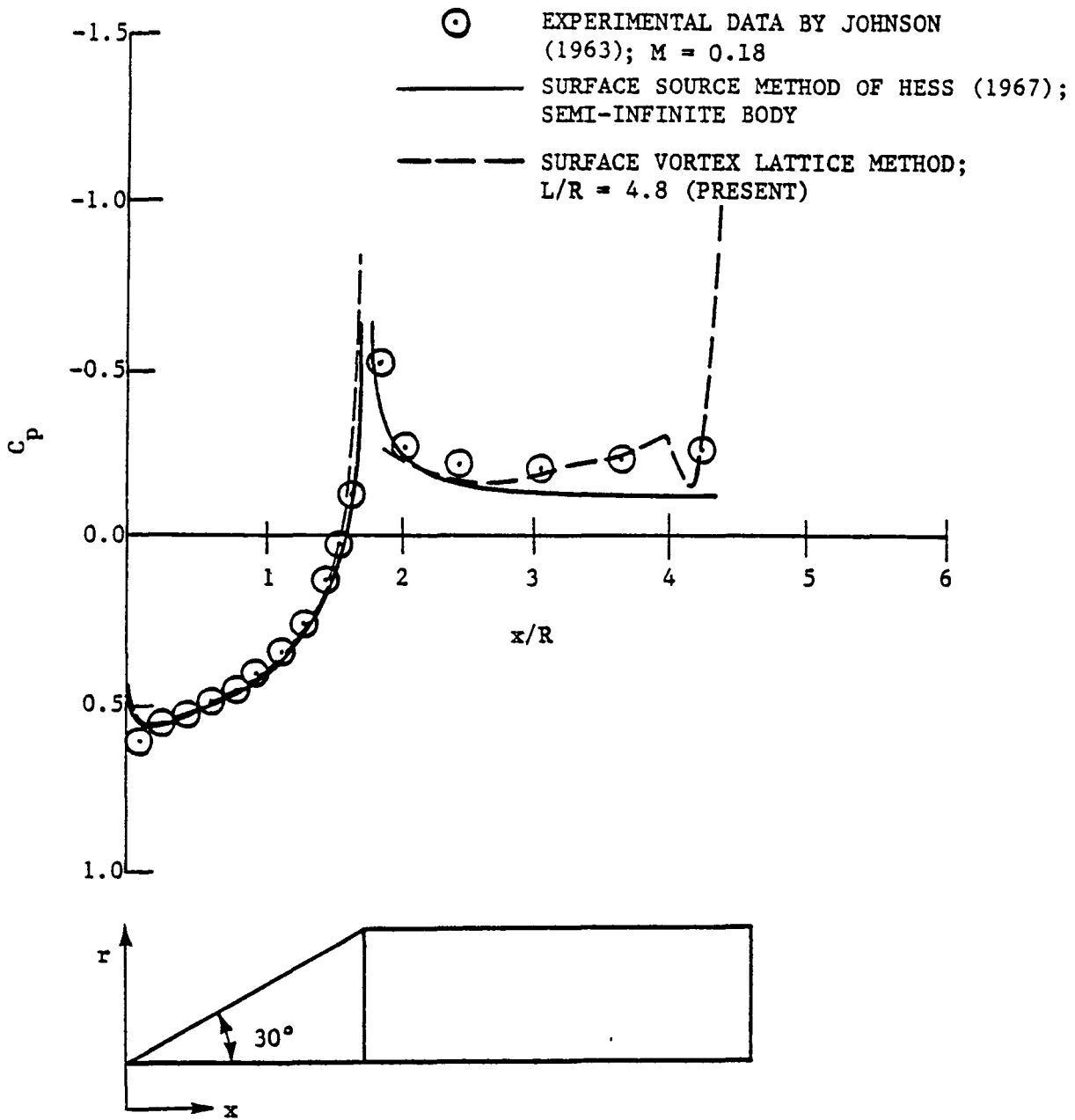cone-cylinder for vortex lattice surface panel
method.

126

Figure 27. Pressure coefficient distribution along θ = 135°
meridian line for flow at α = 20° past a 30°
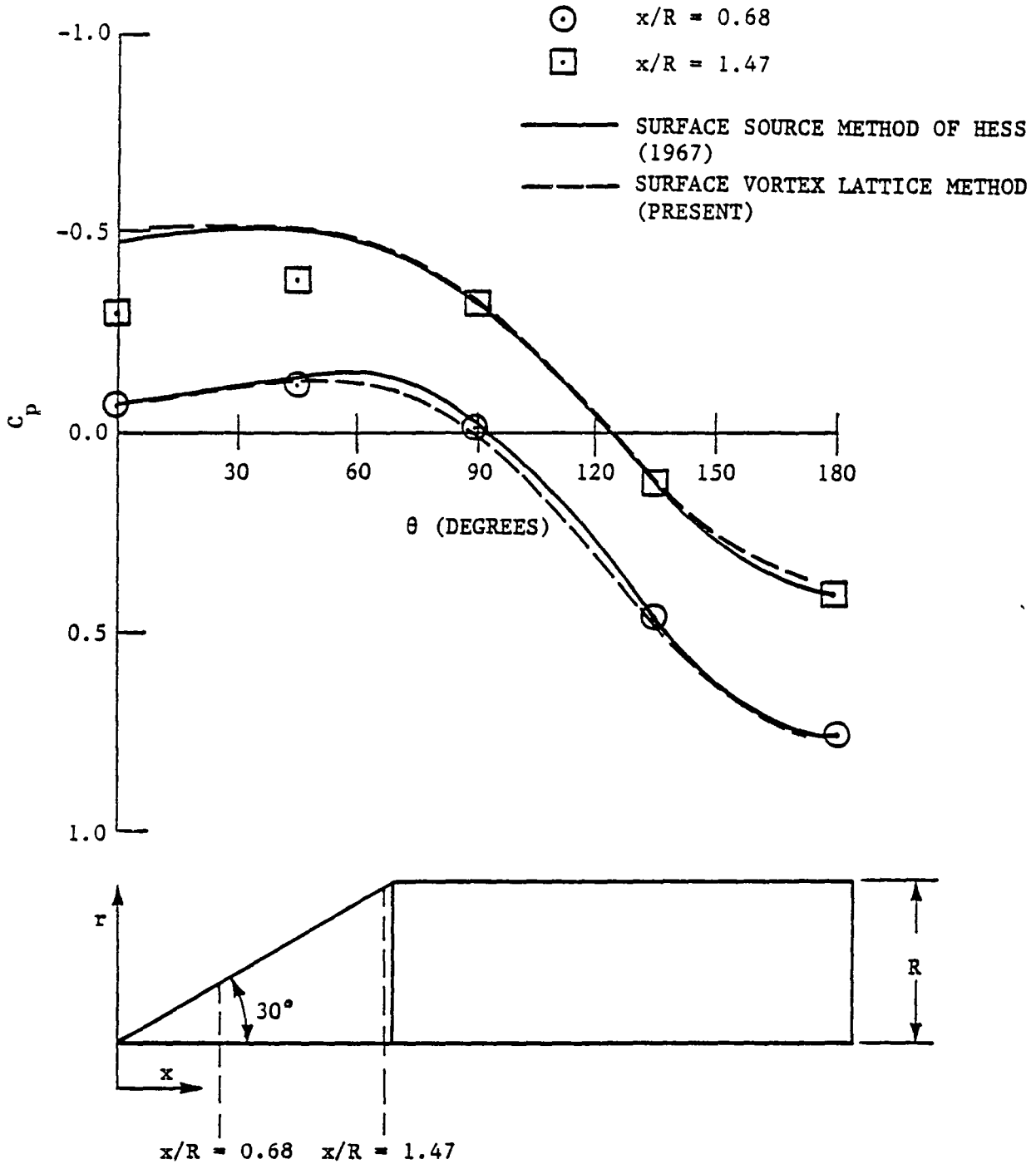cone-cylinder for vortex lattice surface panel
method.

Figure 28. Pressure coefficient distribution along circumferential
lines on cone for flow at $\alpha = 20°$ past a 30° cone-
cylinder for vortex lattice surface panel method.

1 Report No.	2. Government Accession No.	3. Recipient's Catalog No
NASA CR-166058		

4 Title and Subtitle	5 Report Date
Calculation of Potential Flow Past Non-Lifting Bodies At Angle of Attack Using Axial and Surface Singularity Methods	February 1983
	6. Performing Organization Code

7 Author(s)	8. Performing Organization Report No
Jin-Yea Shu and John M. Kuhlman	
	10 Work Unit No.

9 Performing Organization Name and Address	11 Contract or Grant No
Old Dominion University Research Foundation P.O. Box 6369 Norfolk, Virginia 23508-0369	NSG-1357
	13 Type of Report and Period Covered

12 Sponsoring Agency Name and Address	Contractor Report 1/1/81 - 8/31/82
National Aeronautics and Space Administration Washington, DC 20546	14 Sponsoring Agency Code

15 Supplementary Notes
Langley Technical Monitor, Neal T. Frink Topical Report

16. Abstract

Two different singularity methods have been utilized to calculate the potential flow past a three dimensional non-lifting body. Two separate FORTRAN computer programs have been developed to implement these theoretical models, which will in the future allow inclusion of the fuselage effect in a pair of existing subcritical wing design computer programs.

The first method uses higher order axial singularity distributions to model axisymmetric bodies of revolution in an either axial or inclined uniform potential flow. Use of inset of the singularity line away from the body for blunt noses, and cosine-type element distributions have been applied to obtain the optimal results. Excellent agreement, to five significant figures, with the exact solution pressure coefficient value has been found for a series of ellipsoids at different angles of attack. Solutions obtained for other axisymmetric bodies compare well with available experimental data.

The second method utilizes distributions of singularities on the body surface, in the form of a discrete vortex lattice. This program is capable of modeling arbitrary three dimensional non-lifting bodies. Much effort has been devoted to finding the optimal method of calculating the tangential velocity on the body surface, extending techniques previously developed by other workers. Again, the best solution for ellipsoids at angles of attack ranging between 0-30°, has been obtained using cosine spacing of the elements axially.

17 Key Words (Suggested by Author(s))	18 Distribution Statement
Potential Flow Bodies of Revolution at Angle of Attack	Unclassified - Unlimited Subject Category 02

19 Security Classif. (of this report)	20 Security Classif (of this page)	21. No. of Pages	22. Price*
Unclassified	Unclassified	130	A07

End of Document